Mathematical Modeling of Shock Induced Martensitic Phase Transitions

by

John Lloyd Weatherwax
BS Mathematics with honors
BS Physics with honors
University of Missouri-Columbia
1996

Submitted to the Department of Mathematics
in partial fulfillment of the requirements for the degree of
Doctor of Philosophy
at the
MASSACHUSETTS INSTITUTE OF TECHNOLOGY
September 2001

Author .....
Department of Mathematics
August 10, 2001

Certified by .....
Rodolfo Ruben Rosales
Professor of Applied Mathematics
Thesis Supervisor

Accepted by .....
Daniel J. Kleitman
Chairman, Applied Mathematics Committee

Accepted by .....
Tomasz S. Mrowka
Chairman, Department Committee on Graduate Students

Mathematical Modeling of Shock Induced Martensitic Phase Transitions

by

John Lloyd Weatherwax

Submitted to the Department of Mathematics
on August 10, 2001, in partial fulfillment of the
requirements for the degree of
Doctor of Philosophy

Abstract

Recently Bruno and Vaynblat introduced a new mathematical model to describe shock induced martensitic phase transitions. This model is much simpler than prior ones — requiring, essentially, no quantities that cannot be measured directly. Nevertheless, its predictions are in very good agreement with the experimental results.

In the calculations that Bruno and Vaynblat did to match their model against experiments, they simplified the dynamics — replacing rarefaction waves by "rarefaction discontinuities". In this thesis we implement the Bruno-Vaynblat model without any such simplifications. In the process of doing this, a new numerical method for nonlinear hyperbolic conservation laws with phase transitions is developed. Furthermore, in order to improve the quantitative agreement with experiments, several extensions of the Bruno-Vaynblat model are introduced and studied. These include the addition of dissipative effects, and the introduction of a modification to the equation of state (for the Austenite phase) near the critical transition pressure.

Thesis Supervisor: Rodolfo Ruben Rosales
Title: Professor of Applied Mathematics

Acknowledgments

I would first like to thank Dr. Rosales. He is one of the reasons that I was accepted to MIT and has been unbelievably helpful and supportive through out my entire time here. He always had faith and good spirits for me and came through when I needed him most. He is truly a great person with a great heart. I am very glad that I have had the opportunity to work with and get to know him.

I would secondly like to thank Dimitri Vaynblat. His help and guidance was invaluable and I don't think that I could ever thank him enough. I hope that we stay very close friends and I know that he deserves all the wonderful things that will come his way.

I would like to thank the close friends that I have had for many years. Brent Elliott has been supportive and a constant source of good conversation. I wish that we lived closer so that we could have more time together. Troy Hall has been a constant source of ideas and thoughts; some mathematical some not. His humor gives a spark to life and I will enjoy watching him achieve many great things.

I would also like to thank the friends I have made here at MIT: David Amundsen, Mats Nigam, Lior Pachter, Boris Schlittgen, Peter Clifford, Adrian Vetta, Bill Bradley, Adam Klivans and Francis Poulin have made my time here at MIT very enjoyable on a personal level. I am lucky to know each of them and hope that we remain close.

Thanks should also go to the great professors that I feel privileged to have taken classes with or have known: Dr. Michael Brenner, Dr. Oscar Bruno, Dr. John Bush, Dr. Harvey Greenspan, and Dr. Tony Patera. An especially special thanks goes to Dr. Oscar Bruno who was kind enough to allow me to work at CalTech during July (2000) through March (2001) during which the majority of this work was done. My time at CalTech was very exciting and stimulating. In both large and small ways, without Oscar Bruno's help, much of this work probably wouldn't exist.

My wife Christine deserves perhaps the greatest amount of thanks. She has been a constant example of the best that people can be and I feel truly blessed to have her

in my life. She was the strength that keep me going when times were really tough and without her I could not be what I am today. I hope that I can give her many years of happiness.

Finally I would like to thank my family. My mother has given me the idea that dreams are to be sought after and a desire to want more from life than most people seek. She could be considered as one of my sources of emotional strength. To my sister who is very talented and smart, I wish the world. She deserves all that she can and will achieve. To my brother who I see as a smarter version of myself and who maybe one of my best friends. Finally I would like to thank my father. He has perhaps had the toughest time of all the people listed here. I thank him for the raw intellectually ability, the stubbornness to never give up, and the strong desire to learn. I hope that this accomplishment lifts his spirits some.

Contents

List of Figures

List of Tables

Chapter 1

Introduction and Background

1.1 Introduction

Phase transitions are common in nature, such as the solid–to–liquid (melting) or liquid–to–gas (evaporation) changes most substances undergo as temperature and/or pressure are changed. Solid–to–solid phase transitions, while less common, also occur in nature. For example, the atomic structure of solid graphite can change to that of diamond under sufficiently large static pressures. These pressures are so large that they are difficult to achieve in static conditions, but they can easily be produced with shock waves. The jump in pressure carried by a strong shock wave can be large enough to promote the required atomic rearrangements. Small quantities of diamond can indeed be produced in this way [21, 26].

Shock–induced solid–to–solid phase transitions occur in systems other than the graphite–diamond one mentioned above. The α–iron to ϵ–iron phase transition discovered experimentally by Bancroft et al. in 1956 is another example. Bancroft et al. detected this phase transition by measuring the velocity of the free surface of an iron sample through which a strong shock wave passed [2]. A detailed description of Bancroft et al.'s experiment is given in section 1.2. Eighteen years later, Barker and Hollenbach [5] repeated the measurements by Bancroft et al. with a much higher degree of accuracy. The free surface velocity plots they produced are still widely used by theoreticians to test models for the α–ϵ iron phase transition. One such model is

the one proposed by Bruno and Vaynblat (BV), on which the work in this thesis is based [13, 14].

The model Bruno and Vaynblat introduced to describe shock induced martensitic phase transitions is much simpler than prior ones. Earlier models required functions and constants whose determination is not entirely clear (at least to this author), while the BV model has no quantities that cannot be measured independently of the phase transition experiments. Nevertheless, its predictions are in very good agreement with the experimental results.

In the calculations that Bruno and Vaynblat did to match their model against experiments, they simplified the dynamics — replacing the rarefaction waves by "rarefaction discontinuities". This makes the calculation of the solution to the equations much simpler, since then they can be solved essentially exactly. To be more precise, with this assumption the problem is reduced to that of solving a small number of Riemann problems since the wave interactions are simplified to the extent that the state variables are piecewise constant at any time in the evolution.

In this thesis we first implement the BV model without the "rarefaction discontinuity" simplification. This requires the solution of a nonlinear hyperbolic system of conservation laws with discontinuous coefficients. The discontinuous coefficients arise because of the phase transformation. In the process of doing this, a new numerical method for nonlinear hyperbolic conservation laws with phase transitions is developed. The results of this calculation are then compared with the experiments of Barker and Hollenbach, and the discrepancies and their possible causes are discussed.

Next, in order to improve the quantitative agreement of the model with the experiments, several extensions of the Bruno-Vaynblat model are introduced and studied. These include the addition of dissipative effects and the introduction of a modification to the equation of state for the austenite phase near the critical transition pressure. In both cases numerical algorithms for the augmented model are implemented, and the results of the calculations are compared with the experiments.

As a conclusion to this section, we mention that there are several motivational factors for the work presented in this thesis. The first is that of a purely scientific

interest. The shock experiments described in the next section represent an example of a phase transformation happening very far from equilibrium. At this time not many qualitative predictions can be made in these situations. It would be of great scientific interest to be able to extend current understanding of these experiments through accurate mathematical modeling techniques. Secondly the introduction of a viscosity in chapter 4 to the base BV-theory provides a way of measuring the viscosity of iron under extreme pressure conditions. This value would be of interest to the geophysical community where the similarity in the pressures encountered here and those at the center of the earth make it an estimate of the viscosity of the earth's liquid core. The determination of the viscosity of the earth's core would provide an important parameter in theories relating to the earth's geodynamo [38]. We note here that the viscosity of the iron in the earth's outer core is currently not very well known. Predicted values spread 14 orders of magnitude [64]. The two values for the viscosity of iron predicted in this thesis are $9.11 \times 10^2\, P$ and $1.27 \times 10^4\, P$. We note that these two values fall in the middle of the range currently predicted by the geophysical literature [64].

Additional support for the values of the viscosity found in chapter 4 are provided by workers in the field of steady shock propagation in solids. There an attempt to predict values of an effective viscosity for aluminum [58, 63] to explain wave profiles seen in experiments similar to the ones considered in this thesis [67], predict effective viscosities in the range of $1.4 \times 10^3\, P - 2.0 \times 10^4\, P$. The viscosities predicted in this study agree quite well with these earlier calculations.

1.2 Experimental Background

Many materials undergo solid–to–solid phase transitions under sufficiently large static pressures [41, 62]. In parallel with static research on solid–to–solid phase transformations, many groups were investigating the possibility of using dynamic forces to produce the high pressures required. In the 1950s, a discrepancy arising from data taken from static experiments [11, 10] versus data taken from impact experiments [73]

prompted an investigation into the possibility of a solid–to–solid phase transformation in iron [2]. Due to the extremely high pressures needed to produce this phase transformation, early static experiments failed to detect it[1]. In 1956 Bancroft et al. [2] was able to show that iron has a solid–to–solid phase transformation, at around $13\,GPa$. Compared to irons tensile yield stress of 0.1 GPa [43] this is an enormous pressure.

In order to reach the pressures needed for the transformation, Bancroft et al. used dynamic forces rather than the static ones used by their predecessors. The experiments by Bancroft et al. involve sandwiching a flat, cylindrical, iron sample between baratol (a high power explosive made of T.N.T. and barium nitrate) on one side, and a set of recording pins positioned against the opposing surface (see the left picture in figure 1-1). The baratol is used to generate a strong shock wave that travels into the sample, while the pins are used to record the motion (velocity) of the "free surface", on the other side of the sample. When the baratol is ignited, a strong shock wave is generated that travels into the sample. On the other side of the sample, all the disturbances that arrive there, after traveling through the sample, are recorded by the pins.

Bancroft et al. reported that, when the experiment is conducted, the pins record a series of three discontinuous jumps in the velocity of the free surface. Bancroft et al. postulated that three, one-dimensional,[2] shock-like waves are produced by the explosion, propagate through the iron, and eventually impact upon the free surface producing the observed discontinuous velocity jumps of the free surface. The picture on the right in figure 1-1 shows a sketch of a space–time diagram illustrating this situation: Three sharp "discontinuous" waves are born at the origin — the position of the surface of the sample is in contact with the baratol at the time of the explosion. These waves travel through the sample at different speeds and eventually reach the free surface. As each wave reaches the free surface, a jump in the free surface velocity is produced.

[1] Recently the use of synchrotron radiation and a diamond–anvil apparatus has been used for very accurate static investigations of the solid–to–solid phase transformation in iron [7, 36, 51].

[2] That is, the waves are plane, with phase surfaces parallel to the sample cylinder faces, and propagate along the direction given by the axis of the cylinder.

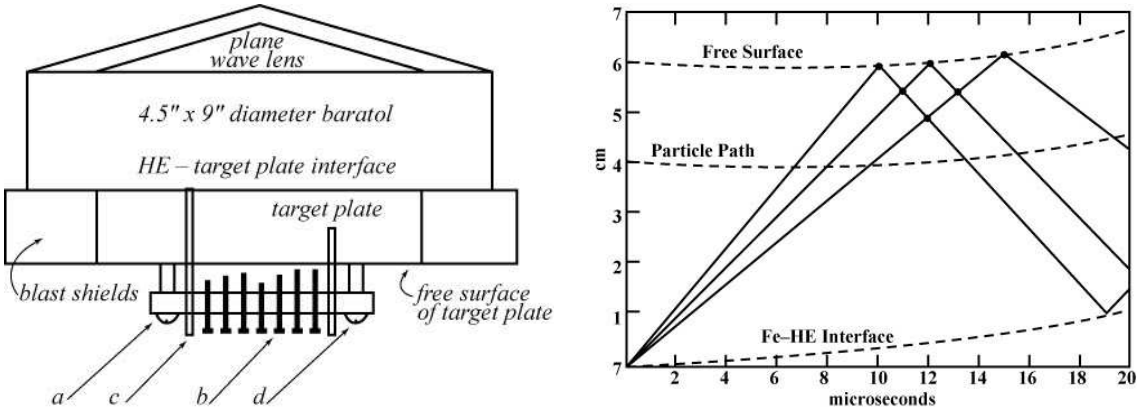

Figure 1-1: **Left:** Experimental apparatus used in the 1956 experiments by Bancroft et al. **Right:** Sketch of a space–time wave diagram for the experiment. The horizontal axis is time, measured in microseconds from the moment of the baratol explosion. The vertical axis is space, measured in centimeters along the axis of the cylinder sample, from the interface in contact with the baratol. The top dashed line plots the free surface position and the bottom dashed line plots the position of the interface originally in contact with the baratol. The middle dashed line is a plot of the particle path for a typical particle in the iron sample. At time $t = 0$ three shock–like waves (solid lines) originate at the origin and travel into the sample. As each wave arrives to the free surface, it imparts a jump to the particle velocity there, producing a jump in the free surface velocity which is recorded by the pins shown on the left picture. These pictures are replicas of similar ones presented in [2].

Bancroft et al. interpreted the results of their experiments as follows:

- Had the experiments produced only two jumps in the free surface velocity, the first jump would be interpreted as being due to the iron's elastic response, and the second to its plastic response[3]. That is to say, the pressure wave generated by the explosion would split into two shock waves: the first weaker and faster wave travels via the elastic response of the material, while the second slower and much stronger wave travels via the plastic response of the material. These waves, upon arrival at the free surface, would produce two jumps in the free surface velocity.
- The presence of a third jump/wave can be explained by the hypothesis that a polymorphic solid-to-solid phase transformation happens in the sample, where

[3]Here we define elastic and plastic in a material science manner. An elastic deformation is a deformation from which the iron can recover its original form. A plastic deformation is one in which the iron cannot.

the atoms of iron rearrange themselves after a strong impact, changing from one crystalline structure to another. This transformation is similar to the one that had previously been observed in steel.

The waves produced are then: First, a shock wave in elastic iron. Second, a shock wave in plastic iron. Third, a phase transformation wave.

This interpretation is the currently accepted one. The initial phase of iron is now called α-iron and is normal phase of iron found at room temperature. It possesses a body centered cubic structure and is ferromagnetic. The transformed phase is called ϵ-iron and is a more compact form of iron found only at much greater pressures. It possesses a hexagonal closed packed crystalline structure and is paramagnetic. When speaking of solid–to–solid phase transformations of this type in a more general context, the first phase of the material is often referred to as the *austenitic* phase or austenite, and the second phase as the *martensitic* phase or martensite.

Advances in laser interferometry technology allowed experiments of the same type as those carried by Bancroft et al., but with much more accurate measurements of the free surface velocity than those possible with the pin technique used by Bancroft et al. Experiments using an interferometer were performed by Barker and Hollenbach in 1974, at the Sandia National Laboratory [5]. Since all the theoretical work that follows will be compared to the Barker and Hollenbach experiments, we now describe these experiments in some detail.

Barker and Hollenbach's iron samples were taken from very pure flat iron stock. In their experiment the impact delivered to the samples is produced by firing an *impactor* at the iron *target*, using a high-velocity powder gun (see figure 1-2 for a sketch of the experimental set up). Opposite the face where the impact is delivered, a laser interferometer is used on a portion of the specimen surface. Any motion of this free surface imparts a Doppler shift in the wavelength of the laser light, and the number of interference fringes is recorded. The number of fringes is proportional to the velocity of the free surface, which is recorded versus time as the experiment proceeds. In the plots produced (see the left picture in figure 1-3), the unit of time

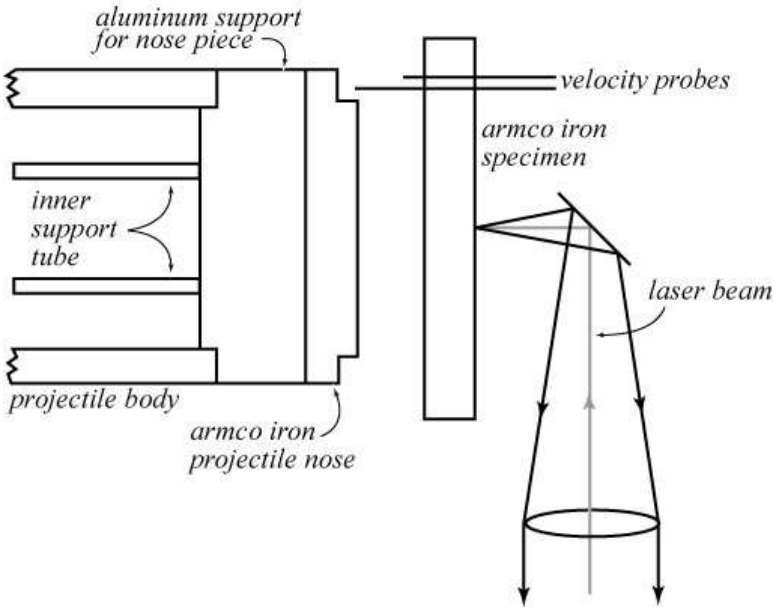

Figure 1-2: Setup for the Barker and Hollenbach experiments. The interferometer is not displayed. This picture is a replica of the one presented in [5].

is scaled by the total thickness of the sample that produced it, so that the horizontal axis in the plots is an inverse velocity. Thus each wave signature appears at a position equal to the inverse of its average velocity across the sample.

A representative sample of some of the Barker and Hollenbach experimental plots obtained by varying the impactor strength and sample length is shown on the left in figure 1-3. Only a few curves are presented out of the sixteen or so experiments that were performed. These few experiments have been selected to show the full range of observed effects. Each curve is given the number assigned by Barker and Hollenbach to label their experiments. Each jump in a curve corresponds to the arrival of a wave at the free surface, which responds by a change in its velocity (see the right frame in figure 1-1). Sharp jumps indicate the arrival of a "discontinuous" wave (e.g.: a shock wave) and wide jumps the arrival of a "smooth" wave. We notice the following facts:

- All the plots show a relatively small wave at time/thickness $\approx 0.17\, sec/km$, involving a change in free surface velocity from $0.00\, km/sec$ to approximately $0.05\, km/sec$.
- For weak impacts (e.g.: experiment number 14) or very strong impacts (e.g.: experiment number 9) only one additional wave is produced: A large jump at

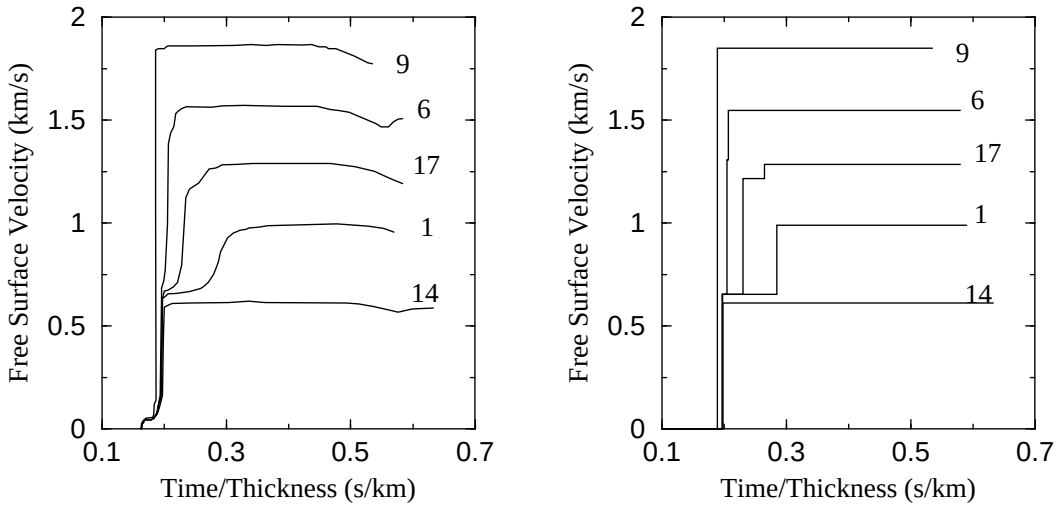

Figure 1-3: Free surface velocity profiles for the α-ϵ phase transition in shock loaded iron.
Left: Experimental measurements by Barker and Hollenbach [5].
Right: Bruno–Vaynblat theoretical model, using the "rarefaction discontinuity" approximation.
Each curve represents a record of the free surface velocity for one experiment, with the numbers as assigned by Barker and Hollenbach to label their experiments. Only a few representative samples of their measurements are displayed in these plots. In all the experiments shown here the sample thickness and diameter are approximately $6\,mm$ and $10\,cm$, respectively. In terms of the impactor velocity, the curves order naturally from bottom (lowest velocity) to top (highest velocity), i.e.: as a function of increasing impactor velocity, the experiments are ordered in the sequence 14, 1, 17, 6, and 9.
The vertical axis is the free surface velocity and the horizontal axis is time scaled by the total thickness of the sample in each experiment, so that the horizontal axis in the plots is an inverse velocity. Thus each wave signature appears at a position equal to the inverse of its average velocity across the sample.

time/thickness $\approx 0.2\,sec/km$.

- For intermediate impactor strengths (e.g.: experiments number 1, 17, and 6) two additional waves are produced: A large jump at time/thickness $\approx 0.2\,sec/km$ to a velocity of around $0.7\,km/sec$ followed by another jump sometime after time/thickness $= 0.2\,sec/km$ to the final asymptotic velocity value for each curve.

The three-wave structure found by Bancroft et al. [2] is present in the experiments numbered 1, 17, and 6. We note that these experiments correspond to intermediate impactor strengths.

The first wave, at time/thickness $\approx 0.17\, sec/km$, causes a small jump in velocity and is present in all the experimental curves. As explained before, this wave is known to be a pressure-increasing shock wave traveling in elastic iron [2, 5][4]. Because of its relatively small size in relation to the other jumps and the fact that its origin is well understood, it will be neglected during the work presented in this thesis. The other much larger jumps in velocity are known to be due to the plastic response of the iron and the presence of a phase transition. They will be the main focus of all the subsequent mathematical modeling in this thesis.

We note that when the elastic precursor wave is neglected, the remaining free surface velocity profiles can be described as possessing either a one wave or a two wave structure. When referring to free surface velocity profiles with two waves, the waves will be referred to as the first wave and the second wave. They will be ordered by their time of arrival at the interface.

The type of phase transition discussed in this thesis also occurs in materials other than iron. For instance, Erskine et al. [26] performed shock experiments similar to those of Baker and Hollenbach with solid graphite, producing diamond as the martensitic phase. Their experiments also produced free surface velocity plots with a two wave structure for a certain range of impactor strengths (see figure 1-4). In these experiments no switch from elastic to plastic response was observed, and no precursor elastic "toe" can be seen in the measured curves.

In this thesis we will develop and study mathematical models for austenite–martensite phase transitions, such as the ones in iron and in graphite–diamond. The success of the models will be measured by how well they reproduce the free surface velocity plots of Barker and Hollenbach, as given on the left in figure 1-3.

[4] Similar to many materials iron behaves elastically for low enough pressures; at higher pressures it behaves plastically.

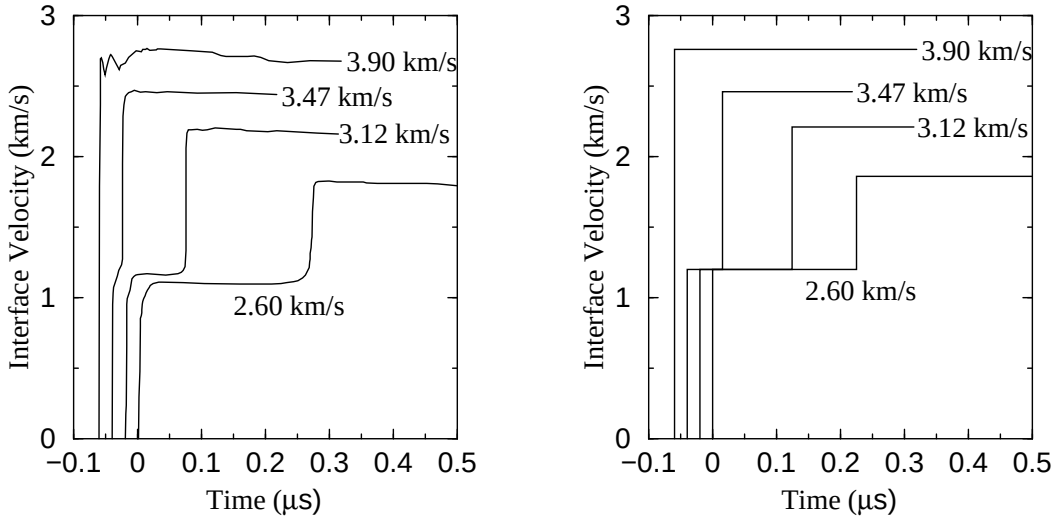

Figure 1-4: Free surface profiles for impact stressed graphite. The vertical axis is the free interface velocity. The horizontal axis is time. **Left:** Experimental measurements by Erskine et al. [26]. **Right:** Bruno–Vaynblat theoretical model, using the "rarefaction discontinuity" approximation.

1.3 Prior Theoretical Work

Prior continuum level theoretical work in the modeling of shock–induced martensitic phase transformations relies heavily on the ideas of meta-stability and in the modeling of the kinetics of the transformation process [8, 72].

In 1997, Vlodarchik and Trebinski [72] modeled phase changes in graphite, taking great care to describe the various possible atomic configurations of the carbon as stresses are applied. An argument is made claiming that the hexagonal ring structure of the carbon atoms in graphite should deform by "puckering". Puckering is defined as an arrangement of carbon atoms where every other atom is displaced out of the original plane of the hexagonal ring. Using these atomic configuration of puckering, the compression of graphite is described by a series of steps in which the atoms, in response to external pressure, move from one configuration to another. These atomic rearrangements take place only after a mixture of graphite and diamond appears. How exactly this mixture forms is unclear. From this point, the mixture is governed by assumptions of local thermodynamical equilibrium. These authors describe the

kinetics of further phase transformation with the expression:

$$\frac{d\lambda}{dt} = [\lambda_m(p) - \lambda]\ A\ \exp\left[\frac{-\Delta\varepsilon(p)}{R\,T}\right], \tag{1.1}$$

where λ denotes the mass fraction (from $\lambda = 0$ for no martensite, to $\lambda = 1$ for all martensite), p is the pressure, $\lambda_m = \lambda_m(p)$ is a *target degree of transformation* for a given pressure,[5] $\Delta\varepsilon(p)$ is the height of the energy transformation barrier (assessed on the basis of a proposed isotherm of graphite at pressure p), R is the ideal gas constant, T is the temperature, and A is a constant.

Vlodarchik and Trebinski argue that the work involved in transforming the material, i.e.: $\Delta\varepsilon(p)$, is stored in the thermal vibrations of the atoms prior to the transformation. From this they obtain the following equation for $\Delta\varepsilon$

$$\int_0^T \chi(\theta)\, c_p(\theta)\, \mathrm{d}\theta = \Delta\varepsilon\,, \tag{1.2}$$

where $\chi(T)$ is the fraction of the thermal energy stored in the atom's vibrations in the direction perpendicular to the hexagonal planes of the graphite. An estimate for $\chi(T)$ can be obtained using the Krumhansl and Brooks model [42], which yields:

$$\chi(T) = \frac{1.5D(x_c) - x_c\,(e^{x_c} - 1)^{-1}}{1.5D(x_c) - x_c\,(e^{x_c} - 1)^{-1} + 3D(x_a) - 2x_a\,(e^{x_a} - 1)^{-1}}\,, \tag{1.3}$$

where

$$D(x) = \frac{2}{x^2}\int_0^x \frac{s^2}{e^s - 1}\,\mathrm{d}s\,, \tag{1.4}$$

with x_c and x_a defined by

$$x_c = T_{DC}/T\,, \qquad \text{and} \qquad x_a = T_{DA}/T\,. \tag{1.5}$$

Finally, T_{DC} and T_{DA} are the Debye temperatures for vibrations in the two main directions in the crystalline structure. With these assumptions, plus continuum equations

[5] For a detailed explanation of the choice of the function $\lambda_m(p)$, see [72].

describing the conservation of mass and momentum (similar to the ones we will use in this thesis later on; see chapter 2), free surface velocity plots like those presented in section 1.2 can be produced [72].

Boettger and Wallace's [8] work also deals with the problem of martensitic phase transformations. Their work involves metastable states between austenite and martensite. The transformation to the final equilibrium state is determined through the use of a "relaxation time." Their expression for the degree of transformation, analogous to equation (1.1), is

$$\frac{d\lambda}{dt} = \frac{\lambda_m(p,T) - \lambda(p,T)}{\tau}\,, \tag{1.6}$$

where λ again represents the degree of transformation, λ_m denotes the metastable state towards which the material is relaxing, and τ is a relaxation time, measuring the speed at which the transformation takes place. The rest of their theory is similar to that of Vlodarchik and Trebinski, described earlier in that the relaxation time τ is fit to each experimental curve.

Next we sketch some of the factors involved in determining the function $\lambda_m(p,T)$, above in (1.6). This determination involves knowing the Gibbs free energy, G, for both the austenite and the martensite phases. These functions, in turn, follow from the Helmholtz free energy, F, by the definition $G = F + p\,\mathrm{v}$, where $\mathrm{v} \equiv 1/\rho$ is the specific volume. Boettger and Wallace propose that the Helmholtz free energy is composed of four pieces, as follows:

$$F = \Phi_0 + F_H + F_A + F_E\,, \tag{1.7}$$

where Φ_0 is the static lattice potential, F_H is the quasi-harmonic phonon free energy, F_A is the an-harmonic contribution, and F_E is the free energy due to thermal excitation of electrons from their ground state. In Boettger and Wallace's work a functional form for each component of the Helmholtz free energy is proposed. Each term involves constants that are approximately known in some way. As before, once the formulation of the free energy is defined, free surface velocity profiles can be computed. The constant τ is chosen for each experiment, so that the computed free

surface profiles match their experimental counterpart as closely as possible.

Both the Vlodarchik–Trebinski and the Boettger–Wallace models are characterized by the idea that it is possible for a mixture of phases to be present at some locations in the sample during the experimental run. This mixture then "relaxes" to some "optimal" mixture that depends on the local conditions. Mixture regions where islands of one phase exist in a sea of another phase are notoriously hard to model precisely in a continuum sense. As a consequence, both models depend on many "effective" material constants and functions that are difficult to obtain. In fact, the idea of a *linear* relaxation time, implicit in equations (1.1) and (1.6), was found [8] to be insufficient to fully capture all the experimental curves presented by Barker and Hollenbach [5] (see the left frame in figure 1-3). The authors concluded that some sort of nonlinear relaxation ought to be taking place inside the material, but did not provide a form for it. How to choose this nonlinear relaxation function is entirely unclear to this author, and a form has not been suggested by other authors. Further theoretical and experimental work will certainly be needed to fully explain the free surface profiles using these ideas.

To address these difficulties, in 1999 Bruno and Vaynblat proposed a new theoretical model that is much simpler than previous ones, and involves only well-known and separately measurable material constants [13, 14]. The Bruno–Vaynblat model, with a simplifying assumption they called the "rarefaction discontinuity approximation", gives qualitatively and quantitatively correct results for both the iron and the graphite-diamond experiments, see figures 1-3 and 1-4. In chapter 2 we provide a full description of the Bruno–Vaynblat model. The mathematical background needed to implement this model is developed in sections 2.1, 2.2 and 2.3, including the rarefaction discontinuity approximation.

Unless otherwise stated, from now on: all references to a mathematical model for austenite–martensite phase transitions in this thesis refer to the Bruno-Vaynblat model. As a means of finishing this chapter we present a simple outline of the major sections of this thesis.

1.4 Summary of the Plan of this Thesis

Below we summarize the plan of this thesis to make navigation of its various parts easier.

- In this chapter 1 (Introduction and Background) we describe the experiments underpinning this work, as well as the theoretical work prior to the Bruno–Vaynblat model.
- In chapter 2 (Bruno–Vaynblat Theory) we introduce the Bruno–Vaynblat model and the solution of the Riemann problem, as well as the appropriate hyperbolic conservation law theory, needed to understand the model.
- In chapter 3 (Bruno-Vaynblat Model without the Rarefaction Discontinuity Approximation) we

  (a) assess the predictions and limitations of the Bruno–Vaynblat model (as implemented by Bruno and Vaynblat);

  (b) implement the model without the rarefaction discontinuity approximation;

  (c) discuss the results of this implementation, including the various new types of wave interactions that we observe; and

  (d) compare the results with the experimental observations, and discuss neglected physical effects whose inclusion could explain some of the discrepancies.

- In chapter 4 (Model Modifications) we consider modifications to the basic Bruno–Vaynblat model, where physical effects that were neglected in the work shown in chapters 1 and and 3 are studied (see item **(d)** in the description of chapter 3 above). Thus

  (a) reasons are given indicating that dissipation may be an important effect, and a model incorporating dissipative effects is introduced. The problems in implementing dissipative effects near the phase transition region are discussed, and a numerical algorithm for doing so is proposed and implemented;

  (b) the results of the implementation of the model with dissipation are compared with the experiments. Since the amount of dissipation that occurs is not a quantity for which we have independent measurements (because of the

very large stresses involved), we give it the value that optimizes the fit between experiment and theory. A discussion of the dissipation value obtained is presented;

(c) a second modification to the model, also studied, has to do with the sound speed near the phase transition point. We argue that the equation of state is not well known in this regime, and study the effects of local (basically, affecting only the sound speed near the phase transition) modifications to the equation of state; and

(d) the results of locally modifying the equation of state are compared with the experimental observations.

- In chapter 5 (Characteristic Tracking Method) we develop a new numerical method for solving one–dimensional hyperbolic systems of conservation laws with phase transitions. This is the method used during the investigations reported in chapter 3, and was developed because of the need for accurate calculations of the interactions of rarefaction waves with discontinuous waves (such as shocks, contact discontinuities, and phase transitions).
- In chapter 6 (Conclusions) we discuss the results of our research, and the areas that need further investigation.
- In appendix A (Lagrangian Formulation) we display various useful formulas for the model equations in Lagrangian coordinates: characteristics and Riemann invariant form, wave (shock and rarefaction) curves,[6] etc.
- In appendix B (Mie-Grüneisen Equation of State) we discuss the equation of state used for most of the investigations in this thesis.
- In appendix C (Conservation of Momentum Discretization) we present the details of the numerical discretization used for the dissipative model equations.
- In appendix D (Summary of the Interface Boundary Conditions used in the Dissipative Code) we give the details of the numerical implementation of the interface boundary conditions, for the model with dissipation.

[6] Needed in the solution of the Riemann problem.

Chapter 2

Bruno–Vaynblat Theory

As mentioned in section 1.3, Bruno and Vaynblat proposed a new model for the shock induced martensitic phase transformations observed in impact experiments. Below we list the assumptions implicit in their model.

2.0.1 Fundamental Postulates

The Bruno–Vaynblat model is based on the following postulates:

1. Because the sample's thickness is so much smaller than its diameter, the problem can be formulated entirely in terms of one–dimensional wave propagation. This assumes that all the waves generated at the lateral edges of the sample do not greatly interfere with the bulk longitudinal motion during the course of the experiment (the time interval during which the free surface velocities are recorded). Prior models made similar assumptions, see [24].
2. Because of the large pressures involved in the α-ϵ iron phase transformation (around 13 GPa, or approximately 1/10-th of the pressure at the center of the earth), the elastic properties of iron can be entirely neglected and only the plastic response of the material is important [24]. This means that the stress tensor can be taken as diagonal, and all the dynamic forcing attributed to a scalar "pressure" function p, so that the equations of solid mechanics simplify greatly. These simplified equations turn out to have the same form as the

equations governing a compressible fluid flow see [22].

Remark 1 *The yield stress for iron reported on in [43] (for tensile tests) was approximately 0.1 GPa, the elastic precursor shock in the Barker and Hollenbach experiments brings the stress in the iron samples to around 1 GPa, well beyond the elastic–plastic boundary, see [12, 20, 24].*

3. From the experimental evidence there is good reason to believe that a relationship of the form $p = p(\mathrm{v})$ provides a good approximation to the behavior in each phase. Here p is the pressure and v is the specific volume, see appendix B. We denote these empirical relationships by $p^A(\mathrm{v})$ for austenite and $p^M(\mathrm{v})$ for martensite. In each phase the function $p = p(\mathrm{v})$ is a convex smooth function, with a negative derivative as required by thermodynamics.
4. The transformation among phases takes place at infinite speed, when some critical value of the pressure is reached. This implies that "continuum level" mixture regions, containing both phases, are not possible. The critical pressures will be denoted by $p^A_{\mathrm{crit}}(T)$ for the forward transformation and $p^M_{\mathrm{crit}}(T)$ for the reverse transformation. We note that this assumption is a limiting case of the theories presented in section 1.3, where the material relaxes to either austenite or martensite over a finite time τ. The Bruno-Vaynblat theory, therefore, corresponds to the limit when $\tau = 0$ and λ can only take the values 0 or 1. Because there is no need to model the poorly understood details of the transformation process, this theory is much simpler than the prior ones.

2.0.2 Mathematical Formulation

From assumptions 2 and 3 in subsection 2.0.1, the governing dynamical equations for the Bruno–Vaynblat model reduce to the conservation of mass and momentum [22]. In an Eulerian frame of reference these are

$$\frac{\partial}{\partial t}\rho + \frac{\partial}{\partial x}(\rho\, u) = 0\,, \qquad \text{and} \qquad \frac{\partial}{\partial t}(\rho\, u) + \frac{\partial}{\partial x}(\rho\, u^2 + p) = 0\,, \tag{2.1}$$

where ρ is the density, u is the particle velocity, p is the pressure, t is the time, and x is the Eulerian spatial position. An equivalent form, in a Lagrangian frame of reference is

$$\frac{\partial \mathrm{v}}{\partial t} - \frac{\partial u}{\partial \xi} = 0\,, \qquad \text{and} \qquad \frac{\partial u}{\partial t} + \frac{\partial p}{\partial \xi} = 0\,, \tag{2.2}$$

where $\mathrm{v} \equiv 1/\rho$ is the specific volume and ξ is the Lagrangian spatial coordinate, related to the Eulerian coordinate x by

$$\xi = \int_{x_0}^{x} \rho(\tilde{x}, t)\, \mathrm{d}\tilde{x}\,, \tag{2.3}$$

where $x_0 = x_0(t)$ is the Eulerian position of a fixed mass particle. From this last equation it should be clear that the Lagrangian spatial coordinate physically represents the amount of mass between a reference particle x_0 and the current Eulerian location x.

Here we will develop the theory in terms of the Eulerian coordinate system. A similar development, in terms of the Lagrangian coordinate system, can be found in appendix A.

From assumption number 4 of the Bruno-Vaynblat model (see subsection 2.0.1), the empirical pressure function $p = p(\mathrm{v})$ has the discontinuous form

$$p(\mathrm{v}) = \begin{cases} p^A(\mathrm{v}) & \text{for } p < p^A_{\mathrm{crit}}(T)\,, \\ p^M(\mathrm{v}) & \text{for } p > p^M_{\mathrm{crit}}(T)\,, \end{cases} \tag{2.4}$$

where we have included a temperature dependence of the critical pressures $p^A_{\mathrm{crit}}(T)$ and $p^M_{\mathrm{crit}}(T)$. However, the experimental evidence suggests that this dependence is quite weak [6, 36], so that a further simplification is introduced, and the temperature dependence of the critical pressure will be neglected, see figure 2-3 (a) for a picture of a typical equation of state. Thus we assume from now on that both p^A_{crit} and p^M_{crit} are known constants. A detailed discussion of the specific functional forms of the individual equations of state ($p^A(\mathrm{v})$ and $p^M(\mathrm{v})$), used for most of the calculations in this thesis, is presented in appendix B.

Remark 2 *The Bruno–Vaynblat model has a relationship, to the models incorporating a detailed calculation of the phase transformation, similar to that of the Chapman–Jouget to the ZND model in combustion theory [27]. There the reactant and the product each have their own equation of state, with the Chapman-Jouget theory modeling the reaction as instantaneous and the ZND theory modeling the details of the chemical reactions involved.*

When $p = p(\mathrm{v})$ is a convex smooth function with negative derivative, the system in (2.1) — equivalently, in (2.2) — is known as the *p-System*, and has been extensively studied in the mathematical literature, see [65]. In the Bruno–Vaynblat theory, because of the switch in the equation of state at the critical pressure, p is neither convex nor continuous, and further assumptions are needed to have a complete theory. These assumptions will be explained in the sections that follow.

2.1 The Continuous p-System

In this section we will consider the system of equations in (2.1) — equivalently, in (2.2) — and assume that $p = p(\mathrm{v})$ is a convex smooth function of the specific volume v, with a negative derivative. These requirements will be weakened in later sections. It is well known [65] that in this case the system of equations in (2.1) is a strictly hyperbolic system of conservation laws — well–posed even for discontinuous solutions — provided that the correct Entropy condition and Rankine–Hugoniot jump conditions are used at the discontinuities (shocks). Next we summarize the most relevant (for our work here) theoretical facts about these equations.

2.1.1 Fundamental Ideas

The characteristic form of the equations in (2.1) is given by

$$\frac{dp}{dt} - \rho\, c \frac{du}{dt} = 0 \qquad \text{along} \qquad \frac{dx}{dt} = u - c\,, \tag{2.5}$$

$$\frac{dp}{dt} + \rho\, c \frac{du}{dt} = 0 \qquad \text{along} \qquad \frac{dx}{dt} = u + c\,, \tag{2.6}$$

where the sound speed $c > 0$ is defined by $c^2 \equiv \dfrac{dp}{d\rho}$. We will call the set of characteristics given by $\dfrac{dx}{dt} = u - c$, the C_- **or 1-characteristics**; while the characteristics given by $\dfrac{dx}{dt} = u + c$ will be called the C_+ **or 2-characteristics.**

The equations can also be written in Riemann Invariant form as

$$\left.\begin{array}{rcll} \dfrac{ds}{dt} & = & 0 \quad \text{along} & \dfrac{dx}{dt} = u - c\,, \\ \dfrac{dr}{dt} & = & 0 \quad \text{along} & \dfrac{dx}{dt} = u + c\,, \end{array}\right\} \tag{2.7}$$

where $s = u - l(p)$ is the *left Riemann invariant* (constant along each C_- characteristic), $r = u + l(p)$ is the *right Riemann invariant* (constant along each C_+ characteristic), and $l(p)$ is given by

$$l(p) = \int_{p'}^{p} \frac{\mathrm{d}p}{\rho c} = \int_{\rho'}^{\rho} \frac{c}{\rho}\,\mathrm{d}\rho\,, \tag{2.8}$$

where $p' = p(\mathrm{v}')$ is some fixed reference state. The Riemann invariants s and r will play a major role in the numerical method developed in chapter 5.

Flow in which one of the Riemann invariants is identically constant is called a *simple wave.* In a simple wave the characteristics that correspond to the other Riemann invariant are straight lines. We will call a simple wave *right-facing* or a right simple wave if the fluid particles (traveling with velocity u) enter the simple wave region from the right; equivalently: when s is identically constant on the wave. Similarly, if the fluid particles enter the simple wave from the left (i.e.: when r is identically constant on the wave), we will call the wave *left-facing* or a left simple wave. Furthermore, we will call a simple wave *expansive or rarefying* (respectively: *compressive*), if the pressure and density on a fluid parcel decrease (respectively: increase) as the particles cross the simple wave region. This corresponds to the characteristics carrying the simple wave diverging (respectively: converging). An extreme case of this occurs when the characteristics diverge (respectively: converge) from a single point, in which case we talk about a *rarefaction fan* (respectively: *a compression fan.*) Figure 2-1 shows an example of a right-facing expansive simple wave on the left frame, and an

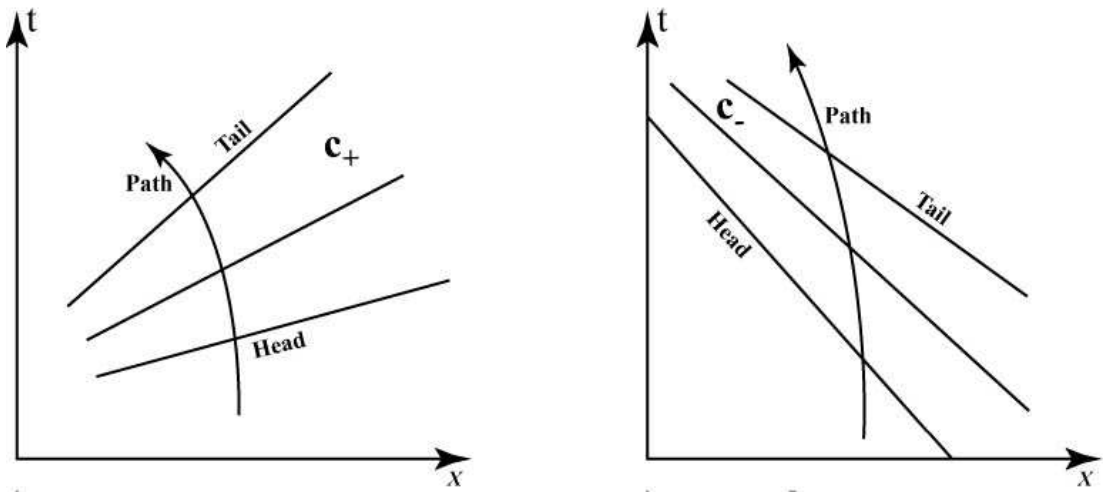

Figure 2-1: Examples of simple waves, with a typical path for a fluid particle shown (thick line). **Left:** Simple expansive wave on the C_+ characteristics (i.e.: a right simple expansive wave). **Right:** Simple compressive wave on the C_- characteristics (i.e.: a left simple compressive wave). In each case the head characteristic (the first characteristic in the simple wave that a particle crosses as it enters the simple wave flow), the tail characteristic (the last characteristic in the simple wave that a particle crosses as it leaves the simple wave flow), and a typical characteristic are shown.

example of a left-facing compressive simple wave on the right frame.

The solutions to the system of equations in (2.1) will in general develop discontinuities in a finite time, even for smooth initial data. These discontinuities must satisfy the Rankine–Hugoniot jump conditions and the Entropy condition, whose form we display below using Eulerian coordinates. An entirely analogous formulation can also be made using Lagrangian coordinates.

The *Rankine–Hugoniot jump conditions* are given by

$$-S_E\,[\rho] + [\rho\,u] = 0\,, \qquad \text{and} \qquad -S_E\,[\rho\,u] + \left[\rho\,u^2 + p\right] = 0\,, \tag{2.9}$$

where S_E is the speed of the discontinuity in Eulerian coordinates and the brackets denote the jump in the enclosed quantity across the shock. Specifically: $[Q] = Q^l - Q^r$, where Q^l (respectively Q^r) is the limiting value of Q — from the left (respectively, from the right) — at the discontinuity.

The *Entropy condition* states that the pressure and density must increase as a

fluid particle crosses the shock. For a right–facing shock or right shock, defined by the fact that the fluid enters the shock from the right, the Entropy condition in Eulerian coordinates is equivalent to:

$$u^r + c^r < S_E < u^l + c^l \,, \tag{2.10}$$

where the superscripts l and r are as above, in the definition of the bracket notation used in equation (2.9). In other words, the C_+ characteristics converge on the shock. Similarly, for a left–facing shock or left shock, the Entropy condition in Eulerian coordinates is equivalent to:

$$u^r - c^r < S_E < u^l - c^l \,, \tag{2.11}$$

so that the the C_- characteristics converge on the shock.

The numerical codes we use in this thesis are of the Godunov type, and are based on having a solver for the *Riemann Problem*. The Riemann problem for the equations in (2.1) is the initial value problem with "step" initial values. Namely:

$$p(x,0) = \begin{cases} p^l & \text{for } x < x_0 \,, \\ p^r & \text{for } x > x_0 \,, \end{cases} \quad \text{and} \quad u(x,0) = \begin{cases} u^l \text{ for } x < x_0 \,, \\ u^r \text{ for } x > x_0 \,, \end{cases} \tag{2.12}$$

where x_0 is the position of the initial discontinuity, and the initial left (p^l, u^l) and right (p^r, u^r) states are constant.

The general solution to the Riemann problem for the equations in (2.1) is well known. It is self–similar (depends on $\zeta = x/t$ only) and consists of two waves separating three constant states:

- the left state, valid for $\zeta < \zeta_l$,
- the middle state, valid for $\zeta_{ml} < \zeta < \zeta_{mr}$, and
- the right state, valid for $\zeta_r < \zeta$,

where $\zeta_l \le \zeta_{ml} < \zeta_{mr} \le \zeta_r$. The right wave, on $\zeta_{mr} \le \zeta \le \zeta_r$, belongs to the C_+ characteristic family, and it can either be a right shock (in which case $\zeta_{mr} = \zeta_r$)

or a right rarefaction fan (in which case ζ_{mr} and ζ_r correspond to the tail and head, respectively, of the fan). The situation for the left wave (on $\zeta_l \leq \zeta \leq \zeta_{ml}$ and belonging to the C_- characteristic family) is similar. Figure 2-2 shows a space–time diagram with an example of one of the four possible cases for the solution of a Riemann problem. In this case the solution involves a left–facing C_- rarefaction fan and a right–facing C_+ shock.

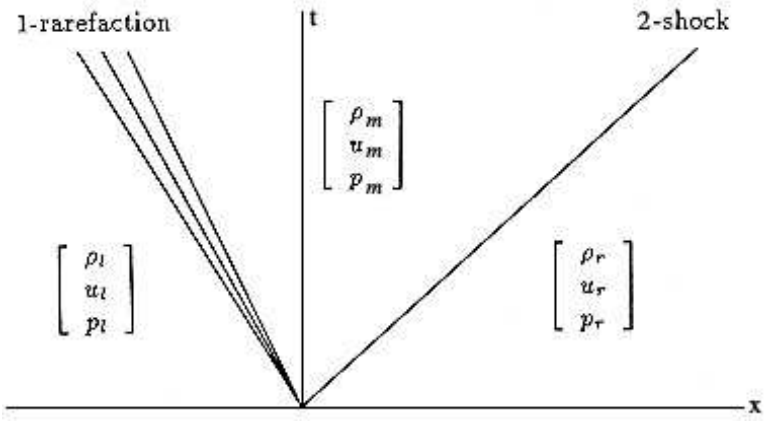

Figure 2-2: Space–time diagram for a typical solution of the Riemann problem, for the continuous convex p-System (system in (2.1), with $p = p(\mathrm{v})$ smooth, convex, with a negative derivative). In this example the C_- or 1-wave is a rarefaction and the C_+ or 2-wave is a shock.

The *solution to the Riemann problem in (2.12) is constructed as follows:* **First:** two solution wave curves in phase space[1] are constructed, one corresponding to each of the states in the initial values. The *left wave curve* consists of all the possible states that can be connected to the left state (p^l, u^l) by either a 1-rarefaction fan or a 1-shock. The *right wave curve* consists of all the possible states that can be connected to the right state (p^r, u^r) by either a 2-rarefaction fan or a 2-shock. **Second:** The intersection of these two curves is found. The middle state in the solution to the Riemann problem is then given by this intersection, say (p^m, u^m). The two waves in the solution to the Riemann problem are given by the corresponding waves in each curve, connecting (p^m, u^m) to either (p^l, u^l) or (p^r, u^r).

[1]Here we mean by *phase space* the set of all the possible values that the solution can take at any point. A point in phase space is determined by a velocity and a density, or a velocity and a pressure, etc.

Notice the following about the general construction of the solution to the Riemann problem:

1. For a given initial state, say $(p,\ u)$ — i.e.: either of $(p^l,\ u^l)$ or $(p^r,\ u^r)$ above — two wave curves can be constructed: a 1-wave curve involving 1-shocks or 1-rarefactions and a 2-wave curve involving 2-shocks or 2-rarefactions. The two are related by the reflection symmetry of the equations ($x \to -x$ and $u \to -u$ leaves the equations invariant), so that the construction of only one of the wave curves needs to be described.

2. Each wave curve is composed of two branches: the shock or Hugoniot branch (states where the connection is by a shock wave), and the rarefaction branch (states where the connection is by a rarefaction wave).

In the next subsection we describe the construction of the wave curves for the case of the convex, continuous p-system. Later, in section 2.2, we will see how this construction must be modified for the case when a phase transition is present, and $p = p(\mathrm{v})$ is no longer smooth or convex.

2.1.2 Shock and Rarefaction Wave Curves

In the derivation of wave curves below we start by assuming that we know the state ahead of the wave,[2] $\Sigma^a = (p^a, u^a)$, and then we find the states that can be connected to the given state by either a shock or a rarefaction fan. We parameterize the curves using the pressure behind the wave, p^b. Notice that, for both shocks and rarefaction waves, the state behind the wave must satisfy the equation of state $p^b = p(\mathrm{v}^\mathrm{b})$. Thus: if we know the pressure behind the wave, we also know its specific volume, from $\mathrm{v}^\mathrm{b} = \mathrm{p}^{-1}(\mathrm{p}^\mathrm{b})$ — this rather trivial observation greatly simplifies the procedure for calculating the wave curves.[3]

[2] For a right (respectively: left) wave, the state ahead is the state to the right (respectively: left) of the wave.

[3] The $(p,\ \mathrm{v})$ projections of the wave curves (shock and rarefaction) are always given by the $p = p(\mathrm{v})$ relationship.

The equations for the shock branches of the wave curves follow upon manipulation of the equations in (2.9), which yields:

$$u^b = u^a \pm \sqrt{-[\mathrm{v}][\mathrm{p}]}\,, \qquad \text{and} \qquad S_E = u^a \mp \mathrm{v}^{\mathrm{a}} \sqrt{-\frac{[\mathrm{p}]}{[\mathrm{v}]}}\,, \tag{2.13}$$

where $[\mathrm{v}] = \mathrm{v}^{\mathrm{a}} - \mathrm{v}^{\mathrm{b}} > 0$, $[p] = p^a - p^b < 0$ (the inequalities here follow from the entropy condition), and the upper (respectively: lower) signs in the square roots must be used for a right (respectively: left) wave.

The equations for the rarefaction branch of the wave curves follow from equations (2.7) and (2.8), upon implementing the condition that one of the invariants is constant across the wave. Thus we obtain for the velocity:

$$u^b = u^a \mp \int_{p^a}^{p^b} \frac{dp}{\rho\, c}\,, \qquad \text{where} \qquad c = \sqrt{\frac{dp}{d\rho}} = \mathrm{v} \sqrt{-\frac{\mathrm{dp}}{\mathrm{dv}}}\,, \tag{2.14}$$

and the upper (respectively: lower) sign must be used for a right (respectively: left) wave. Notice the analogy between the formula for the shock speed in (2.13), and the formula for the characteristic speed (corresponding to the nonconstant Riemann invariant) in the rarefaction wave in (2.14), namely: $u^b \pm c^b$ — which is the basis for the rarefaction discontinuity approximation, introduced later in subsection 2.3.1.

To summarize: given Σ^a, p^b, and v^{b}, from the first equation in (2.13) — or (2.14) — we can obtain the particle velocity behind a shock — or a rarefaction fan. Therefore, the complete state behind the wave is known once the pressure behind the wave is specified, so that we have a complete procedure for the determination of the shock and the rarefaction branches of the wave curves.

2.2 The Non-Continuous p-System

In this section we will discuss the differences that arise in the solution to the Riemann problem when a non-convex, non-continuous, $p = p(\mathrm{v})$ relationship — such as the one given by equation (2.4) — is used. The left frame in figure 2-3 shows a typical plot

for a $p = p(\mathrm{v})$ relationship of the type we will consider here.

2.2.1 Riemann Problem Solution

As in the standard case for the p-System, the solution of the Riemann problem consists of three constant states separated by two self-similar waves. These two waves are a left-facing 1-wave and a right-facing 2-wave. Each wave can be either a single rarefaction fan or a single shock front, or it can be a *generalized wave*: a group of several elementary self-similar waves that belong to the same characteristic family [54]. The possibility of generalized waves distinguishes the Riemann problem for materials with equation of state given by equation (2.4) from the standard Riemann problem – where the two waves are always either a rarefaction fan or a shock wave.

When the 1- and 2-wave curves are known, the Riemann problem under consideration is then solved in the same manner as in standard situations, i.e. the intersection of these two wave curves gives the middle state and the path to this intersection along the wave curves gives the left-facing and right-facing waves. Thus, the solution of the Riemann problem is reduced to construction of wave curves. Remember that a wave curve is a generalization of the shock and rarefaction curves to the case where generalized waves are possible [54].

A contact discontinuity is not a possible wave type in the case when $p(\mathrm{v})$ is a continuous convex function of v. Here, however, in the particular case of a Riemann problem involving two different materials or two different phases a contact discontinuity is possible. In these cases the solution to the Riemann problem consists of as before a left-facing wave and a right-facing wave but separated now by a contact moving at the velocity of the particles in the middle state.

2.2.2 Generalized Wave Curves

Because of the reflectional invariance of equations (2.1), in this section we restrict attention to right-facing waves. The left-facing wave curve for a given initial state Σ^a is the reflection of the right-facing wave curve for the same initial state through

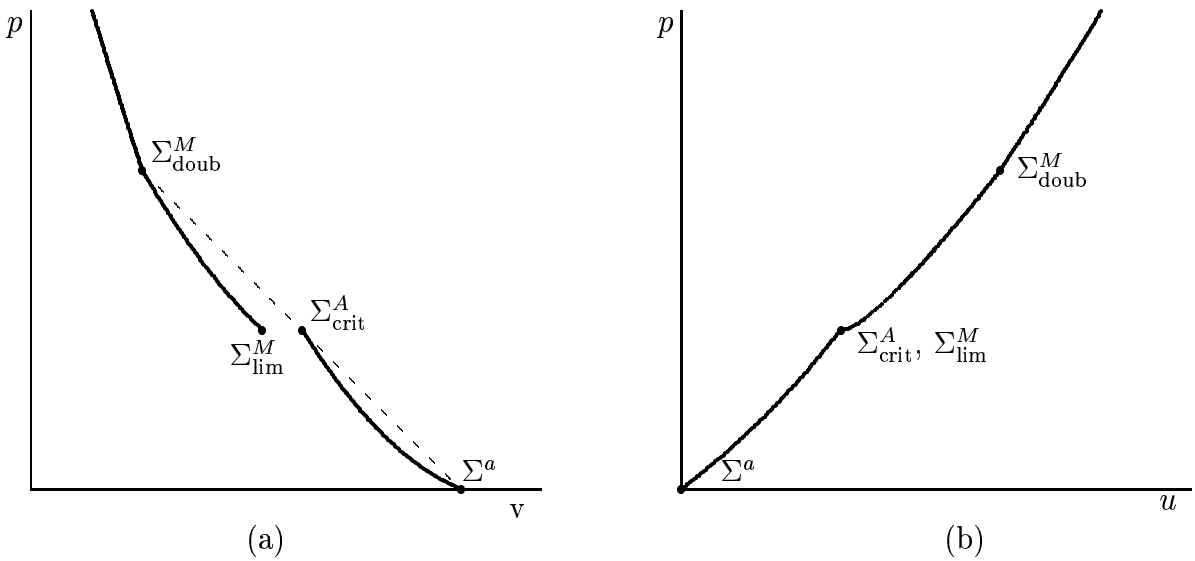

Figure 2-3: Compression branch of the austenite–centered wave curve. The projections of the wave curve are given by the thick solid lines. The thin dashed line is the Rayleigh line. **Left (a):** Projection onto the (v, p)–plane. **Right (b):** Projection onto the (u, p)–plane.

the plane $u = u^a$. Also because of the Galilean invariance of equations (2.1) we will assume the velocity ahead of the wave to be zero, $u^a = 0$.

2.2.3 Austenitic Initial State

In this subsection we construct the wave curves for austenitic initial states. The expansion branch ($p^b < p^a$) has a very simple structure: it is a regular rarefaction curve discussed in subsection 2.1.2. Thus we focus on the compression branch ($p^b > p^a$), which is more complex: it consists of three different sub-branches.

Austenitic States and Curves

1. When the pressure behind the wave is below the critical pressure of austenite ($p^b < p^A_{\text{crit}}$), this portion of the wave curve is the same as the standard shock curve discussed in subsection 2.1.2, (see figure 2-4 (a)).

2. For pressures behind the wave greater than the critical pressure ($p^b > p^A_{\text{crit}}$), the state after this wave must be martensite and a shock cannot be used to connect the two states or else the entropy condition (2.10) will not be met. The correct

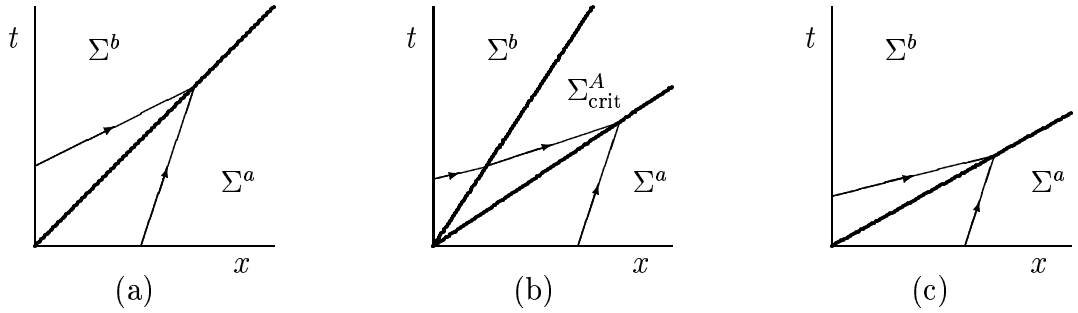

Figure 2-4: Space–time representations of right waves connecting the initial state Σ^a with states Σ^b from the compression branch of the austenite–centered 3–wave curve. From left to right, the state Σ^b belongs to: **(a)** The first compression sub-branch; **(b)** The second compression sub-branch; and **(c)** The third compression sub-branch. The trajectories of discontinuity fronts are represented by thick lines and the C_+ characteristics by thin lines.

way to resolve this difficulty is to split the jump to p^b into two pieces, a jump to the critical state p^A_{crit} followed by another jump to the pressure p^b. This is an example of a split wave. The first jump to the critical pressure is simply a shock whose final state corresponds to the critical pressure of austenite. The second jump to the martensitic branch of the equation of state is a *forward critical phase transformation wave*, (see figure 2-4 (b)).

3. For pressures greater than a special value ($p^b > p_{\text{doub}}$) again the entropy condition is met. For pressures in this range the state ahead and behind are connected by a single *forward phase transformation wave*, (see figure 2-4 (c)).

2.2.4 Martensitic Initial State

In this section we describe the wave curves for martensitic initial states. In this case the compression branch ($p^b > p^a$) has a very simple structure: it is a regular shock curve discussed in subsection 2.1.2. Thus, we may focus on the more interesting branch, the expansion branch, which displays more complexity: it consists of three different sub-branches.

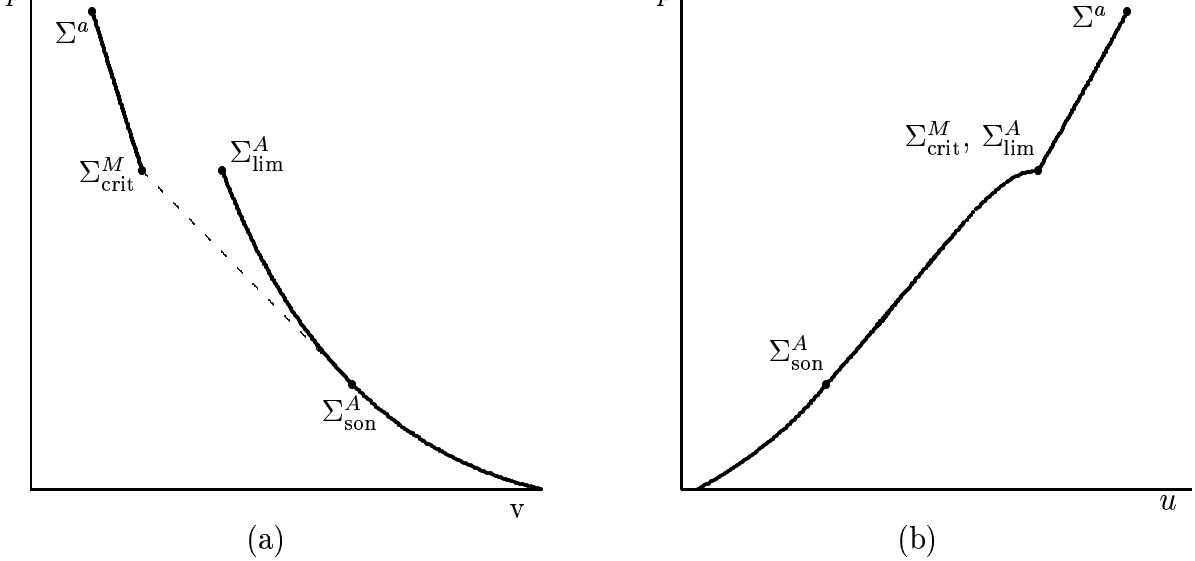

Figure 2-5: Expansion branch of the martensite–centered wave curve. The projections of the wave curve are given by the thick solid lines. The thin dashed line is the Rayleigh line. **Left (a):** Projection onto the (v, p)–plane. **Right (b):** Projection onto the (u, p)–plane.

Martensitic States and Curves

1. When the pressure behind the wave is above the critical pressure of martensite ($p^b > p^M_{\text{crit}}$), this portion of the wave curve is the same as the standard rarefaction wave curve discussed in subsection 2.1.2, (see figure 2-6 (a)).

2. For pressures behind the wave below the critical pressure of martensite ($p^b < p^A_{\text{crit}}$), the state after this wave must be austenite. The correct way to connect these two waves is again through a split wave. The jump to p^b is split into two transitions. The first transition corresponds to a rarefaction fan from the initial state to the critical state for martensite. The second transition corresponds to a *backwards critical phase transformation*, a shock like wave from the critical pressure of martensite to the final state on the austenitic branch. This is another example of a split wave, (see figure 2-6 (b)).

3. For pressures below a special value ($p^b < p_{\text{lim}}$) again the type of wave changes. In this case the transition to the final pressure p^b is broken into three transitions. The first transition involves a rarefaction fan to the critical pressure of martensite. The second component involves a backwards phase transformation

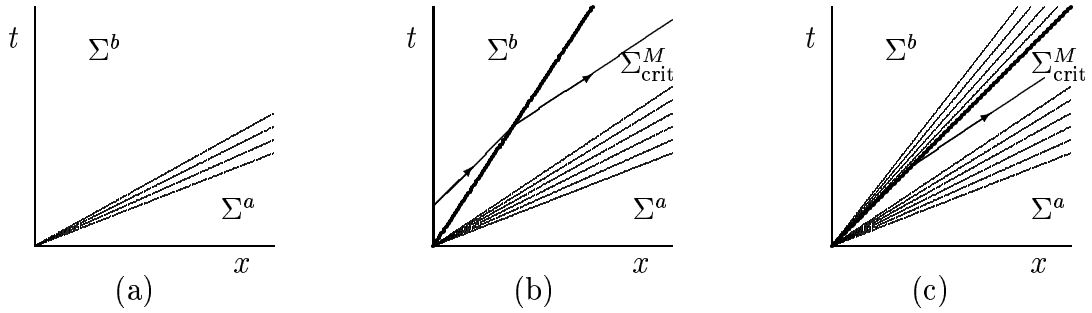

Figure 2-6: Space–time representations of right waves connecting the initial state Σ^a with states Σ^b from the expansion branch of the martensite–centered right wave curve. From left to right, the state Σ^b belongs to: **(a)** The first expansion sub-branch; **(b)** The second expansion sub-branch; and **(c)** The third expansion sub-branch. The trajectories of discontinuity fronts are represented by thick lines and the C_+ characteristics by thin lines.

front to this limiting pressure and the third component involves a rarefaction fan in austenite to the final state, (see figure 2-6 (c)).

2.2.5 Remarks on the Riemann Problem

For a material characterized by the equation of state (2.4), the specifics of the Riemann problem stem from the peculiarities of the corresponding wave curves as constructed in subsection 2.2.2. The following properties of these wave curves play a crucial role in the solution of the Riemann problem.

1. The wave curves consist of several sub-branches; the analytical descriptions of which are different for each sub-branch.

2. A given sub-branch is always either a shock curve or a rarefaction curve; however the state at which this shock or rarefaction curve is centered is not necessarily the state at which the entire wave curve is centered.

3. Although the curves themselves in the $(\mathrm{v}, \mathrm{p}, \mathrm{u})$-space are discontinuous[4], their projections onto the (p, u)-plane are continuous piece-wise smooth, monotonic

[4]The specific volume $\mathrm{v^b}$ jumps at $\mathrm{v^b} = \mathrm{v^A_{crit}}$ on an austenite-centered curve and at $\mathrm{v^b} = \mathrm{v^M_{crit}}$ on a martensite-centered curve; see figures 2-3 (a) and 2-5 (a).

function. The left-facing wave curves are monotonically decreasing and the right-facing wave curves are monotonically increasing. Both curves are defined on the infinite intervals $-\infty < u < +\infty$ and $0 < p < +\infty$; see figures 2-3 (b) and 2-5 (b).

Property 3 immediately implies that the intersection of any two wave curves of the opposite families exists and is unique; thus, there exists one and only one solution of the Riemann problem. It then follows from property 2 that the Riemann problems considered here may be solved in a manner similar to that encountered in standard cases.

2.3 Initial Value Problems

In the experiments of section 1.2, the problem starting at the exact instant of time when the impactor and the target collide, can be modeled by a Riemann problem. In this Riemann problem the left state is given by $(p_l, u_l) = (0, u_f)$ and the right state is given by $(p_r, u_r) = (0, 0)$, where u_f is the velocity of the flyer, and we approximate atmospheric pressure as zero based on the extreme pressures experienced in the sample during the experimental runs. This Riemann problem can be solved, and the flow field evolved, for a small time forward: up until the first wave interaction occurs. If the two waves that interact next are "thin" (either a shock, a transformation front or a contact discontinuity[5]) then the collision can be resolved by solving another Riemann problem at the point of their collision. In fact interactions between only one-dimensional thin discontinuities (shocks, transformation fronts and contacts) require only the solution of Riemann problems, and as long as these are the only types of waves present, the flow can be evolved forward using the solution of Riemann problems. It is in the production of a continuous wave, like a rarefaction wave, where the further solution of the flow using only a Riemann solver is limited. Interactions involving continuous rarefaction waves and discontinuities, for example, typically require full numerical simulations

[5]In this system a contact discontinuity arises at the boundary between two phases only. For example at the iron vacuum boundary.

to resolve, and one cannot a priori using only a small number of Riemann solutions continue the flow to a desired point in time. If, however, the rarefaction waves found are sufficiently weak, they may be accurately approximated by discontinuities, and a Riemann solver is all that is needed.

In order to avoid having to do a full numerical simulation of the impact problem, Bruno and Vaynblat numerically solved the flow problem using the simplifying assumption of weak rarefaction fans. This approximation, called the *rarefaction discontinuity approximation*, is described below.

2.3.1 Rarefaction Discontinuity Approximation

The assumption of weak waves — where the wave strength is measured by any of the three quantities $[p]/p^a$ or $[\mathrm{v}]/\mathrm{v}^\mathrm{a}$ or $[u]/\mathrm{v}^\mathrm{a}\mathrm{C}^\mathrm{a}$ — allows rarefaction fans to be approximated by discontinuities, hereafter called *rarefaction discontinuities*[6]. When the physical solution requires a rarefaction fan, a discontinuity is inserted carrying the same jump as the original fan and moving at a speed comparable with the two fan edges. As discussed above, under such an approximation all wave interactions can be resolved, using only a Riemann solver. A validation of this approximation procedure, can be found in [18]. In particular, it follows from [18, p. 156] that the errors in replacing a true rarefaction fan with a discontinuity are of the third order in the wave strength.

Remark 3 *Historically rarefaction discontinuity approximations of this type have been used in many contexts. In the solid dynamics community, a special case of this approximation called — the "free surface approximation" — has been widely used in studies of rarefaction fans arising from the reflection of shocks at free surfaces [76]. A detailed treatment of the degree to which the free surface approximation is valid can be found in [74]. The first explicit use of the "general" rarefaction discontinuity approximation in a Riemann solver can be attributed to [15]. A detailed discussion*

[6]Here again $[Q]$ represents the jump in Q, see subsection 2.1.2.

of a Riemann solver in which fans are approximated by discontinuities can be found in [23].

In a typical experiment the impact on the target induces one or two discontinuous propagating fronts in the target and one or two discontinuous propagating fronts in the flyer (see the compressive sub-branches of the austenitic centered initial state, subsection 2.2.3). These wave patterns account for the initial stages of the experiment, up to the time when the leading wave reaches a material boundary — such as the free surface in the experiments of [5]. For later times, however, the wave structure inside the impactor-flyer system is more complicated. It includes all waves reflected from material boundaries, any secondary waves born in interaction of reflected and incoming waves, etc, so that as time evolves, many waves are generated through reflections and interactions.

If in accordance to the rarefaction discontinuity approximation every wave produced by the Riemann solver is approximated by a discontinuity, then every state in the flow diagram is constant, and correspondingly so is every wave velocity. A great simplification arises in computing the evolution of the flow profile. At any given time we can compute the pair of waves that intersects next, by simply comparing, in turn, each pair of waves and recording the specific pair that intersects first. From this point we can continue to evolve the flow by solving the Riemann problem that results from the collision of the two discontinuous waves. By solving one Riemann problem at a time in this manner one can move the flow forward in time, from any given initial condition of constant states.

Bruno and Vaynblat implemented a numerical code incorporating the rarefaction discontinuity approximation in [13]. The results of the numerical predictions of the free surface velocities were presented in section 1.2. The results for the α-ϵ iron phase transformation, are presented in figure 1-3 (page 18), and for the graphite-diamond phase transition presented in figure 1-4 (page 20).

In the next chapter we will discuss how well the rarefaction discontinuity approximation predicts the experimentally observed free surface plots and analyze the experimental and theoretical data sets in greater detail. Further into this thesis, the

discrepancies between the model and the experiments will be considered, and modifications to the model including physical effects neglected in the original formulation by Bruno and Vaynblat will be introduced and studied.

Chapter 3

Bruno-Vaynblat Model without the Rarefaction Discontinuity Approximation

The plan of this chapter is as follows:

- In section 3.1 (Assessment of the Discontinuous Bruno-Vaynblat Model) we asses the predictions of the Bruno–Vaynblat model as implemented by Bruno and Vaynblat. The degree to which it fits the experimental data is analyzed and possible causes for the disagreements are proposed.

- In section 3.2 (Full Bruno-Vaynblat Model, Including Fans) the Bruno–Vaynblat model is implemented in full, without the rarefaction discontinuity approximation. The results of this implementation, including several new types of wave interactions that are observed in the numerical runs, are discussed. The predictions of the full model are compared with the experiments, and the improvements (relative to the earlier partial implementation by Bruno and Vaynblat) are discussed, as well as the remaining discrepancies.

- In section 3.3 (Additional Physical Effects) we discuss several physical effects neglected by the Bruno–Vaynblat model which may be responsible for the rel-

atively small discrepancies with the experimental data. In the chapters that follow this one, we propose and study ways to add two of these effects.

3.1 Assessment of the Discontinuous Bruno-Vaynblat Model

When one looks at the results obtained with the rarefaction discontinuity approximation, one cannot help but be amazed by the agreement with experiment. In these impact experiments the pressure jump the material experiences are on the order of $10^9\,Pa$. At these large pressures the rarefaction waves can hardly be considered weak. Thus it is entirely possible that the rarefaction wave approximation is loosing some important feature of the problem. One of the purposes of the work done by this author is to go beyond this approximation and learn what features of the free surface profiles are dependent on it. Therefore, in the hopes of further improving the results of Bruno and Vaynblat, in this section we concentrate on the qualitative *disagreements*, between their theoretical curves and the experimental ones. The observations made here will then form the basis for the modifications made by this author in later sections. The two sets of curves, shown in figure 1-3 (page 18) differ in at least the following fundamental points:

- The rarefaction discontinuity approximation produces free surface velocity profiles that are "too steep". The experimental profiles numbered 1 and 17, have a steep, but *finite* slope (representing the increase in velocity achieved during the second wave). The predictions of the rarefaction discontinuity approximation, however, give infinite rise times for the second wave in each experiment. The experimental curve numbered 1 has the most shallow rise time for the second wave, and correspondingly the worst match with theory.

- The rarefaction discontinuity approximation produces corners that are "too sharp". The experimental profiles numbered 17 and 6 have smooth transitions between the jump accompanying the second wave and the limiting asymptotic

velocity each assumes. The rarefaction discontinuity approximation, however, gives sharp angular corners at these locations on the graphs.

- For long times the rarefaction discontinuity approximation predicts a constant asymptotic value of free surface velocity. Many of the experimental curves have free surface velocities, however, are not constant for large values of time.

- The initial rise of the first wave in the rarefaction discontinuity plots are not prefixed by a tiny "toe" around the Time/Thickness of $0.2\,s/km$. In the experimental plots the first jump in free surface velocity is preceded by a relatively small jump before the Time/Thickness of $0.2\,s/km$, that is not present in the theoretical plots. We note here that it is believed that this "toe" is caused by elastic effects see, section 1.2, while the remaining curves are produced by the plastic response of iron. It is only the waves propagation occurring in the plastic iron, that is modeled and all approximations will neglect this toe.

The approach taken for the remainder of this thesis is to keep the basis of the Bruno-Vaynblat theory of martensitic phase transformations but to add new effects in a hope of removing some or all of the disagreements mentioned above. It is felt that the disagreement with respect to the slopes of the free surface plots, (first item mentioned), is the most important of all affects to try and capture. One obvious point that would need to be introduced into the theory if we are to hope for better agreement is:

A smoothing effect had to be incorporated.

As an aside, it is not surprising that the free surface plots constructed out of discontinuities should give rise to very "sharp" and angular results. The very components that the solution is built from have this property. From the results shown in figure 1-3, created with the rarefaction discontinuity approximation, it seemed obvious that the first attempt at improving the model should be that of removing the approximation and evaluating numerically the full equations.

To fully resolve the rarefaction fans, two numerical schemes were implemented. These codes enabled the study, in a controlled environment, of the effects that including fans have on the free surface velocity plots.

3.2 Full Bruno-Vaynblat Model, Including Fans

In this section we present predictions that the full Bruno-Vaynblat theory gives including rarefaction fans in the different impact regimes corresponding to the experimental setups of Barker and Hollenbach [5]. The complete numerical flows, presented below, were constructed using two numerical schemes:

1. A Godunov type initial value solver.

2. A new numerical scheme, called the *Discontinuity Tracking Method*, developed in the course of working on this problem, see chapter 5.

Both numerical schemes give the same results and we present all plots using the discontinuity tracking method as it is much better at resolving the features of the flow. The qualitative predictions, presented here, are illustrated with figures which resulted from numerical simulations, utilizing actual material constants — obtained as indicated in Appendix B.

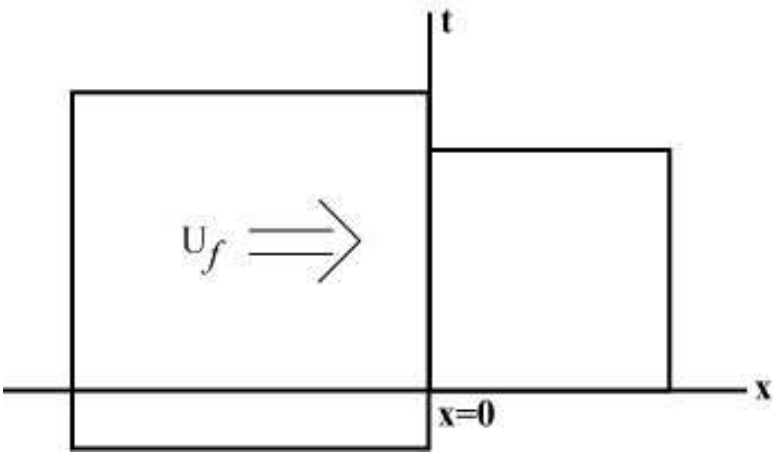

Figure 3-1: A cartoon of the impact experiments. The origin of the (x,t)-diagrams is shown.

The following key is helpful in interpreting the (x,t)-plots:

1. A simple cartoon showing the location of the space time origin and the first Riemann problem solved is shown in figure 3-1.

2. Shocks are printed using a *thick solid black* line.

3. Forward transformation fronts are printed using a *thick dotted black* line.

4. Contact discontinuities are printed using a *thick dot-dashed black* line.

5. Backwards transformation fronts are printed using a *thick long dashed* line.

6. A few sample characteristics are printed using *thin gray* lines. More will be said about these numerical waves in chapter 5.

7. Constant state regions are printed in pure *white*.

3.2.1 Three Qualitative Regimes

In the experiments reported on in [5], both the target and the impactor were made of pure iron. The monitored interface was open to the air and for all practical purposes unconstrained. We see from the experimental pictures, presented in section 1.2, that different flyer velocities, u_f, can give rise to qualitatively different wave patterns. In this section we discuss some of the wave patterns that are achievable; in the context of the full Bruno-Vaynblat model. The results presented here motivate and explain many of the improvements made in later sections.

We begin by considering the initial configuration $\Sigma(x, t_1)$ of states at the impact time $t = t_1$, for which we use the following notation:

$$\Sigma(x, t_1) = \begin{cases} \Sigma_0^I\,, & \text{for } x < x_1\,, \\ \Sigma_0^T\,, & \text{for } x_1 < x < x_1 + L\,, \\ \Sigma^{\text{Vac}}\,, & \text{for } x_1 + L < x\,, \end{cases} \tag{3.1}$$

where x_1 is the position of the interface between the target and the impactor at the impact time, t_1, and L is the initial length of the target. The initial state of the impactor is iron, in the austenitic phase, at zero pressure, and moving at a speed u_f.

The initial state of the target is the same as that of the impactor but moving at a velocity of 0. From this information we can write the initial states of the two iron pieces and the vacuum state as

$$\Sigma_0^I = (0, u_f)\,, \qquad \Sigma_0^T = (0,0)\,, \qquad \Sigma^{\text{Vac}} = (0,0)\,. \tag{3.2}$$

This information and equation (3.1) define the first Riemann problem (RP_1), centered at (x_1, t_1) with left state Σ_0^I and right state Σ_0^T, see figure 3-2.

The collision between the flyer and the target will impart a compressive force on the sample and impactor. The 1-st Riemann problem will have different types of solutions depending on the magnitude of u_f (see the discussion of the austenitic centered wave curve in subsection 2.2.3). Here we classify into three different parameter regimes the different qualitative wave profiles that result.

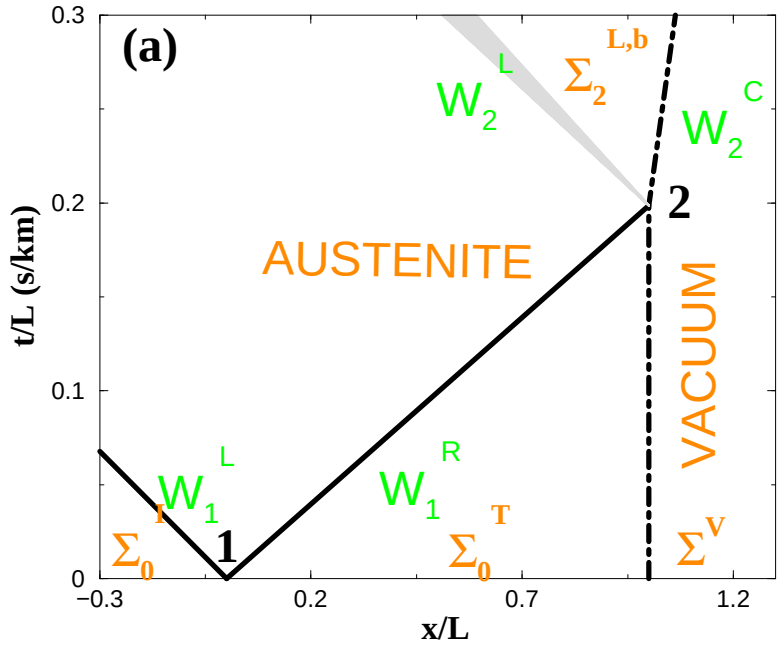

Figure 3-2: An impact in regime A. (x,t)-diagrams for the α-ϵ iron phase transition. Horizontal axis is the spatial coordinate x scaled by the sample thickness. The vertical axis is time t scaled by the sample thickness.

Regime A: In this regime the compressive force from the flyer is not large enough to produce a phase transition and upon impact, only one discontinuity (a shock)

develops in each of the target and flyer. A typical (x,t)-diagram of this regime is depicted in figure 3-2. The solution to Riemann problem 1 (labeled with a 1 in figure 3-2) consists of three constant austenitic states: the initial left state Σ_0^I, a constant middle state Σ_1^M, and the initial right state Σ_0^T, separated by two waves: a 1-shock front W_1^L and a 2-shock front W_1^R.

The solution of the full problem coincides with the solution of this Riemann problem up until the time, t_2, when the discontinuity reaches the free surface. To continue the solution of the impact problem beyond this time, one needs to solve a second Riemann problem (RP_2), centered at (x_2,t_2) the initial data of which is given by

$$\Sigma_2^L = \Sigma_1^M \qquad \text{and} \qquad \Sigma_2^R = \Sigma^{\text{Vac}}\,. \tag{3.3}$$

The solution to the second Riemann problem consists of a left-facing rarefaction fan, W_2^L, that is reflected back into the sample. The reflected fan lowers the pressure back down to atmospheric. This fan will appear in all the cases we consider and will play an important role in section 4.3. Because of its prominence in the sections that follow we will name it as: the *reflected rarefaction fan*. We see the free surface is represented in this Riemann problem as a contact discontinuity.

Regime B: Regime B is different from regimes A and C in that depending on the

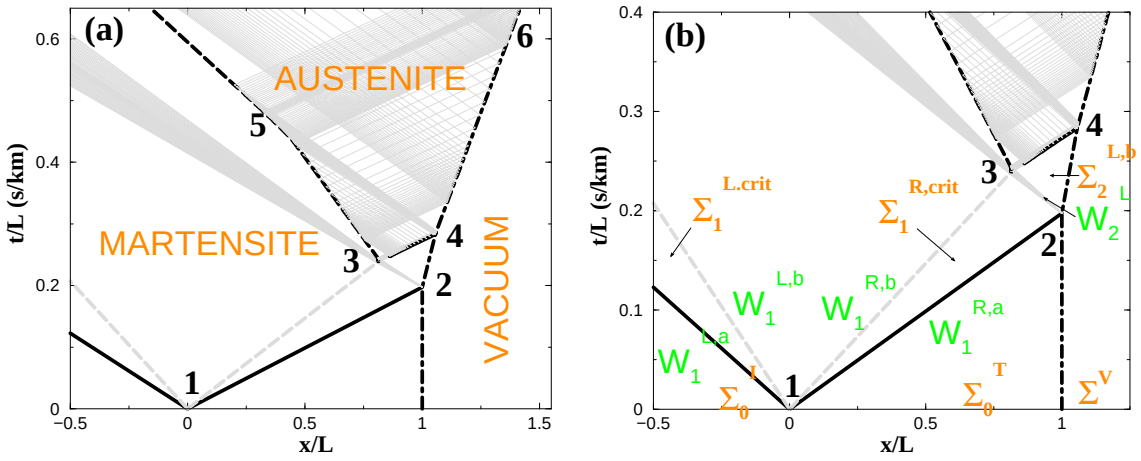

Figure 3-3: (x,t)-diagrams for the α-ϵ iron phase transformation. (a) An impact in sub-regime B.1. (b) An enlargement of region (a) showing details of the interaction regions $1\ldots4$.

magnitude of the impact velocity u_f, three different sub-regimes may occur. These three sub-regimes differ qualitatively in the way that the forward phase transformation wave "decays" into a backwards phase transformation wave. We will call these sub-regimes B.1, B.2, and B.3 and discuss their properties here.

In figures presented in this subsection we have labeled with numbers, the locations the sequence of wave interactions that take place as the flow evolves. We mention that in the rarefaction discontinuity approximation each interaction would occur at a point as all the waves colliding are discontinuities. When we consider the full equations and fully resolve rarefaction fans these point interactions "smear" and become interactions of simple waves and discontinuities. Typical (x,t)-diagrams associated with the first sub-regime B.1 are depicted in figure 3-3, those for a typical B.2 in figure 3-4 and those for typical B.3 in figure 3-5.

The plots for all three regimes give qualitatively identical results for the first two Riemann problems. The first Riemann problem, in contrast to regime A, produces two split waves W_1^R and W_1^L, (see figure 3-3 (a)). Each split wave consists of a precursor shock and a forward phase transformation front separated by a critical austenitic state. The middle state Σ^M is now martensitic.

As in regime A the next Riemann problem occurs when the precursor shock strikes the free surface. This Riemann problem, as in regime A, produces a left-facing rarefaction fan. The next wave interaction takes place when the head of the reflected fan meets the right-facing phase transition (labeled with a 3 in figure 3-3). The continuation of the flow for times beyond this point requires the numerical solution of the interaction of a rarefaction fan and a phase transformation wave. Qualitatively after this wave interaction has completed, the emerging picture is similar to what happens in the rarefaction discontinuity approximation [14] in that, three waves propagate away from the collision zone: a *left-facing expansive simple* wave, a middle wave (the type of which depends on the sub-regime), and a *right-facing compressive simple* wave.

We can see in all of the sub-regimes an effect of the phase transformation W_1^R is to "reflect" the reflected rarefaction fan born at the second Riemann problem back

towards the free surface. This reflection takes place at the interaction numbered 3 in all of the regime B sub-regime's. This reflected wave eventually reaches the free surface affects the free surface velocity. This is the mathematical origin for the second jump seen in the free surface plots.

For a complete discussion of the interaction that takes place when a phase transformations and a simple waves collide (see subsection 3.2.2).

- **Regime B.1:** In this sub-regime, after the compressive austenite-to-martensite

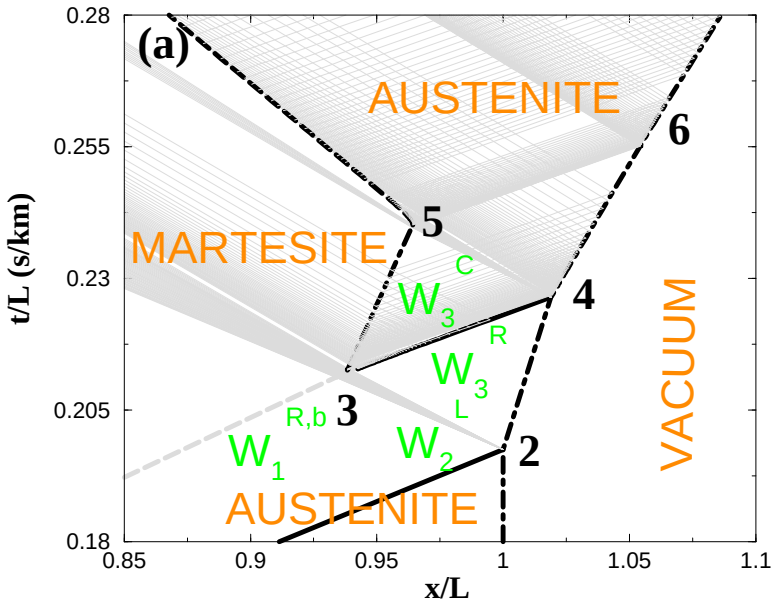

Figure 3-4: An impact in sub-regime B.2. (x,t)-diagrams for the α-ϵ iron phase transition.

transformation front meets the reflected rarefaction wave a "reverse-transformation tendency" prevails: the right-facing transition front is sufficiently weak for the reverse transformation — from martensite to austenite — to be initiated in the interaction of the rarefaction fan and the phase transformation wave. We see that in this sub-regime the third wave interaction produces a left-facing simple wave for the left wave, a *backwards phase transformation* wave as a middle wave, and a right-facing simple wave as the right wave.

- **Regime B.2:** In this sub-regime, after the compressive austenite-to-martensite

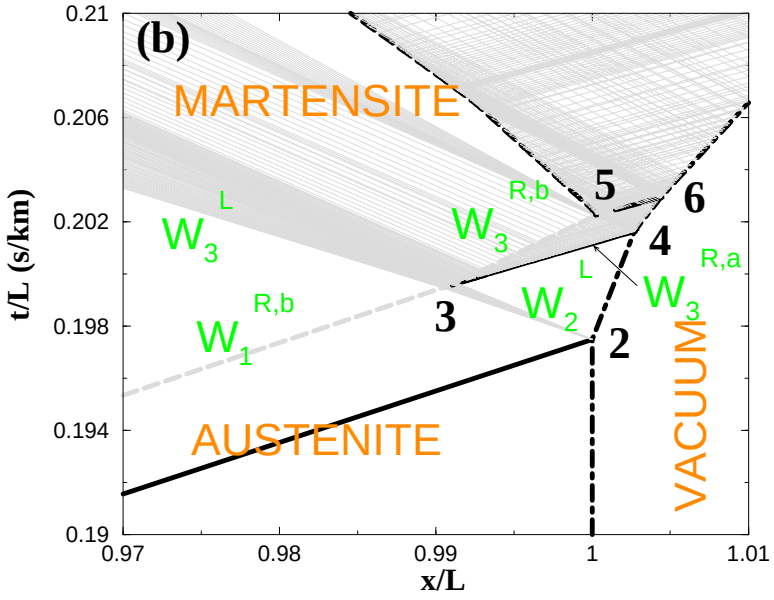

Figure 3-5: An impact in sub-regime B.3. (x,t)-diagrams for the α-ϵ iron phase transition.

transformation front meets the reflected rarefaction wave the "direct" and "reverse" transformation tendencies balance each other. The right-facing transformation front is not sufficiently weak for the reverse transformation to occur as it does in regime B.1. We see that in this sub-regime the third wave interaction produces a left-facing simple wave for the left wave, a *contact discontinuity* as a middle wave, and a right-facing simple wave as the right wave. The contact discontinuity travels until it is further weakened by the simple wave arising from the interaction labeled 4 and becomes a backwards transformation front at location 5.

- **Regime B.3:** In this sub-regime, after the compressive austenite-to-martensite transformation front meets the reflected rarefaction wave a "direct-transformation tendency" prevails. The right-facing transformation front is sufficiently strong to sustain the interaction of the rarefaction fan beyond the collision point. We see that in this sub-regime the third wave interaction produces a left-facing simple wave for the left wave, a *right-facing phase transformation* as a middle wave, and a right-facing simple wave as the right wave. We note that the right-

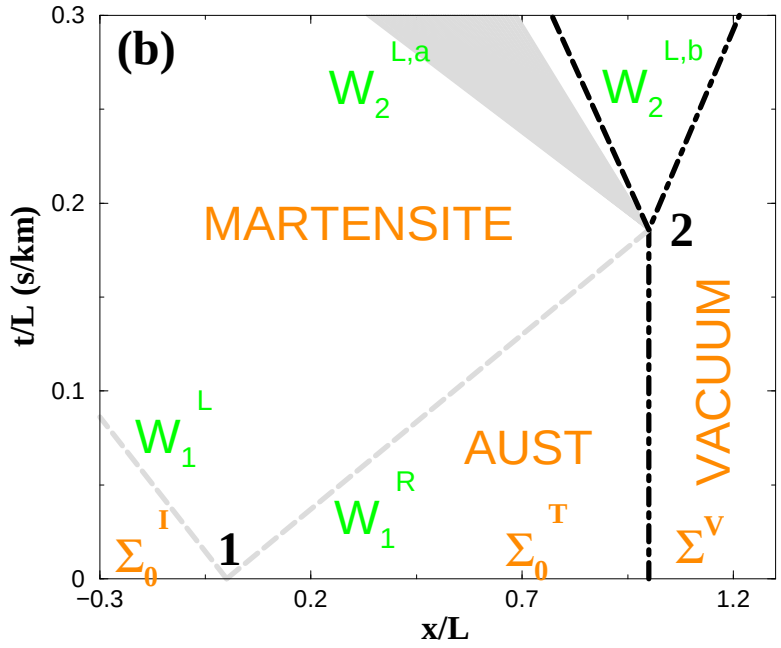

Figure 3-6: An impact in regime C. (x,t)-diagrams for α-ϵ phase transition in iron.

facing simple wave compresses the iron to its critical pressure so that the critical condition is maintained ahead of the forward phase transformation wave.

Regime C: In this case the impact is strong enough to create a single forward transformation front propagating into the target and flyer after impact. The middle state in this case is martensite. A typical (x,t)-diagram is depicted in figure 3-6.

The second Riemann problem arises as the right-facing forward transformation front W_1^R reaches the free-surface. We point out that in its solution the left-facing wave W_2^L is a *rarefying split-wave* — composed of a precursor rarefaction wave followed by a transformation front, changing the phase of the sample from martensite back to austenite.

Notice that, up to this point, we have not included a proper description of how the forward transformation front becomes a backwards transformation front under the influence of a simple wave. This is an important point and we present a discussion in the next subsection.

3.2.2 Simple Wave-Transformation Front Interactions

In this section we describe the sequence of events that take place when a forward transformation front decays into a backwards transformation front under the influence of rarefying simple wave. This decay only takes place when the initial Riemann problem produces split waves; a precursor shock followed by a forward phase transformation wave, as in regime B (see subsection 3.2.1).

In this regime, the first Riemann problem gives rise to a phase transformation wave traveling behind a precursor shock. The precursor raises the pressure from atmospheric to the critical pressure of austenite. This shock strikes the free surface and a left-facing rarefaction fan is reflected back into the sample (for an (x, t)-plot of these events, see figure 3-3 (a)). When the right-facing forward phase transformation wave and the left-facing rarefaction fan collide, what happens can be described by a sequence of two events: that of changing the forward transformation front into a contact discontinuity, followed by the further change of the contact discontinuity into a backwards transformation front. These two events will now be discussed.

Changes in Wave Type

The initial forward right-facing phase transformation wave can be conveniently visualized in the (v, p)-plane. In figure 3-7, the initial phase transformation wave which takes austenite at its critical forward transformation pressure to martensite at a higher pressure is represented by the chord in the (v, p)-plane from the critical pressure of austenite to the point A in the martensitic branch (see figure 3-7). In the (v, p)-plane this cord is the Rayleigh line. As the interaction with the rarefaction fan proceeds the pressure behind the phase transformation decreases and the initial point on the martensitic branch (point A) moves downward towards location D. Several intermediate chords, representing forward phase transformations between the critical austenite and martensite with pressures below p_A are shown. For example see points B and C in figure 3-7.

When the pressure behind the forward transformation front reaches that of the

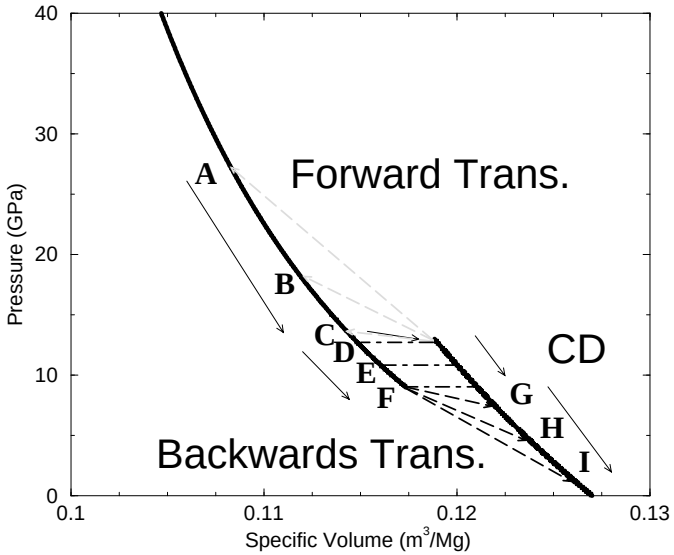

Figure 3-7: Representation in the (v, p)-plane of the forward transformation front decaying into a backwards transformation front. The arrows on the chords point to the state behind the phase transformation. The smaller arrows show the direction of the progression of pressure behind the phase transformation.

critical pressure in austenite (point D) the wave can no longer support a phase change and must change type. The forward transformation front now becomes a contact discontinuity. As the pressure drops still further the horizontal line, beginning at point D, translates horizontally downward eventually reaching the backwards transformation pressure for martensite (point F).

When this point is reached, further decrease in pressure requires another change in wave type. The contact discontinuity becomes a backwards transformation front. The corresponding picture in the (v, p)-plane of this backwards transformation front is of a Rayleigh line from the critical pressure of martensite (point F) to the austenitic wave curve branch (point G).

Figure 3-8 shows a detailed view in the (x, t)-plane of the interaction discussed above, for an impact falling in regime B.1. In this figure the locations where the contact discontinuity and the backwards transformation front form are shown as locations P_1 and P_2 respectively. Also present are the simple waves that are reflected and transmitted as this interaction takes place. These reflected and transmitted simple waves will be discussed next.

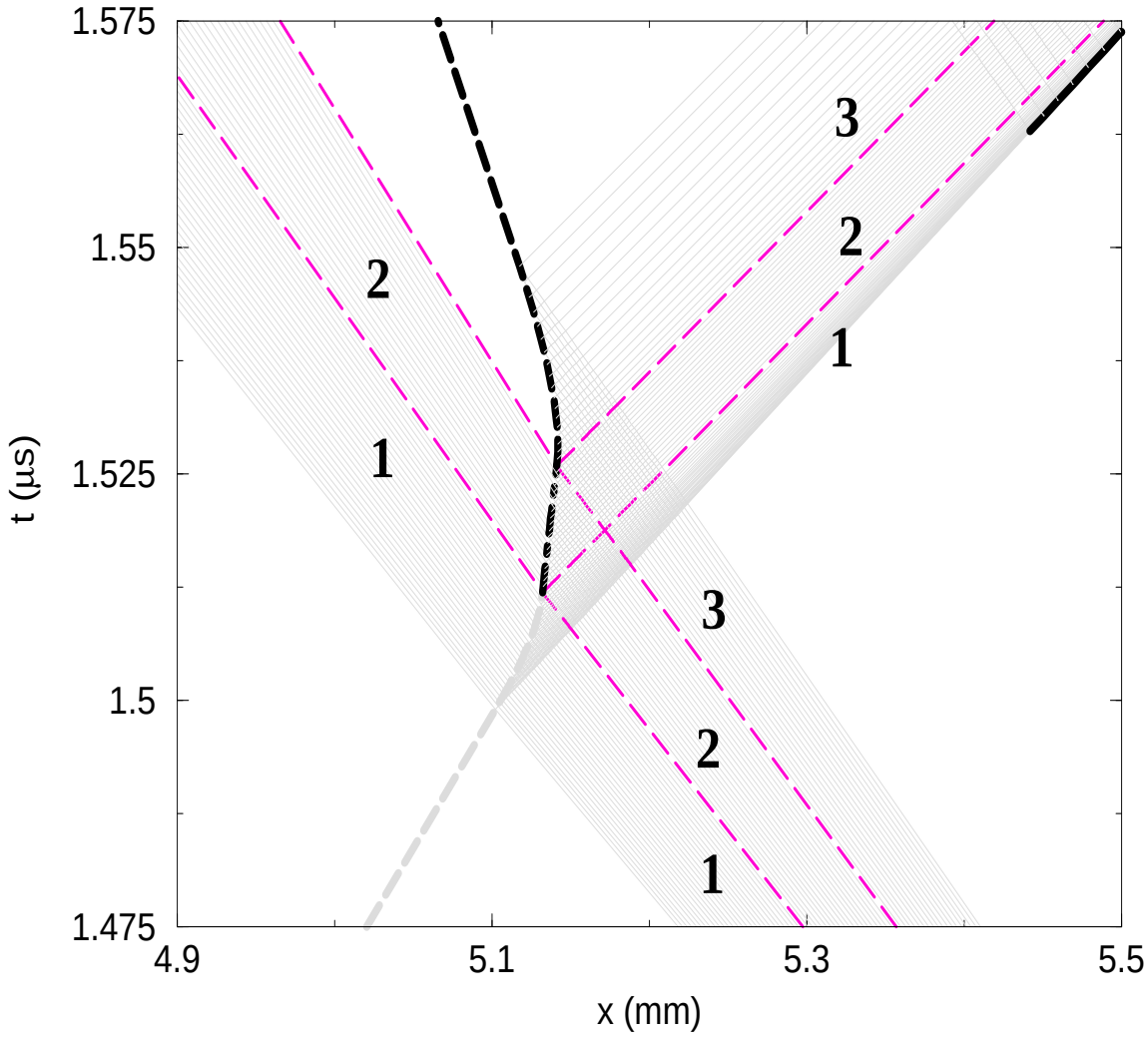

Figure 3-8: Detailed view in the (x, t)-plane of the interaction of a right-facing forward transformation front with a left-facing rarefaction fan. Please see the key presented on page 48 for a description of the symbols used. We have drawn the boundaries of the simple waves with a long dashed line.

Reflected and Transmitted Composite Simple Waves

Here we discuss the nature of the reflected and transmitted simple waves that are produced in the interaction of a phase transformation wave and a rarefaction fan.

As the right-facing forward phase transformation wave propagates through the left-facing reflected rarefaction fan, the pressure ahead of the phase transformation wave must remain at the critical pressure of austenite. To insure this a right-facing simple compression wave is reflected from the forward transformation front and an an expansive simple wave passes through phase transformation (see wavelet A and wavelet A' in figure 3-8).

At the point where the forward phase transformation front changes into a contact discontinuity. From standard theory for contact discontinuity and rarefaction fan interactions [18, p. 180] one sees that both the reflected and transmitted wavelets in this case are expansive (see wavelet B and wavelet B' in figure 3-8).

At point F where the contact discontinuity changes into a left-facing backwards transformation front, the pressure ahead of the wave is held a critical. It can be shown that this is sufficient to ensure that no transmitted wave is propagated through the backwards phase transformation. Thus in the (x, t)-plane characteristic impinge on the back of the backwards phase transformation but no characteristic are drawn crossing this wave indicating that the state ahead of this wave is constant. We mention that the reflected wave from the back of the backwards phase transformation is a compressive simple wave.

From this discussion we see here the first example of a simple wave of mixed type. The reflected simple wave from the forward transformation front is compressive, the reflected simple wave from the contact discontinuity is expansive, and the reflected simple wave from the backwards transformation wave is compressive again. This gives a structure of compressive, expansive, compressive to the entire reflected simple wave. In the numerics presented in chapter 5, the boundaries between these simple wave are easily shown in the (x, t)-plane or by a picture of the pressure profile. In figure 3-9 one sees clearly the three components of the composite simple wave propagating towards

the free surface on this plot of pressure as a function of x at a given time. There the leading compressive simple wave is steepest, the expansive portion is shallower, and the trailing compressive simple wave is shown last.

From this picture we can observe another phenomena. If any of the compressive simple waves break before reaching the free surface we must insert a shock propagating with a speed given by the Rankine-Hugoniot equations. In the (x, t)-plane shown in figure 3-8 we can see that it is the first compressive portion of this composite simple wave that breaks. The numerics then inserts a shock (drawn as a dark black line) propagating to the right.

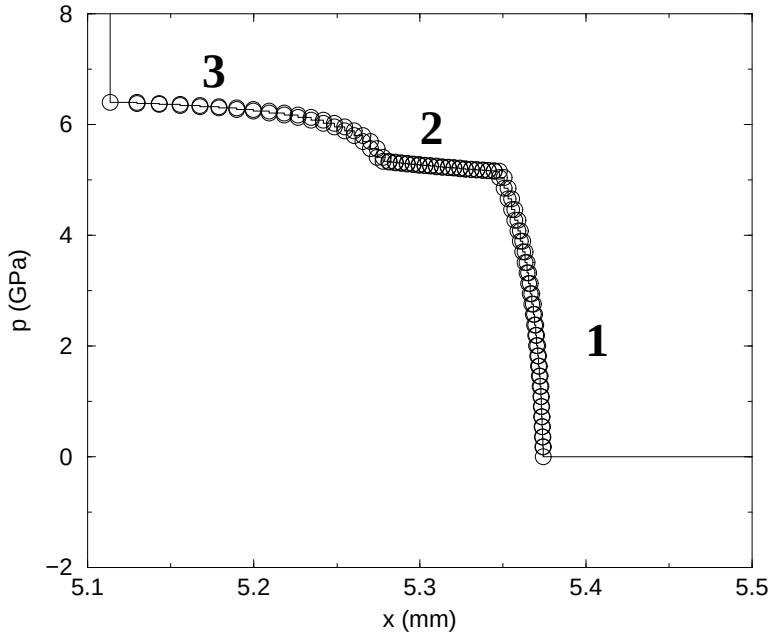

Figure 3-9: Profile of the composite simple wave of pressure propagating to the right towards the free surface.

Remark 4 *This explanation hints at other effects that do not happen in this physical system, but could happen mathematically with the hyperbolic system given here. The natural reverse of the process just described would correspond to a backwards transformation front interact with a sufficiently strong compressive simple wave, producing a forward transformation as a result. We mention also that if a contact discontinuity separating two different phases of the same material interacts with a sufficiently strong expansive or compressive simple wave transformation among phases could result. As*

a practical note, in the numerics for this problem all waves that could change type are carefully monitored at each timestep to insure that the correct representation is being used.

3.2.3 Conclusions

With the full numerical solution to the flow equations, comparisons can now be made between the free surface plots predicted by the full Bruno-Vaynblat theory and the experiments of Barker and Hollenbach. Remembering that the BV theory has *no* free parameters the a comparison of these plots will show the extend that the BV theory fully captures the physics of these phase transformation. Plots of this comparison are shown in figure 3-10.

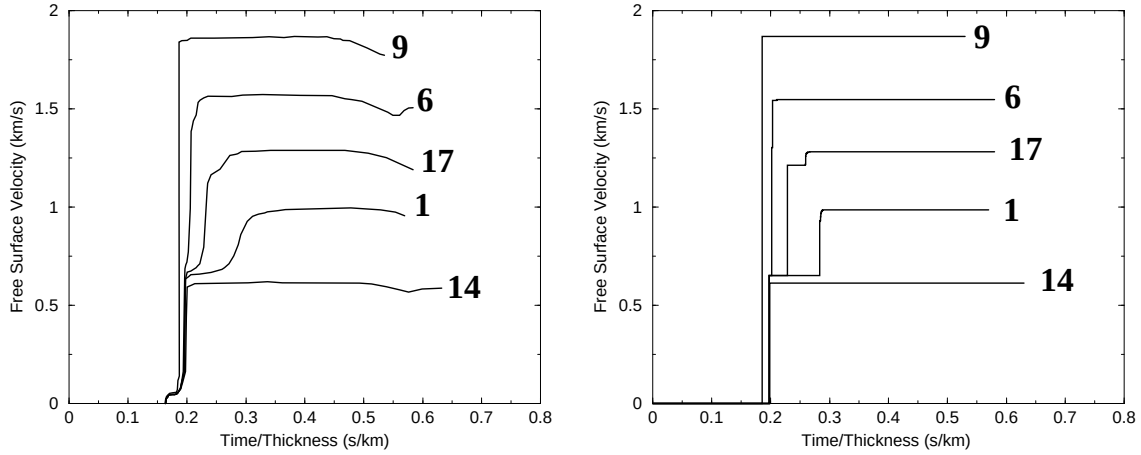

Figure 3-10: Free surface profiles for α-ϵ phase transition in iron. On the left are the experimental curves. On the right calculated curves using the characteristic tracking method, including rarefaction fans.

We notice that although the curves have improved some, with respect to the points mentioned in section 3.1, the compressive nature of the first component of the simple wave that is reflected from the forward transformation front is so great that it breaks and becomes a shock on its way to the free surface. Thus the free surface velocity profile resembles the one seen under the rarefaction discontinuity approximation. From this exercise we have learned a very important fact: in order to improve the agreement with experiment we must somehow smooth these shocks.

The manner in which this is accomplished is described in the following section.

3.3 Additional Physical Effects

The results and dynamics of including rarefaction fans into the numerics are presented in section 3.2. The inclusion of rarefaction fans into the Bruno-Vaynblat model gave somewhat smoother free surface profiles. We learn that the compressive nature of the *first* component of the reflected composite simple wave results in the formation of a shock and in order to further improve the theory, additional smoothing of this piece is needed. Three physical effects currently neglected and that would smooth this compressive simple wave are considered.

1. Dissipation is important. Generically there is always dissipation, and this energy loss needs to be included in the model. Incorrectly modeling phase transformations as energy conserving, by not including dissipation, could result in pictures of qualitatively the same type as presented in figure 3-10. This investigation is reported on in chapter 4 section 4.1.

2. The equation of state of austenite, while well known for pressures far from critical, cannot be claimed to be known accurately for pressures near or close to critical. We exploit this fact by modifying the austenitic equation of state near the critical transformation pressure for austenite. This modification while more indirect than other methods can lead to smoother free surface profiles. This investigation is reported on in chapter 4 section 4.3.

3. As discussed in section 1.3, an alternate approach to the theory of austenitic-martensitic phase transitions is based on the idea of a relaxation time. These effects have been incorporated in past models, see for instance [8, 72]. In some cases it is found that, to achieve good agreement with experiment, a different relaxation time is required for each experimental curve, which is not a very satisfactory situation [8]. Since several previous theoretical studies have investigated this effect, we focused the efforts of this work on the previous two ideas.

The next chapter is concerned with the implementations of several of the ideas discussed here. We begin by considering the effect dissipation has on the full Bruno-Vaynblat model and then look at modifications to the austenitic equation of state.

Chapter 4

Model Modifications

In chapter 3 we studied the effects of including rarefaction fans in the Bruno-Vaynblat model, using a Mie-Grüneisen equation of state. The agreement with experiments, due to this more accurate implementation of the model, improved (relative to the approximate implementation by Bruno and Vaynblat). However, some disagreements persisted; significantly the fact that several of the wave signatures at the free surface (as observed in the experiments) are "smoother" than those produced by the model. Several physical effects, neglected in the Bruno-Vaynblat model, were proposed in section 3.3 as possible causes for the discrepancies. With the hope of further improving the agreement between the experiments and the theory, in this chapter we consider two of these physical effects: first we modify the model so as to include them, and then we study the consequences of this (the modified models are solved numerically, and the results are compared with the experiments). In the first modification, considered in sections 4.1 and 4.2, we introduce dissipation into the model. In the second modification, studied in section 4.3, we consider the effect of local changes in the equation of state for the Austenite, affecting the behavior of the material close to the phase transition regime only.

4.1 Dissipative Effects

In this section we will study the importance and effects of dissipation in the shock induced phase transitions under consideration. First we will give arguments indicating why dissipation may be important, then we will modify the model equations to include dissipation in as simple a way as possible, next we will introduce a numerical scheme to solve the modified equations, and finally we will analyze the results from this modification.

4.1.1 Motivation

In this subsection we give some arguments indicating that the amount of dissipation, in the regime of the shock induced phase transitions we consider, may be quite large — so that it should not be neglected. These arguments will be used as a motivation for including dissipation into the governing equations in (2.2), followed by an investigation of the effect this has on the predictions of the model.

We begin by pointing out that, after each flyer-plate experiment is finished, the target material is completely destroyed. Therefore, measurements can only be taken of the free surface for a very short time (while the target is still in one piece). Furthermore: a full explanation of what happens internally in the target (causing its destruction) is not known.

For parameter regime B impacts (see subsection 3.2.1), a possible explanation (for the destruction of the sample) is the following: When the precursor shock propagates through the target, it raises the sample pressure/stress from atmospheric to critical. Thus, a region of critical austenite forms between the precursor shock and the phase transition front (traveling behind the shock, at a slower velocity). One may ask then: what keeps the austenite in the critical region from changing phase right after the shock passes, and forces it to wait till the phase transition front arrives? The explanation for this is, roughly, as follows: In iron the martensite phase has a volume contraction of about 20%, relative to the volume of the austenite phase. Such contraction cannot happen at some arbitrary place inside the material, for the volume

reduction would immediately make the pressure drop below critical (stopping the phase change). Thus, the austenite must wait till the phase transition front (which, effectively, carries the volume reduction needed for the transformation) arrives, before it can change into martensite.

There is, however, a catch to the explanation at the end of the last paragraph. Namely: it only makes sense for an ideal material, with no defects of any kind. The reason is that defects allow the contraction needed to happen, at the price of a fracture in the target material. Further, any such fracture will (generally) allow more fractures to happen, the net consequence of this being that very many fractures will develop in the target (in the region between the precursor shock and the transition front), with some amount of phase transition occurring before the arrival of the main phase transformation front. These fractures are then the cause of the sample destruction.

Modeling at the "continuum" level of the process described in the prior paragraph is very hard, and beyond our current level of understanding — in fact, trying to avoid such modeling was one of the main motivations Bruno and Vaynblat had when they developed their model. We will not attempt to do this here, but we observe that one important consequence of this process is that we can expect a large amount of dissipation to occur because of it: From the view point of the transformation wave, the cracked material it travels through is extremely dissipative. Thus we propose to include dissipation into the model, and do so in as simple a way as possible. Namely: we will take an approach similar to the one that is used in the modeling of dissipation by turbulent fluid flows, and add an "effective" viscosity to the governing equations — note that this viscosity is not molecular viscosity, which is usually quite small, in fact, we expect it to be large. This "viscosity" will, unfortunately, be a free parameter (which we do not know how to measure independently). Actually, in agreement with the motivation for this dissipative model, we will introduce two viscosities, namely: one value will apply ahead of the precursor shock, and a second (much larger one) behind it.

We note that this work here is the first to incorporate the idea of an effective viscosity within the context of phase transformations. It is the very fact that the

Bruno–Vaynblat model excludes mixture regions that allows us to treat both the effects of viscosity and phase transformation within the context of the same model. Previous authors have used the idea of an effective viscosity to study the dislocation density in a material [40], and (from this point of view) our viscosity approach can be stated as postulating an increase in the dislocation density as the result of the precursor shock raising the pressure to critical.

Finally, we point out that, in addition to the dissipation we expect due to the process described above, there are other sources that may also be important, such as (for example) the losses introduced during the movement of crystalline grain boundaries. We also notice that the main effect of introducing dissipation into a hyperbolic system is the "smearing" of the shocks, and the widening of the rarefaction fans (see reference [75]). This, clearly, will tend to make the theoretical free surface plots more like the experimental ones. An important point to be made here, however, is that *dissipation should not affect the thickness of the main transformation front itself.* Thus, in our modified model the shocks will no longer be modeled as discontinuities, but the transformation fronts will still be discontinuous — see figure 4-1.

4.1.2 Dissipative Governing Equations

We modify the Eulerian equations (2.1), to include dissipation, as follows:

$$\frac{\partial}{\partial t}\rho + \frac{\partial}{\partial x}(\rho\, u) = 0\,, \qquad \frac{\partial}{\partial t}(\rho\, u) + \frac{\partial}{\partial x}(\rho\, u^2 + p) = \mu\, \frac{\partial^2}{\partial x^2} u\,, \tag{4.1}$$

where the viscosity coefficient μ is a measure of the amount of dissipation present in the system. Equivalently, the Lagrangian equations (2.2) become

$$\frac{\partial}{\partial t}\mathrm{v} - \frac{\partial}{\partial \xi}\mathrm{u} = 0\,, \qquad \frac{\partial}{\partial \mathrm{t}}\mathrm{u} + \frac{\partial}{\partial \xi}\mathrm{p} = \mu\, \frac{\partial}{\partial \xi}\left(\frac{1}{\mathrm{v}}\frac{\partial \mathrm{u}}{\partial \xi}\right)\,. \tag{4.2}$$

To study the effect that the added viscous term has on the free surface plots, we solved numerically the Lagrangian equations in (4.2). In what follows we will first present a brief discussion of the numerical algorithm used in solving these equations,

followed by a presentation of some selected results from the numerical calculations, and finally comment on the results obtained.

We note that these equations are more complicated than they appear upon a cursory examination. The problem appears because of the phase transitions, across which the equation of state (relating the pressure p to the density ρ) has a discontinuity. This introduces discontinuities in the flow variables, which makes the meaning of the twice-differentiated dissipative term not clear at the location of the phase transitions. We will deal with this difficulty in what follows, within the context of the numerical algorithm.

4.2 Dissipative Numerics

In this section we describe the motivation and discretizations used in the numerical algorithm chosen for this problem. In section 3.3 of chapter 3, we discussed several qualitative differences between the free surface velocity plots generated using the Bruno–Vaynblat model and the experimental measurements of Barker and Hollenbach. Of the differences noted, the most important disagreement was in the slope (or width) of the second wave. All the theoretical free surface predictions (thus far) have slopes that are almost vertical, while the experimental curves are much smoother. The greatest disagreement in regards to this effect, occurs with the first experiment presented in Barker and Hollenbach [5]. This experiment corresponds to a parameter regime B impact (see subsection 3.2.1). Thus, the numerical scheme is implemented with the aim of solving the equations in (4.2) for regime B impacts.

For regime B impacts, the first Riemann problem (between the flyer and the target) produces two right-facing waves: a precursor shock and a phase transformation, see figure 3-3. A hypothetical representation of the solution at a time after impact, but before the precursor shock has collided with the free surface, is shown in figure 4-1. There one can see the precursor shock broadened by the dissipation: the shock is now a compression wave where the competing effects of nonlinearity and diffusion balance each other. It is clear from this figure that the phase transformation front

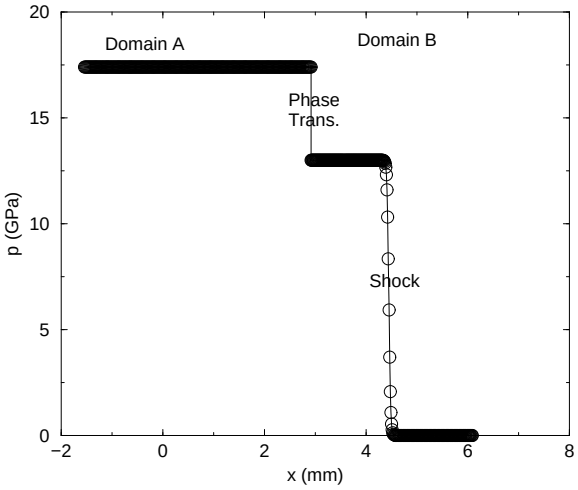

Figure 4-1: Hypothetical diffusive pressure wave profile, for an impact in the parameter regime B, plotted at a time shortly after the impact. The horizontal axis is distance, in millimeters, measured from the point of impact. The vertical axis is pressure, in Giga Pascals. Domain A (respectively B) is defined as all the points to the left (respectively, to the right) of the phase transformation. Here we see the right-facing phase transformation, present as a discontinuity, and the right-facing shock, slightly smeared by the viscosity, both propagating towards the free surface — located at $x \approx 6\,mm$.

divides the material into *two domains of interest: domain A* (containing martensite, behind the transformation front) and *domain B* (containing austenite, ahead of the transformation front).

The natural division of the flow into separate domains, by a moving phase transformation discontinuity, is what motivates the transformation given below — in which we consider a general case, with more than one discontinuity and more than two domains. Specifically, we derive discrete numerical equations for M domains, separated by $M+1$ interfaces — including the left end of the first domain, and the right end of the last domain (that is: the left and the right ends of the sample, respectively). *In each domain there is a single phase, either austenite or martensite, so that a single equation of state applies.* Thus, in each domain the equations in (4.2) have a clear meaning, and standard finite difference discretizations can be used. The problem is then reduced to the question of how to solve the equations across the phase transition fronts, where the equation of state has a discontinuous jump, and the meaning of the equations in (4.2) has to be clarified.

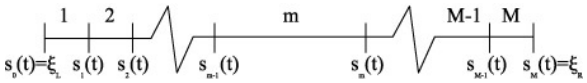

Figure 4-2: Several domains separated by moving discontinuities, including the left end of the first domain and the right end of the last domain — that is: the left and the right sample ends, respectively. Each discontinuity is a phase transition, and in each domain there is a constant phase, either austenite or martensite.

Consider a section of the real line from ξ_L to ξ_R, containing $M+1$ interfaces and M domains, as in figure 4-2. Assume that, as a function of time t, the locations of the interfaces are given by the smooth functions $\xi = s_i(t)$, where $0 \le i \le M$, $\xi_L = s_0(t)$ corresponds to the left end of the sample, and $\xi_R = s_M(t)$ corresponds to the right end. Notice that we work in Lagrangian coordinates, where the function $\xi = s_i(t)$ indicates the mass to the left of the given interface (up to some constant, generally selected so that $\xi_L = 0$), and $\mathcal{M}_i = \dot{s}_i(t)$ is the mass flux across the interface. A similar formulation is possible in Eulerian coordinates, where the values $s_i(t)$ and $\dot{s}_i(t)$ give the location in space and velocity of the i-th interface.

In any given domain ($s_{m-1}(t) \le \xi \le s_m(t)$), define the coordinate transformation $\xi \to \xi_m$ by

$$\xi_m = \frac{\xi - s_{m-1}(t)}{s_m(t) - s_{m-1}(t)}\,, \qquad \text{so that} \qquad \begin{cases} \xi = s_{m-1} & \Longleftrightarrow \quad \xi_m = 0\,. \\ \xi = s_m & \Longleftrightarrow \quad \xi_m = 1\,. \end{cases} \tag{4.3}$$

Thus the m-th domain is transformed into the fixed interval $[0,1]$ — this is a mathematical trick often used in free surface calculations [35]. Of course, the functions $s_i(t)$ are not known beforehand, so that the price we pay for simplifying the domain of integration (eliminating the free surfaces) is to introduce a new unknown for each domain — namely: the functions $s_m(t)$, $1 \le m \le M$.

In each domain, we can now write the equations in (4.2) in terms of the local variable ξ_m, using equation (4.3) above. Conservation of mass, the first equation in (4.2), becomes

$$\frac{\partial}{\partial t}\mathrm{v} - \frac{1}{\mathrm{s_m} - \mathrm{s_{m-1}}} \left[\left((1-\xi)\,\dot{\mathrm{s}}_{\mathrm{m-1}} + \xi\,\dot{\mathrm{s}}_{\mathrm{m}} \right) \frac{\partial}{\partial \xi}\mathrm{v} + \frac{\partial}{\partial \xi}\mathrm{u} \right] = 0\,, \tag{4.4}$$

and conservation of momentum, the second equation in (4.2), becomes

$$\frac{\partial}{\partial t}u - \frac{(1-\xi)\,\dot{s}_{m-1} + \xi\,\dot{s}_m}{s_m - s_{m-1}}\,\frac{\partial}{\partial \xi}u + \frac{1}{s_m - s_{m-1}}\,\frac{\partial}{\partial \xi}p = \frac{\mu}{(s_m - s_{m-1})^2}\,\frac{\partial}{\partial \xi}\left(\frac{1}{\mathrm{v}}\frac{\partial u}{\partial \xi}\right)\,, \quad (4.5)$$

where, to simplify the notation, we have dropped the subscript m on ξ_m. Next we discretize these equations, using a finite differences staggered grid approach.

Break up each domain $0 \le \xi \le 1$ into a uniform grid, with N nodes, including the end points. Namely, let

$$\xi_i = (i-1)\,\Delta\xi\,, \qquad \text{where} \quad \Delta\xi = \frac{1}{N-1} \quad \text{and} \quad 1 \le i \le N\,, \qquad (4.6)$$

be the *nodes*, and call the interval $\xi_i \le \xi \le \xi_{i+1}$ the *i-th cell* — with *center:* $\xi_{i+\frac{1}{2}} = \frac{1}{2}\,(\xi_i + \xi_{i+1})$. Then, for the specific volume v (and density $\rho = 1/\mathrm{v}$) we use a node centered approach, with the numerical scheme carrying the values of the density at the nodes — i.e., the values: $\mathrm{v}(\xi_\mathrm{i}, \mathrm{t})$. For the velocity, on the other hand, we use a cell centered approach, with the numerical scheme carrying the values of the velocity at the cell centers — i.e., the values: $u(\xi_{i+\frac{1}{2}}, t)$. It is now convenient to introduce *notation to denote whether a numerical variable is defined on nodes or cells.* To be specific, when referring to a cell centered variable, for example u, we will use a bar, as in $\bar{u}$. On the other hand, a node centered variable will receive no special indication. Thus the notation v_ξ applies to the node centered value of the ξ derivative of the specific volume, while $\bar{\mathrm{v}}_\xi$ means the cell centered value of the same thing. With these definitions we are now in a position to write down the spatial discretization of the dissipative equations in (4.4) and (4.5) are, using the staggered grid technique, as done in the subsections that follow.

We point out that the *full* discretization of the equations in (4.4) and (4.5) will be done using the *method of lines.* In this method one first discretizes the spatial derivatives, forming a semi-discrete system of equations, and then uses an ordinary differential equation solver to discretize the time derivatives. Following this approach, in the presentation below we first focus on obtaining semi-discrete approximations to the governing partial differential equations, and afterwards deal with the discretiza-

tion of the time derivatives, so as to obtain a fully discrete set of equations.

4.2.1 Method of Lines Applied to the Dissipative Problem

Since the method of lines applied to the equation in (4.4), representing conservation of mass, involves updating a node centered variable, v, we need discrete versions for the spatial derivatives in the equation, centered at the nodes. Thus we use centered differences to approximate the spatial derivatives appearing in equation (4.4), namely:

$$\frac{\partial}{\partial\xi}\mathrm{v}(\xi_{\mathrm{i}},\mathrm{t}) \approx \frac{\mathrm{v}(\xi_{\mathrm{i+1}},\mathrm{t}) - \mathrm{v}(\xi_{\mathrm{i-1}},\mathrm{t})}{2\Delta\xi} \qquad \text{and} \qquad \frac{\partial}{\partial\xi}\mathrm{u}(\xi_{\mathrm{i}},\mathrm{t}) \approx \frac{\bar{\mathrm{u}}(\xi_{\mathrm{i+}\frac{1}{2}},\mathrm{t}) - \bar{\mathrm{u}}(\xi_{\mathrm{i-}\frac{1}{2}},\mathrm{t})}{\Delta\xi}\,, \tag{4.7}$$

where we note that both expressions on the right hand side involve the natural domain of definition of the variables involved (node centered densities and cell centered velocities). These approximations, when used in (4.4), lead to the following semi-discrete system (correct up to second order in $\Delta\xi$) for the conservation of mass

$$\begin{aligned}\frac{\partial}{\partial t}\mathrm{v}(\xi_{\mathrm{i}},\mathrm{t}) &= \left(\frac{(1-\xi_i)\,\dot{s}_{m-1} + \xi_i\,\dot{s}_m}{s_m - s_{m-1}}\right)\frac{\mathrm{v}(\xi_{\mathrm{i+1}},\mathrm{t}) - \mathrm{v}(\xi_{\mathrm{i-1}},\mathrm{t})}{2\,\Delta\xi} \\ &+ \left(\frac{1}{s_m - s_{m-1}}\right)\frac{\bar{u}(\xi_{i+\frac{1}{2}},t) - \bar{u}(\xi_{i-\frac{1}{2}},t)}{\Delta\xi}\,. \end{aligned} \tag{4.8}$$

A similar process can be applied to the equation in (4.5), for the conservation of momentum. This requires updating (in time) the velocity, a cell centered variable, so that cell centered approximations for the various derivatives with respect to ξ involved are needed. The exact discretizations selected to do this are no more technically complicated than the ones used above in the conservation of mass equation, but contain more terms. Thus, to avoid displaying long formulas here, the semi-discrete equations for the conservation of momentum are shown in appendix C.

The discretizations above are, of course, valid only inside each domain — where the relationship between p and v, as given by the equation of state, is smooth. We need now to worry about what happens at the ends of each domain, where two type of situations may arise: either the end of the domain coincides with the end of the sample

(i.e.: s_i for $i = 0$ or $i = M$), or the end of the domain corresponds to the location of a phase transition (i.e.: s_i for $0 < i < M$). This leads to two types of boundary conditions, that must be imposed at the domain ends, which we call (respectively) *outer boundary conditions* and *inner boundary conditions.* We note that, in order *to consider the resolution of this problem, we can restrict the discussion to the simpler case* $M = 2$, when there are only two domains — such as in the example shown in figure 4-1 for a typical initial condition in the parameter regime B, where a single right-moving, discontinuous, phase transformation front separates the martensite on the left from the austenite on the right. In this case, as indicated in the figure caption, we will call the martensite domain the domain A, and the austenite domain the domain B — note that the precursor shock wave in the austenite is not a true discontinuity in the dissipative approximation, and it is not a domain boundary.

In the numerical calculations we are not interested in computing for times large enough that wave reflections from the back end of the impactor reach the free surface. In the particular case of two domains, such as the one in figure 4-1, this means that we can *assume that the left boundary of domain A is at negative infinity* — with the right boundary at the phase transformation, located at $s(t)$. On the other hand, domain B is bounded on its left by the phase transformation front, and on its right by the free surface, at ξ_R. Finally, we note that, as the flow evolves, the phase transformation wave will change type: from a right moving phase transformation front, to a contact discontinuity, to a left moving phase transformation front — see subsection 3.2.2. Thus the domain boundaries are not always phase transformation fronts, and can even switch from being one to being a contact discontinuities, or vice versa. *Generally, the domain boundaries are just discontinuities (or interfaces), separating the martensite phase on one side from the austenite phase on the other.*

Going back to the issue of the boundary conditions, we note that the discretizations for the conservation of mass and momentum equations in (4.8) and (C.3)), both require information about the specific volume and the velocity one node and one cell away from the cell or node on which the time derivative terms in the semi-discrete equation are centered. Thus these equations cannot be used sufficiently close to a

boundary. In the next subsection we discuss the additional equations used to solve for the nodes and cells near boundaries (the inner and outer boundary conditions mentioned earlier in this subsection).

4.2.2 Boundary Conditions

In this subsection we discuss the equations used to update the unknowns, for nodes and cells, near the numerical domain boundaries. Two different types of boundary conditions are discussed here. The first type, which we call the *outer boundary conditions*, apply at the ends of the computational domain, namely: at ξ_L and ξ_R. The second type, which we call the *inner boundary conditions*, are the conditions needed at the interfaces between the domains. The exact conditions used at any given interface depend on the type of discontinuity separating the domains, be it a forward transformation front, a contact discontinuity, or a backwards transformation front. Below we discuss these two types of boundary conditions, as used in the numerical simulations.

Outer Boundary Conditions

The stencils of the semi-discrete equations, in (4.8) and (C.3), require the specification of variables one node and one cell to either side of the node or the cell at the stencil center. As a consequence of this fact, two boundary conditions are required on each outer boundary. This is consistent with the increase in order of the model partial differential equations, due to the added dissipative term.

To model numerically the semi-infinite nature of domain A, we argue that: for a sufficiently large and negative value of ξ, the specific volume should be constant. Thus we set $\mathrm{v} = \mathrm{v_L}$ at $\xi = \xi_L$, where $\mathrm{v_L}$ is obtained from the solution of the first Riemann problem (the collision of the impactor and the flyer), a calculation that is done before the full viscous flow computation is started. This gives one of the two boundary conditions needed on the left end of the numerical domain.

Similarly, we argue that on the right end of domain B the specific volume should

also be a constant, i.e.: $\mathrm{v} = \mathrm{v_R}$ on ξ_R, where the constant is determined by the equation $p(\mathrm{v_R}) = 0$. This follows because the right boundary of domain B is a free surface, and cannot support any pressure.

Finally, to determine the second boundary condition required at each end, we use the conservation of mass equation in (4.2). From this equation it is clear that, if v is constant along a particle path $\xi =$ constant, it follows that

$$\frac{\partial}{\partial \xi} u = 0\,. \tag{4.9}$$

This gives a second boundary condition, applicable on any $\xi =$ constant boundary, where v is kept constant.

Inner Boundary Conditions

Here we will formulate the boundary conditions used at the interface between the two domains, A and B, across which there is a jump in the equation of state (martensite on one side and austenite on the other). First we will consider all the unknowns/variables (at or near the interface) that cannot be updated by either of the equations in (4.8) or (C.3), and then we will systematically provide the extra equations needed to update their values.

We begin by considering the immediate neighborhood of the interface, and the associated unknowns there. Figure 4-3 shows a schematic representation of the situation. In this figure the interface is denoted with a cross, the nodes with solid dots and the cell centers with open dots. There are, however, some *important clarifications that must must be made with regard with this figure:* in fact, the rightmost node of the left domain (node N in the figure), the leftmost node of the right domain (node 1 in the figure), and the interface are the same point in space, but we have represented them separately in the picture — because they play different roles in the numerical algorithm. Similarly, there is no cell N belonging to the left domain, nor is there a cell 0 belonging to the right domain, but (for numerical reasons, which will become clear in the development that follows below) these *ghost cells* have been introduced in the

figure. We note that, in space, the N-th (ghost) cell of the left domain is actually to the right of the interface — it represents a ghost extension of the state of the material phase on the left of the interface, to the right of the interface. Similarly, in space, the 0-th (ghost) cell of the right domain is actually to the left of the interface.

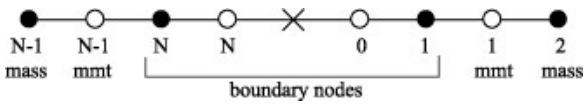

Figure 4-3: Schematic representation of the numerical grid near an interface. The interface is indicated by a cross, the nodes by solid dots and the cell centers by open dots. We note that, in fact, the rightmost node (i.e.: N) of the left domain, the leftmost node (i.e.: 1) of the right domain, and the interface are the same point in space, but (because they play different roles in the numerical algorithm) they are represented separately in the picture. Similarly, there is no cell N belonging to the left domain, nor is there a cell 0 belonging to the right domain, but (for reasons, explained in the text) these *ghost cells* are introduced by the numerical algorithm — they represent extensions of the material phases on each side of the interface, to the other side. In space, the N-th (ghost) cell of the left domain is actually to the right of the interface, and the 0-th (ghost) cell of the right domain is actually to the left of the interface.

The representation of the numerical grid shown in figure 4-3 provides a convenient way to label the unknowns around the interface. In this representation, each node and cell center carries one unknown (the values of the specific volume and velocity, respectively) and the interface carries two unknowns, namely: its Lagrangian coordinate position $\xi = s(t)$, and the mass flow across the interface $\mathcal{M} = \dot{s}$ — both as introduced by the transformation in (4.3), mapping the equations to a fixed $[0, 1]$ grid.

To update (in time) the specific volume in the node labeled $N - 1$, the formula in equation (4.8) can be used, since an additional cell and node exist to either side of this node. The same statement can be made about the cell center labeled $N - 1$, using the formula in equation (C.3). Similarly, the cell center labeled 1, and the node labeled 2, can be updated using the semi-discrete formulas in (4.8) and (C.3). This still leaves six variables for which the regular stencil used in the semi–discrete equations cannot be used, and for which extra equations are needed. These are:

$$\mathrm{v_N}\,, \quad \bar{\mathrm{u}}_\mathrm{N}\,, \quad \mathrm{s}\,, \quad \dot{\mathrm{s}}\,, \quad \bar{\mathrm{u}}_0\,, \quad \text{and} \quad \mathrm{v}_1\,.$$

The first extra equation is obtained by approximating the mass flux through the interface (i.e.: $\mathcal{M} = \dot{s}$) by the finite difference formula

$$\dot{s} \approx \frac{s^{n+1} - s^n}{\Delta t}\,, \tag{4.10}$$

where s^n is the value of $s = s(t)$ at time $t = t_n$, and $\Delta t = t_{n+1} - t_n$ (higher order approximations for the time derivative are also possible, of course, but this is the one that we used). The other five extra equations will depend on the type of interface between the two domains. They are presented in detail below in their continuous forms, and in their discretized forms in appendix D. In summary: two equations follow from the Rankine-Hugoniot jump conditions (conservation of mass and momentum across the interface), one equation from knowledge of the specific interface type, and the remaining two equations are obtained from a numerical extrapolation process to be described below. There are now two cases to consider, depending on the interface type.

Case 1: the interface is a forward or backwards transformation front.
Two of the equations follow from the conservation of mass and momentum across the interface, where care must be taken to include the fluxes due to the dissipative terms. Modifying the equations in (A.11) to include the fluxes due to dissipation, we get

$$\dot{s}\,[\mathrm{v}] + [\mathrm{u}] = 0 \qquad \text{and} \qquad \dot{s}\,[\mathrm{u}] - \left[\mathrm{p(v)} - \frac{\mu}{\mathrm{v}}\frac{\partial}{\partial \xi}\mathrm{u}\right] = 0\,, \tag{4.11}$$

where the partial derivative u_ξ must be computed without crossing the discontinuity — it is because of the need to compute this derivative that the ghost cells were introduced earlier. We note that, in order to derive these equations, we have assumed that *there is no viscous contribution to the momentum flux arising from the phase transformation.* Mathematically this means that singularities of order higher than Dirac deltas are ignored. These singularities arise from the dissipative term in (4.2), because the variables are discontinuous across the interface. After this is done, the second jump condition above in (4.11) guarantees the cancellation of the remaining

distribution (Dirac's deltas) part in the momentum equation in (4.2).

A further condition, that is specific to transformation fronts (forward and backwards), follows from the fact that the pressure ahead of the wave must be at the critical value for the phase that the wave is propagating into. This gives a third equation

$$p_N = p_{\text{crit}}^{\{A,M\}} \qquad \text{or} \qquad p_1 = p_{\text{crit}}^{\{A,M\}}\,, \tag{4.12}$$

where which formula is used depends on the direction of propagation of the interface, and the type of phase transformation.

Finally, the two remaining boundary conditions are obtained from a numerical approximation. As explained above, the ghost cells are introduced because of the need to compute the derivatives u_ξ in the right equation in (4.11). However, this is meaningless unless values for the velocities are provided at the ghost cell centers. A reasonable approach to doing this is to use extrapolation of the values of the velocity, from the side the ghost cell belongs to. We found, through experimentation with various possibilities, that first order extrapolation gives reasonable results for this purpose. This yields, on the uniform grids we used (see (4.6)), the following equations for $\bar{u}_N$ and $\bar{u}_0$

$$\bar{u}_0 = 2\,\bar{u}_1 + \bar{u}_2 \qquad \text{and} \qquad \bar{u}_N = 2\,\bar{u}_{N-1} + \bar{u}_{N-2}\,. \tag{4.13}$$

Case 2: the interface is a contact discontinuity.

In this case

$$\frac{ds}{dt} = 0\,, \tag{4.14}$$

because no mass crosses the interface. This gives a condition specific to contact discontinuities only. Conservation of mass and momentum now take the simpler forms

$$[u] = 0 \qquad \text{and} \qquad \left[p(\mathrm{v}) - \frac{\mu}{\mathrm{v}}\frac{\partial}{\partial\xi}\mathrm{u}\right] = 0\,, \tag{4.15}$$

where the same remarks made after the equations in (4.11) apply. Finally, two additional (numerical) boundary conditions are obtained by manipulation of the conser-

vation of mass differential equation in (4.4). This equation yields, when evaluated on the N-th node:

$$\frac{d}{dt}\mathrm{v_N} - \frac{1}{\mathrm{s} - \xi_\mathrm{L}} \frac{\partial}{\partial \xi}\mathrm{u_N} = 0\,,$$

where we have used the fact that we have only two domains, that the node is actually a particle path, and that $\dot{s} = 0$. A semi-discrete equation for $\mathrm{v_N}$ can now be obtained by discretizing the spatial derivative of the velocity in this equation, using finite differences. This gives

$$\frac{d}{dt}\mathrm{v_N} - \frac{1}{\mathrm{s} - \xi_\mathrm{L}} \frac{3\bar{\mathrm{u}}_\mathrm{N} - 4\bar{\mathrm{u}}_{\mathrm{N}-1} + \bar{\mathrm{u}}_{\mathrm{N}-2}}{2\Delta\xi} = 0\,, \tag{4.16}$$

where the velocity value at the center of the ghost cell (i.e.: $\bar{u}_N$) follows by the same extrapolation process used in earlier in equation (4.13). A similar procedure generates a semi-discrete equation for $\mathrm{v_1}$.

In appendix D we present a detailed summary of all the semi–discrete equations used to update each node, cell, and interface (i.e.: s) at the boundary between domains. The numerical scheme is completely defined once we specify how to discretize the time derivatives. This is explained in the next subsection.

4.2.3 Discretization of the Time Derivatives

In this subsection, following the method of lines approach, we finish the construction of the viscous numerical algorithm. We do so by presenting the strategy used to discretize the time derivatives in the in the semi–discrete equations derived in the earlier subsections. To this end we use the θ-method, which leads to some of the most commonly used (simple) algorithms for time integration.

The semi–discrete equations for the dissipative model can be written in the compact vector ode form

$$\frac{d}{dt}Y = f(Y)\,, \tag{4.17}$$

where $Y = Y(t)$ is a vector representing the solution to the problem, and f is the nonlinear vector function that follows upon writing the semi–discrete equations in

terms of Y. Specifically, we can write Y as a vector having one block of entries per domain, with the blocks separated by the variable giving the position of the corresponding interface s_n. Furthermore, within each block let the Y entries alternate between the node centered specific volume values $\mathrm{v_j}$ and the cell centered flow velocity values $\bar{u}_{j+\frac{1}{2}}$. Note that the values of u in the ghost cells are not included in Y, since they are not evolved in time, and are computed directly by the purely algebraic equations in (4.13).

Let now $0 \leq \theta \leq 1$ be a relaxation parameter, whose value can be used to control the accuracy and stability of the algorithm (see below). Introduce also a time discretization, with $t_{n+1} = t_n + \Delta t$ and $Y^n = Y(t_n)$. Then the θ-method algorithm for the ode in (4.17) is given by

$$F(\Delta Y^n, Y^n) = \Delta Y^n - \Delta t\, f\,(Y^n + \theta\, \Delta Y^n) = 0\,, \tag{4.18}$$

where $\Delta Y^n = Y^{n+1} - Y^n$, and F is defined by the formula. It is well known that: when $\theta \geq 1/2$ this algorithm is unconditionally stable, and when $\theta < 1/2$ the algorithm is conditionally stable only [59]. Particular values of θ give rise to some common time integration strategies:

- $\theta = 0$ gives the explicit forward Euler scheme.
- $\theta = \frac{1}{2}$ gives the second–order, centered implicit trapezoidal rule (or Crank-Nicholson).
- $\theta = 1$ leads to the backwards implicit Euler method.

In our calculations we used a value of θ slightly above $1/2$ (in fact $\theta = 0.55$), to assure maximum stability and accuracy.

Given the current state Y^n, equation (4.18) is a (generally nonlinear) system of equations for the increment vector ΔY^n, which we solve using Newton's method. This requires the calculation of the Jacobian of the nonlinear vector function F, which is a cumbersome but straightforward task — since, in fact, F is made up by fairly simple formulas.

We finally point out that, since the equations used at the interface change as the interface changes type, we monitor where this changes take place, and then adjust the formulas for the function F and its Jacobian accordingly.

4.2.4 Dissipative Numerical Results

From the analysis in subsection 4.1.1, it is clear that we should have (at least) three different effective viscosities: one (relatively low) in the austenite ahead of the precursor shock, another (high) one in the critical austenite behind the precursor shock, and a third one in the martensite (behind the phase transformation).

However, the main purpose in introducing dissipation is to explain the broadening of the second rise, after the first sharp one produced by the arrival of the precursor shock, in the free surface experimental velocity plots. It is clear that, for this, the dominant effects will occur in the critical austenite region, as the waves reflected back from the free surface (produced when the precursor shock arrives) propagate into this region and interact with the oncoming phase transformation front. Thus, a *much simplified viscosity–approach is possible: we simply use two values for the viscosity, one (valid everywhere in space) for times before the precursor shock reaches the free surface, and another one for the times after this event.* To be specific: in the equations in (4.2) we take the effective viscosity μ as a piecewise constant function of time. In this two viscosity model $\mu = \mu_1$ throughout the sample until the precursor shock strikes the free surface. After this collision the value of μ is changed to $\mu = \mu_2$ everywhere in the sample. This simple approach should be able to capture the main changes that the introduction of dissipation causes on the free surface motion.

The numerical experiments we conducted with the dissipative algorithm can thus be described as follows: the code was run with various values of the two viscosities, and (by trial and error) these values were adjusted to have the best fit with the experiments. It is important to point out that **the same two viscosity values were used to simultaneously find the best fit to all the experimental curves**, so that the good fits we obtained (see figure 4-4) are not merely a consequence of adjusting enough free parameters.

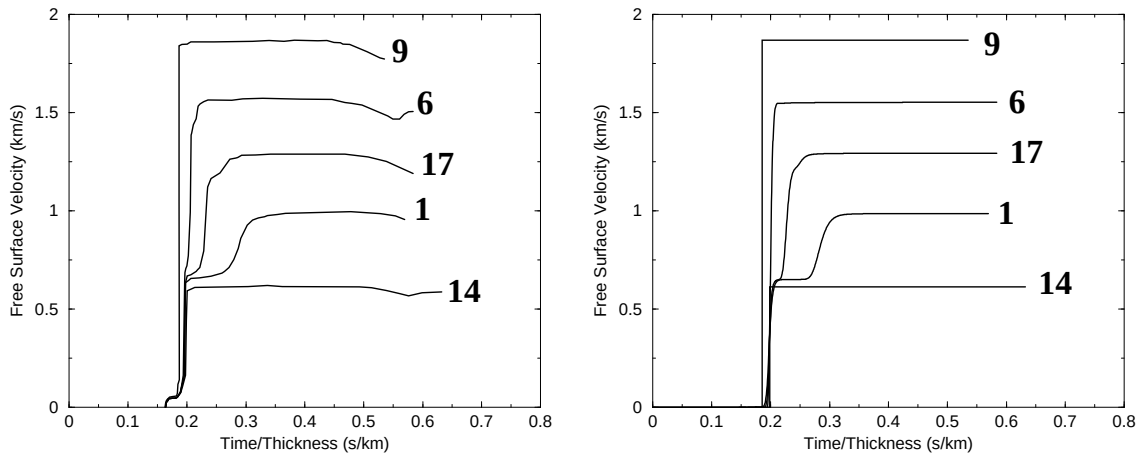

Figure 4-4: Comparison between the Barker and Hollenbach experiments and the numerical solutions to the two-viscosity model, where the values of the two viscosities (the same for all the curves) are selected to optimize the fit. The actual viscosity values used are given in subsection 4.2.5.

The arguments in subsection 4.1.1 suggest that the "first" viscosity (the one valid in the sample ahead of the precursor shock) should be low. This is consistent with the experimental results, since this viscosity determines how spread-out the precursor shock is, and the first wave in the experimental plots is very sharp. It is only the second wave that is broad, which agrees with the idea that it is the material behind the precursor shock that is highly dissipative — due to the cracking induced on the crystalline structure by local phase transformations, as explained in subsection 4.1.1.

The results of our investigation are summarized in figure 4-4, which shows a remarkably good agreement — given the simplicity of the theory. In fitting the values of the two viscosities, the actual process we used is as follows: we first found the value of the (small) first viscosity, to have the best fit between calculations and experiments for the first wave. Then the value of the (large) second viscosity was found, so as to have the best fit with the second wave. We point out that the results shown are rather insensitive to the value of the first viscosity, in so much that we obtain good agreement with the experiments as long as it is sufficiently small. The sensitivity to the second viscosity is not large either, in so far as small factors (two or three) up and down do not make much of a difference. But the order of magnitude is pinned down with certainty.

4.2.5 Validity of Viscosity Value

The values of the two effective viscosities leading to the best fit curves shown in figure 4-4, calculated using the process described in subsection 4.2.4, are

$$\left.\begin{array}{rcccl} \mu_1 & = & 9.11 \times 10^1 \text{ Pa sec} & = & 9.11 \times 10^2 \text{ P}, \\ \mu_2 & = & 1.27 \times 10^3 \text{ Pa sec} & = & 1.27 \times 10^4 \text{ P}, \end{array}\right\} \tag{4.19}$$

where the unit used is the CGS unit for dynamic viscosity, the Poise. Note that

$$1P = 1 \, \frac{\text{gr}}{\text{cm sec}} = 0.1 \, \frac{\text{kgr}}{\text{m sec}} = 0.1 \, \text{Pa sec}$$

and that (as a point of comparison), for water under standard conditions: $\mu \approx 10^{-2}$ P. It is also important to note that, while the values above in (4.19) are the exact ones used to obtain the curves in figure 4-4, these curves are not very sensitive to the particular values used — as pointed out at the end of subsection 4.2.4. Thus, the three digits displayed here should not be taken seriously, with the value of μ_1 merely indicating an upper bound on how large the first viscosity can be taken,[1] and the value of μ_2 giving a rough idea (within a factor of two or so) of the appropriate size for the second viscosity.

Obviously, we *can interpret the process leading to* (4.19) *as that of providing a rough measurement of the effective viscosity — or dissipation coefficient — under the conditions of a large dynamic load produced by the precursor shock in the experiments by Barker and Hollenbach.* The natural question is now: are these numbers reasonable? Is there agreement with other measurements, under similar conditions, to be found in the scientific literature? Clearly, there is no problem with the value of μ_1 we obtained. This value should be interpreted as merely an upper bound on what the two–viscosity model requires for agreement with experiments, and the value is quite consistent with the values viscosity has for most fluids under normal conditions (i.e.: these values do not exceed μ_1 above). The real question has to do with the value of

[1] Clearly, with more precise data on the first wave, better values for μ_1 would be easy to obtain.

μ_2, which is actually quite large (six orders of magnitude larger than the viscosity of water, for example). We consider this issue next.

Unfortunately, due to the extreme pressures experienced by the sample, direct measurements of the viscosity under these conditions would be very hard, and we were unable to find any within the published literature. The only form of iron under pressures comparable to the ones studies here discussed in the literature, is molten iron in a liquid state. Admittedly, molten iron and solid α or ϵ iron are drastically different phases of the same material. Thus, in any comparison of this sort, the best we can hope to achieve is order of magnitude agreement — which would, at least, give us some extra degree of confidence in the numbers we obtained; or prove us wrong if no agreement occurs.

In molten iron at the high pressures involved, experimental measurements (again) would be very hard, and we found none published. But theoretical calculations have been performed by a number of authors, mostly motivated by geophysical applications. Namely: most of the Earth's core is believed to be composed of molten iron, at a pressure about 10 times as large as the critical pressure for the α–ϵ phase transformation we have been studying [37]. A determination of the viscosity of the molten core is needed, for example, to explain the damping of radial seismic wave modes propagating in the earth [1]. It is thus *interesting to compare the value of the (second) viscosity μ_2 we obtained, with the theoretical predictions from the geophysical literature.*

A thorough literature review of published dynamical viscosity calculations for the Earth's core is presented in [64]. The values reported there for the viscosities in the outer core span 14 orders of magnitude, from 10^{-2} P on the lower end, to 10^{12} P on the upper end. This huge variation is due, in part, to the varying number of ways used to arrive at the values of the parameter, most of which are very indirect (and probably not too reliable). The approaches include (for example) extrapolation from values measured at lower pressures, measurements based on the changes in the Earth's magnetic field over geological time scales, molecular dynamical simulations, and others. The important fact for us, however, is that *the value of μ_2 reported in*

(4.19) *is in the middle of this range.*

A second source of measurements, that we can use as a comparison check with our value for the second viscosity, is provided by the measurements of effective viscosities based on shock propagation experiments (without phase transitions) in solids [3, 58, 63, 67]. For example, Band [3] used the approach of comparing the analytic viscous profile for a shock wave with the experimental profile, to obtain a value for the viscosity. Typical values for the viscosities obtained by these approaches are exemplified by the values (for aluminum) given by Prieto et al. [58] at 1.4×10^3 P, and by Sakharov et al. [63] at 2×10^4 P. Both of these values are not too far away from the one for μ_2 in (4.19) — with a close match not expected, since these shock experiments were done either for materials not exhibiting phase transformations, or with (relatively small) pressure jumps that do not result in a phase transformation.

4.3 Equation of State Modifications

In this section we consider an alternate physical means by which the Bruno-Vaynblat model could be modified to give more realistic free surface velocity plots, for *impacts in regime B*. As stated above, a modification to the austenite equation of state could be made in hopes of effecting the free surface. When one looks at figure 3-3 (a) on page 51, one sees that the width of the reflected fan, W_2^L, is quite narrow. In all of the regime B cases this left-facing rarefaction wave is traveling into a region of austenite at its critical pressure. Along its path this rarefaction fan collides with the phase transformation wave, $W_1^{R,b}$. One of the results of the ensuing interaction is a reflected *composite simple* wave called W_3^R, see subsection 3.2.2. It is this composite wave, that collides with the free surface and affects the free surface velocity plots. In fact when this wave reaches the free surface a second jump in velocity is recorded. Experiments suggest that the second wave should be "smooth", and one speculates that this might happen if the rarefaction wave W_2^L were not so narrow.

As mentioned in section 3.2, the speed of the head of the leading edge of the W_2^L wave is given by the derivative of the equation of state at the critical pressure

of austenite (also see equation (4.20) of this section). This speed, and therefore the equation of state, plays a very influential role in determining the *thickness* of the reflected fan, W_2^L, and correspondingly the *size* of the interaction region that forms when this rarefaction fan collides with the forward phase transformation. Intuitively the larger the width of this reflected fan the larger the interaction region and therefore the larger the reflected composite simple wave, W_3^R that is sent towards the free surface, see subsection 3.2.1 regime B. In contrast to what happens with a Mie-Grüneisen equation of state, if the reflected composite simple wave, W_3^R, is significantly *wide* it might not break before it reaches the free surface and the resulting free surface profile for the second wave would not be so steep, see subsection 3.2.2. If we can prevent shock formation in the W_3^R simple wave we might have a chance at improving the agreement between theory and experiment.

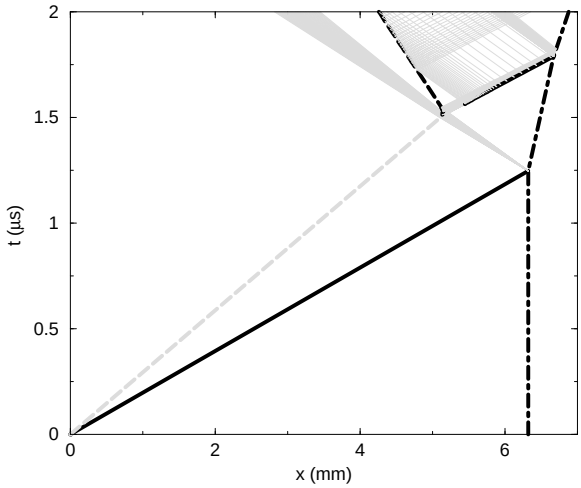

Figure 4-5: Space time plot of the reflected fan, computed with Mie-Grüneisen equation of state, interacting with the phase transformation wave in a typical regime B situation.

To investigate the effect the austenite equation of state has on the free surface (through the means mentioned above) we modified the equation of state slightly in a neighborhood of the critical pressure p^A_{crit}. The attempt was to *increase* the speed of sound at this point and correspondingly the speed of the head of the reflected rarefaction fan. The speed of sound in an Eulerian coordinate system is given by

$$c^2 = -\mathrm{v}^2 \frac{\mathrm{dp}}{\mathrm{dv}}\,. \tag{4.20}$$

From this expression we see that in order to increase the value of the sound speed we need to decrease the value of $p'(\mathrm{v})$ at the critical volume. We note in passing that the definition of the sound speed at *critical* is somewhat ambiguous. Mathematically, it is proportional to $p'(\mathrm{v})$ as in equation (4.20). For the $p(\mathrm{v})$ relationship used to investigate phase transformations, however, the analytical description of the v-p relationship changes at this critical value, see equation (2.4). Thus this derivative at critical can only be defined using one-sided limits. Physically the speed of sound should correspond to the speed at which small disturbances, expansive or compressive propagate. When the pressure is critical, however, the material cannot be compressed any further without a phase transformation. To expect this one-sided limit of the slope of the Mie-Grüneisen equation of state to be an accurate representation of the sound speed would be naïve. In fact, the equation of state near the region in which the actual phase transformation takes place is very poorly understood overall. Small modifications to the equation of state in the region near the forward transformation pressure of austenite would certainly be beyond experimental error.

The Mie-Grüneisen equation of state, used in all the sections of this thesis as an equation of state for both austenite and martensite (until now), consisted of the following functional form for the pressure as a function of volume, see appendix B

$$p(\mathrm{v}) = \rho_0 \mathrm{a}_0^2 \frac{\eta(\mathrm{v})}{(1 - \mathrm{s}\,\eta(\mathrm{v}))^2}\,. \tag{4.21}$$

Here ρ_0, a_0, and s are material dependent constants and η is the fractional volume change from some reference state $\tilde{\mathrm{v}}_0$ or

$$\eta(\mathrm{v}) \equiv \frac{\tilde{\mathrm{v}}_0 - \mathrm{v}}{\tilde{\mathrm{v}}_0} = 1 - \frac{\mathrm{v}}{\tilde{\mathrm{v}}_0}\,. \tag{4.22}$$

The value of $\tilde{\mathrm{v}}_0$ is normally taken to be the specific volume of austenite at zero pressure, or $\tilde{\mathrm{v}}_0 = 1/\rho_0 \equiv \mathrm{v}_0$. We see that $\eta > 0$ corresponds to compression of this volume and $\eta < 0$ corresponds to expansion. The variable η will be used to simplify the presentation whenever possible.

Rather than modify the existing austenite Mie-Grüneisen equation of state given

above, we will construct a new one that is not very different from the original. The new equation of state will enable better control over the slope at critical. In constructing this new equation of state for austenite the following, well established criterion, must be satisfied.

1. $p(\mathrm{v}_0) = 0$. The pressure at the rest state for austenite must be zero.
2. $-\mathrm{v}_0^2 \frac{\mathrm{dp}}{\mathrm{dv}}\Big|_{\mathrm{v}_0} = \mathrm{c}_0^2$. Here c_0 is the well documented sound speed in austenite at the reference volume v_0.
3. $p(\mathrm{v}_{\mathrm{crit}}) = \mathrm{p}_{\mathrm{crit}}$. The pressure at the *known* critical volume is the *known* critical pressure.
4. $p'(\mathrm{v}) < 0$. The pressure increases with decreasing specific volume.
5. $p''(\mathrm{v}) > 0$. The pressure is a convex function.

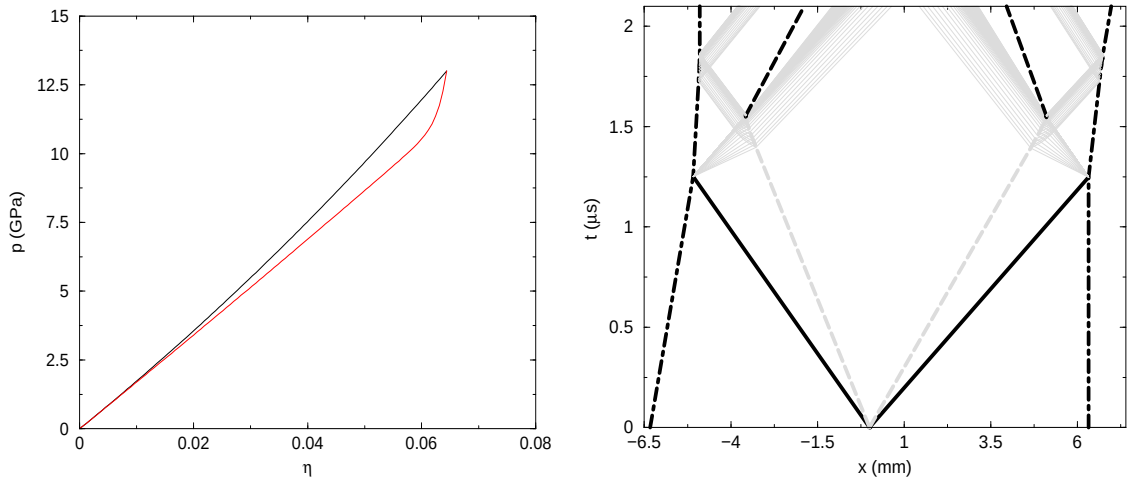

Figure 4-6: On the left, comparison of the Mie-Grüneisen equation of state with the exponential one proposed in equation (4.24). On the right, space-time wave diagrams for an impact in regime B for the α–ϵ phase transition in iron, done using the modified equation of state in equation (4.24).

These last two criteria are required from purely thermodynamic constraints on the equation of state, see for example [18, p. 5]. While satisfying all of these requirements we would like to be able to make the sound speed at critical as large as possible. The

sound speed at critical can be written as

$$c_{\rm crit}^2 = -{\rm v}^2 \frac{{\rm dp}}{{\rm dv}}\Big|_{{\rm v}_{\rm crit}} = {\rm v}_0 \left(1-\eta\right)^2 \frac{{\rm dp}}{{\rm d}\eta}\Big|_{\eta_{\rm crit}}, \tag{4.23}$$

and an equivalent statement to maximizing $c_{\rm crit}$ is to maximize $\frac{dp}{d\eta}|_{\eta_{\rm crit}}$. To achieve control over the slope of $p'(\eta)$ at critical, we took a $p = p(\eta)$ equation of state of the following form

$$p(\eta) = a + b\, e^{\eta} + c\, e^{\frac{(\eta-\eta_{\rm crit})}{\epsilon}}. \tag{4.24}$$

Requiring conditions 1, 2, and 3 from the above list gives three equations for the three unknowns a, b, and c. These equations can be easily solved. With these three coefficients now determined in terms of known quantities we see that $p'(\eta_{\rm crit})$ is given by

$$p'(\eta_{\rm crit}) = b\, e^{\eta} + \frac{c}{\epsilon}\, e^{\frac{(\eta-\eta_{\rm crit})}{\epsilon}}\Big|_{\eta_{\rm crit}} = b\, e^{\eta_{\rm crit}} + \frac{c}{\epsilon}, \tag{4.25}$$

and smaller values of ϵ give larger values of $p'(\eta_{\rm crit})$ and correspondingly greater values for the sound speed. The value of ϵ is modified to increase the width of the reflected rarefaction fan. The value of ϵ we used in the equation of state is 1.5×10^{-3}.

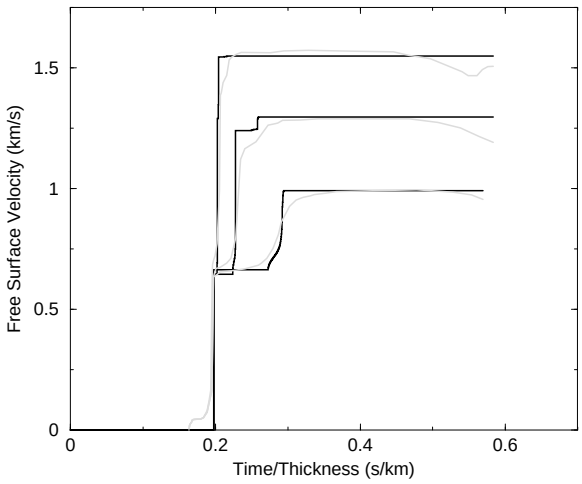

Figure 4-7: Comparison between Barker and Hollenbach experiments experimental free surface profiles and theoretical free surface profiles predicted from equation (4.24).

For comparison, we plot the $p(\eta)$ formula of the austenite Mie-Grüneisen equation of state and equation (4.24) in figure 4-6 (left). Notice that the two curves generally agree over a fairly long range of η's but begin to diverge as we approach the critical pressure. We see that the sound speed of the modified equation of state increases greatly over that of the Mie-Grüneisen equation of state at the critical pressure.

In figure 4-6, we present the (x,t)-diagram, for the first experiment considered by Barker and Hollenbach, see reference [5]. We note that the reflected rarefaction fan is indeed much larger when compared with those obtained with the Mie-Grüneisen equation of state (compare with figure 3-3). We can also see from this figure that the increase in sound speed brought about by this equation of state does indeed widen the mixed simple wave reflected off the phase transformation, or wave W_3^R. In fact this mixed simple wave is now wide enough that it does not break on its way to the free surface. This in contrast to the behavior predicted to arise from a Mie-Grüneisen equation of state. This indicates that the approach used in this section does indeed have the correct general effect on the behavior, though (as the next paragraph makes clear) it is not enough to provide a complete agreement with the experimental data. More work along this lines is needed, probably incorporating both the ideas hear and the two-viscosity approach used earlier.

In figure 4-7 one sees the effect the modified equation of state has on three representative free surface plots that correspond to regime B impacts. The interesting result seen here is that the curvature of the theoretical plots near the *beginning* of the second wave matches very well with the experimental ones. The agreement between the two sets of curves in the second wave is not as good for later times. The fact that the agreement between theoretical and experimental curves improved so much in the initial region may be an indication that more investigation into the equation of state near the critical pressure of austenite is warranted.

In the following chapter we present a new numerical scheme developed in the course of working on this problem and used in the presentation of many of the results in this chapter.

Chapter 5

The Characteristic Tracking Method

5.1 Introduction

In the previous chapter additional physical arguments were suggested for improving the agreement between theory and experiment for a set of iron impact experiments. Once each additional physical principle is put forth the resulting mathematical models are then implemented numerically. A new numerical scheme (the *Characteristic Tracking Method*: CTM) that resulted from this investigation of solid–to–solid phase transformations is presented here.

In this chapter we develop a numerical method for solving one-dimensional 2x2 nonlinear hyperbolic partial differential equations. The CTM scheme developed during the investigations reported in chapter 1. There the need arose for accurate calculations of interactions between rarefaction fans and discontinuous waves, including shocks, contact discontinuities, and phase transformations. The characteristic tracking method has several important advantages over other methods currently in existence for the numerical solution of nonlinear hyperbolic systems. The CTM is very accurate at following interfaces between two regions, since it can resolve discontinu-

ities, fan edges, and boundaries between simple waves[1] to *one* node of accuracy. After development we found the characteristic tracking method to perform extremely well in practice.

5.2 Previous Numerical Methods

Numerical methods for nonlinear hyperbolic equations have had a long history. The methods of Courant et al. [19] and Lax and Friedrich [44], developed in the early 1950s, stand out as the first attempts at the numerical solution of problems of this type. Since then a large number of schemes have been developed. The early approaches relied on the application of finite difference techniques. Of particular importance is the pioneering work of Lax and Wendroff [45, 46, 47] on space–centered schemes. This work lead to several centered three–point schemes for one–dimensional hyperbolic equations, a popular one being that of MacCormack [50].

Additional finite difference methods can be derived that relate more closely to the physical propagation properties of the nonlinear hyperbolic equations. These "non–space–centered" schemes can be classified as *upwind* schemes. The first explicit upwind scheme appeared in the work of Courant et al. [19]. Since then several extensions have appeared [57]. The flux vector splitting methods of Steger and Warming [66] and Van Leer [48] can be considered upwind methods due to their directional discretization of the flux derivatives.

A very original approach to the numerical solution of nonlinear hyperbolic problems was taken by Godunov [28]. He approached the solution to the global problem by solving many *local* Riemann problems. This use of an exact nonlinear solution locally to approximate the flow has lead to a host of schemes that introduce different Riemann solvers [25, 61, 60, 56]. Several attempts have been made to extend Godunov's ideas to second order, see [16, 17, 29, 30, 31, 33, 34, 69, 70].

The principal difficulty encountered in the numerics of nonlinear hyperbolic systems stems from the fact that the mathematical equations themselves can develop

[1] Boundaries of this last type occur in the investigation reported in chapter 1 (see subsection 3.2.2).

discontinuities in finite time from smooth initial conditions see [49]. These discontinuities (shocks and contact discontinuities) are notoriously hard to resolve numerically. Most of the schemes described above suffer their greatest difficulties around the locations of these moving interfaces. The numerical problems involved range from the miscalculation of their speeds, to unphysical oscillations present before or after their location, to excessive smearing of their wave profiles.

Many additional numerical schemes have been invented in an attempt to correct for the problems mentioned above. One such idea, aimed at correcting oscillations generated by the shock, is to introduce a non–physical viscosity into the governing equations themselves [55]. Another approach aims at preventing the generation of numerical oscillations before they occur. This approach is based on the concept of non–linear *limiters*, introduced initially by Boris and Book [9] and Van Leer [68]. This work eventually lead to the concept of *total variation diminishing (TVD)* schemes, first introduced by Harten [29]. Many of these traditional ideas and concepts are introduced and discussed in LeVeque's book [49].

Based on the shortcomings mentioned above, some simple idealized requirements that a numerical scheme for nonlinear hyperbolic systems should satisfy can easily be stated. Namely:

1. Detection and resolution of the discontinuities as they are created, automatically, without user intervention or a priori knowledge of the solution to the equations.

2. The mathematical idea of a discontinuity (a jump over zero width) should be a goal, in the representation of discontinuities in the flow. That is, the resolution of discontinuities should be as exact as possible. Numerically this means using as few computational grid points as possible for each discontinuity.

3. No oscillations around propagating discontinuities.

4. Discontinuities propagating with speeds that satisfy the Rankine-Hugoniot conditions, and are therefore correct.

5. Conservation of the appropriate quantities (mass, momentum, etc).

The characteristic tracking method satisfies all of the above requirements for the numerical solution of one-dimensional nonlinear hyperbolic systems, as well as some additional requirements that are not listed. For instance, certain applications, such as the solution to conservation equations with non-convex equations of state, can produce simple waves of *different* compressibilities traveling together[2]. When numerically solving such systems, it is desirable to be able to keep accurate track of the boundaries between the two different types of simple waves. This is possible with the characteristic tracking method.

5.3 Mathematical Background

Here we present the numerical algorithm as it would be applied to the problem considered in chapter 1, written in Eulerian coordinates. The relevant equations (conservation of mass and momentum), are repeated here for ease of reference. They are

$$\frac{\partial}{\partial t}\rho + \frac{\partial}{\partial x}(\rho\, u) = 0\,, \qquad \frac{\partial}{\partial t}(\rho\, u) + \frac{\partial}{\partial x}(\rho\, u^2 + p) = 0\,, \tag{5.1}$$

with p a *known* function of ρ. The relevant Rankine-Hugoniot conditions are

$$-S\,[\rho] + [\rho\, u] = 0\,, \qquad -S\,[\rho\, u] + \left[\rho\, u^2 + p\right] = 0\,, \tag{5.2}$$

where S is the speed of the discontinuity.

For this system a pair of Riemann invariants always exists, namely:

$$s = -\frac{1}{2}\left(u - l(\rho)\right), \qquad \text{and} \qquad r = +\frac{1}{2}\left(u + l(\rho)\right), \tag{5.3}$$

where s is the *left-going* Riemann invariant (constant along the characteristics $\frac{dx}{dt} = u - c$), while r is the *right-going* invariant (constant along $\frac{dx}{dt} = u + c$), and $l(\rho)$ is

[2]For an example of such a situation see subsection 3.2.2.

defined as

$$l(\rho) = \int_{\rho'}^{\rho} \frac{c}{\rho}\, \mathrm{d}\rho = \int_{p'}^{p} \frac{\mathrm{d}p}{\rho c}\,. \tag{5.4}$$

Notice that, since $l'(\rho) = c/\rho \neq 0$, ρ can be written as a function of l. Note also that the mathematical equations themselves *conserve* the quantities s and r. This fact will be *explicitly enforced* in the formulation of the characteristic tracking method.

$$u = r - s\,, \qquad l = r + s\,, \tag{5.5}$$

so we can use s and r as independent variables if desired.

5.4 Description of the Algorithm

The algorithm described here relies heavily on the use of a Riemann solver. It will be assumed that a Riemann solver for the hyperbolic system under consideration is known. For the particular system of equations considered here (a mathematical model of martensitic solid–to–solid phase transitions) , a Riemann solver was developed in subsection 2.2.1.

The CTM algorithm is somewhat analogous to the original ideas of Godunov [49]. In Godunov's work the flow is evolved indirectly by means of solving Riemann problems at the interface between two cells. In each cell an average value of the state is defined. Then at each *fixed* node[3] the flux is computed using the solution of the corresponding Riemann problem. These fluxes are then directly used to update the average state variables in a conservative way [28]. The averaging present in the first step of Godunov's method is what smears shocks.

As mentioned in subsection 2.2.1, the solution of a Riemann problem consists of a left-facing and a right-facing wave, each of which can be either a shock or a rarefaction fan. Vaynblat modified the ideas of Godunov's slightly in his Ph.D. thesis [71], permitting the computational grid to move when the solution of a particular Riemann problem produces a sufficiently strong shock. With this modification the numerical

[3]In Godunov's original work the grid used is stationary.

grid follows discontinuities and only one grid point is needed to represent shocks[4]. Vaynblat's method, however, in the smooth regions of the flow, still relies on averaging and a fixed numerical grid. In this manner it is very similar to the original Godunov method. As a consequence, his resolution of rarefaction fans resulted in a smearing of the fan edges. His algorithm also did not rely on the use of Riemann invariants and as such did not implicitly enforce their conservation. In contrast the characteristic tracking method relies heavily on the use of conserved Riemann invariants and involves *no averaging*.

We state here the *numerical* goal of the algorithm as an aid in understanding the definitions below.

A CTM flow will be defined as one in which:

1. *The numerical approximation of the solution will consist only of constant states. These constants states can be arbitrarily small in regions of smooth flow.*

2. *These constants states are separated only by* discontinuities *that travel at constant speeds.*

Remark 5 *When the flow consists of only discontinuities separated by constant states (as specified above), the numerical solution is quite simple. First, propagate all discontinuities until two of them collide. At the point of their collision solve another Riemann problem. If all waves produced from this Riemann problem are discontinuous, we have evolved the flow forward in time and returned to the same qualitative flow description that we started with: that of constant states separated by discontinuous waves (or a CTM flow). Assuming all Riemann problems encountered produce discontinuous waves, the flow field can easily be evolved forward in time. The simple*

[4]Vaynblat's method is similar to the method of Harten and Hyman and borrows their idea of a moving grid [32].

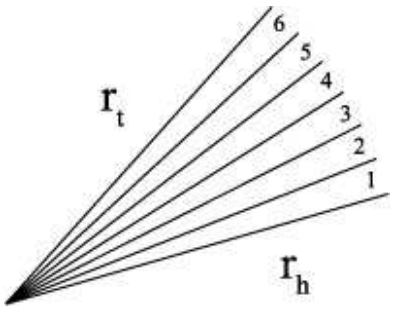

Figure 5-1: Discretization of right-facing rarefaction fan with 6 constant state wedges and 7 characteristic waves.

heuristic idea of "propagate until collision" can be applied over and over until the solution has evolved to a desired time. This algorithm can no longer be continued once a single Riemann problem produces a rarefaction fan. The question then arises, can the heuristic approach of "propagate until collision", be used (with modification) even when fans are present.

If every wave (even continuous rarefaction fans) produced by a Riemann problem could be broken up one or many *discontinuous* "waves", each moving at its own constant speed, then the problem could be numerically solved according to the "propagate until collision" strategy. The two questions that need answering then become

1. How to discretize continuous rarefaction fans into discontinuous "waves" satisfying the criterion above.

2. How to properly generalize any Riemann problem that involves these new "waves".

The answer to the first question is rather simple and will be discussed here. The answer to the second question depends on the wave types that enter the interaction and will be considered in subsections 5.4.2 and 5.4.3.

To motivate the answer to question number 1 we note that each fan can be drawn in the (x, t)-plane as a sequence of characteristics (of the same family) stemming from one point. The characteristics of the opposite family then cross the fan. From the definition of a simple wave, the invariant associated with these crossing characteristics

is constant. The discretization we choose explicitly enforces this observation. We require that the jump in the *continuous* invariant across each inserted wave is zero.

As an example assume that we have a right-facing rarefaction fan, see figure 5-1. In this case the left invariant $s = s_0$ is constant throughout the fan, while the right-facing invariant decreases from the value r_h (on the right, or head of the wave) to r_t (on the left, or tail of the wave). Next we discretize this fan into N wedges of constant states. The jump in the right-going invariant, r, in moving from one wedge to the next, is given by $\Delta r = \frac{r_t - r_h}{N+1}$. Thus the state in the i-th wedge is $(s_0, r_h + \Delta r\, i)$ where i is counted from the head of the fan (starting at zero), towards the tail (where it takes the value $N+1$), see figure 5-1. Between the i-th and $i+1$-st wedge, we insert a characteristic wave[5] traveling at the speed of sound given by a state that is the average of the state in i-th and $i+1$-st wedges. That is the sound speed in the state given by

$$\left(\frac{1}{2}(s_0 + s_0), \frac{1}{2}(r_h + \Delta r\, i + r_h + \Delta r\, (i+1))\right) = \left(s_0, r_h + \Delta r\, i + \frac{\Delta r}{2}\right) .$$

At this time the continuous centered rarefaction fan is now replaced by $N+1$ characteristic waves, moving to the right, separated by N wedges of a constant state. For a left-facing rarefaction fan the procedure used to discretize is similar.

To help in the presentation of the answer to question number 2, we make the following definitions.

- A **numerical characteristic wave** is a propagating discontinuity such that the jump in *one* invariant across it is zero. In a sense the numerical characteristic wave is like a true characteristic in that when the difference in states across it shrinks to zero, it becomes a true characteristic of the flow field. These are the waves used in the discretization of rarefaction fans. This is in contrast to what we now define as a numerical discontinuity wave.

- A **numerical discontinuity wave** is a propagating discontinuity in which *both*

[5] To be defined later but for now simply think of this as a characteristic.

Riemann invariants jump upon crossing the wave. Intuitively a discontinuity wave is similar to a shock wave but is not restricted to this. Depending on the system of equations, other waves can be classified as numerical discontinuity waves for example, a contact discontinuity or a phase transformation.

With these definitions we are ready to describe the numerical algorithm. From whatever initial condition we are interested in, we construct, using cell averaging perhaps, an initial condition consisting of piecewise constant data. To start the numerical solution we next solve the Riemann problem at each cell interface, with the given Riemann solver. The solution of each Riemann problem introduces two waves, one left-facing and one right-facing. On average, half will be rarefaction fans and the other half shocks. Shocks are discontinuities that carry a jump in both invariants and are therefore discontinuity waves without modification. A rarefaction fan is however continuous. The discretization introduced above is applied to each rarefaction fan and a CTM flow results.

After we have discretized all fans produced by the initial Riemann problems, numerically all output from each Riemann problem is of the same type: either characteristic or discontinuity waves (or both). Each of these waves is traveling at a known velocity from a known point of origin. As the velocities are constant, these waves are represented in an (x, t)-plane as straight lines. The time at which the first pair of waves collides from two neighboring Riemann problems can be calculated by simply finding the minimum, in time, of pairwise intersection of each pair of straight lines. Because of our chosen discretization of fans the solution of the flow is approximated by a sequence of constant states and waves and is therefore a CTM flow. At the point where the first two neighboring waves collide we have yet to explain how to continue the flow further. What we do depends on the type of numerical waves involved in the collision. The types of possible collisions are as follows:

1. The two colliding waves are both discontinuity waves.

2. The two colliding waves are both characteristic waves.

3. The two colliding waves are of different types: one is a discontinuity wave and the other is a characteristic wave.

Remark 6 *If the manner in which we resolve each collision produces only characteristic waves or discontinuity waves or both, the numerical solution after this collision is again a CTM flow and can be evolved forward in time by again looking for the earliest wave collision. Thus we have generalized the heuristic idea of "propagate until collision" discussed above, if we can insure that the results of the three intersection types produce only characteristic waves or discontinuity waves.*

In the next subsections we consider specifically how to resolve the interactions defined above.

5.4.1 Collision of Two Discontinuity Waves

In this situation both waves that make up a collision are discontinuity waves. At the exact instant of collision we have two constant states separated by a discontinuity. We compute the solution to the Riemann problem here using the given Riemann solver and discretize any fans that result as explained above. Following this procedure at the end of this interaction we will again have a CTM flow, and the algorithm continues.

5.4.2 Collision of Two Characteristic Waves

In this case we consider the situation where the two waves colliding are both characteristic waves. Two sub-cases become important see figure 5-2.

1. The two characteristic waves that collide are of *different* families, i.e., the wave collision is head-on.

2. The characteristic waves are of the *same* families, i.e., one wave in the pair is overtaken.

If the characteristic waves colliding are of different families, situation 1, we proceed as follows. At the collision point we construct two "outgoing" characteristic waves:

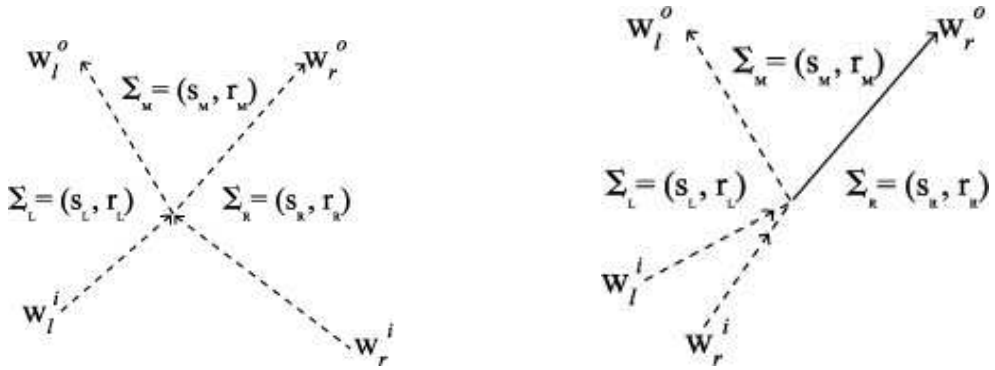

Figure 5-2: Collisions of characteristic waves. A head-on collision (left). An overtaking collision (right). Characteristic waves are drawn with dashed lines.

one left-facing characteristic wave and one right-facing characteristic wave, with a "middle" wedge (state) separating the two outgoing waves. See figure 5-2 (left) for notations. Across the outgoing left-facing characteristic wave, W_L^O, the right-facing Riemann invariant is constant. Similarly across the outgoing right-facing characteristic wave, W_R^O, the left-facing Riemann invariant is constant. We can then numerically compute the state in this middle wedge by taking corresponding invariants from the left and the right states. The middle state is then given by

$$(s_M, r_M) = (s_R, r_L)\,.$$

The velocities of the outgoing characteristic waves W_L^O and W_R^O are computed from the sound speed taken from averages of this newly computed middle state and the left and right states. For example, the velocity of W_L^O is taken to be the sound speed in the state given by

$$\left(\frac{s_L + s_M}{2}, \frac{r_L + r_M}{2}\right) = \left(\frac{s_L + s_R}{2}, r_L\right)\,, \tag{5.6}$$

and the speed of the W_R^O wave is taken to be the speed of sound in the state corresponding to

$$\left(\frac{s_M + s_R}{2}, \frac{r_M + r_R}{2}\right) = \left(s_R, \frac{r_L + r_R}{2}\right)\,. \tag{5.7}$$

If instead the characteristic collision involves characteristic waves of the *same* family, situation 2, we have a discretized version of two characteristics of the same family colliding. When this occurs in nonlinear hyperbolic systems a shock is born and needs to be inserted into the (x,t)-plane at the location of the collision. These two characteristics then converge on this shock. The numerics models this procedure exactly. As an example we consider the case when the two characteristic waves are right-facing, see figure 5-2 (right) for notations. At the point of the collision we produce two outgoing waves, a characteristic wave and a discontinuous wave. The outgoing right-facing wave representing the inserted shock will be a discontinuity wave and the left-facing wave will be a characteristic wave of the *opposite* family of the incoming characteristic waves. The middle state (s_M, r_M) in this configuration is computed as follows. Across the outgoing left-facing characteristic wave the right-going Riemann invariant is constant, this requires $r_M = r_L$. From the two Rankine-Hugoniot (5.2) equations applied to the discontinuity wave we can eliminate the velocity of the wave and obtain the following equation

$$u_R - u_M = -\sqrt{(v_R - v_M)\,(p_M - p_R)}\,. \tag{5.8}$$

If we write this equation in terms of the invariants in the middle state (s_M, r_M) we get the following

$$u_R - r_M + s_M = -\sqrt{(\mathrm{v_R} - \mathrm{v(l_M)})\,(\mathrm{p(l_M)} - \mathrm{p_R})}\,, \qquad l_M = r_M + s_M\,. \tag{5.9}$$

Here we recognize that the specific volume $\mathrm{v_M}$ and the pressure p_M are functions of l_M which is given directly by the sum of invariants. This gives one equation for one unknown s_M. This equation can then be solved numerically for the unknown s_M. Once both s_M and r_M are known one of the equations (5.2) can be used to calculate the speed of the shock.

The speed of the outgoing left-facing characteristic is given by the sound speed of an average state between (s_L, r_L) and (s_M, r_M) in a manner the same as presented in the explanation of a head-on collision of two characteristic waves, see equation (5.6).

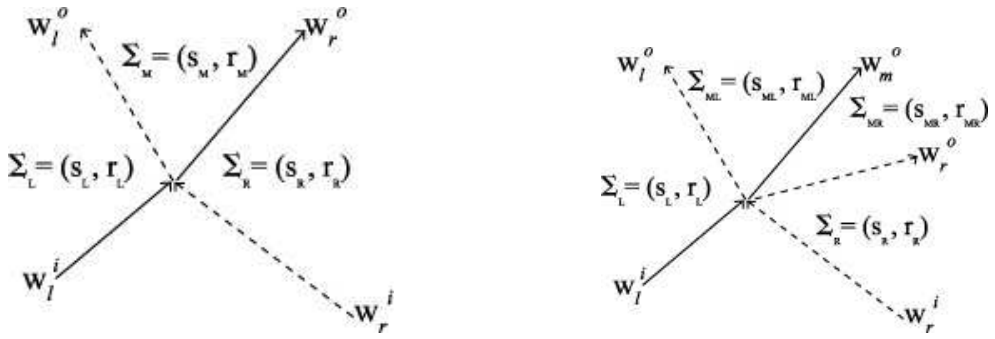

Figure 5-3: Numerical waves that are produced by a characteristic shock intersection (left) and a characteristic contact discontinuity intersection (right). Characteristic waves are drawn as dashed lines. Discontinuity waves are drawn as solid lines. The plot on the right can represent *either* a collision between a characteristic wave and a contact discontinuity or the collision between a characteristic wave and a right-facing phase transformation.

5.4.3 Collision of a Characteristic Wave and a Discontinuity Wave

Here we consider the situation where one of the incoming waves is a discontinuity wave and the other is a characteristic wave. The exact results obtained depend on the true characteristic structure of the actual wave represented by the discontinuity wave and the direction that each wave is traveling when it collides. We consider several examples to demonstrate the procedure used in each case.

Consider a right-facing shock that collides with either a left-facing or a right-facing characteristic wave. The characteristic structure of a right-facing shock is such that the C_+ characteristics converge on the shock from both sides, while the C_- characteristics pass through. After the collision, independent of the original direction of the characteristic wave, we produce a right-going shock and a left-facing or C_- characteristic wave. For an example of a head-on collision see figure 5-3 (left). The state and velocities of the waves that are produced are constructed exactly as in the case where two characteristic waves of the same family collide, see subsection 5.4.2.

As a second example consider the case that occurs when the discontinuity wave is formally a contact discontinuity. The characteristic structure of a contact discontinuity is that the true characteristics from both families pass through the wave. When

one of the numerical characteristic waves and a contact discontinuity collide the result of the collision is a left-facing characteristic wave, a right-facing characteristic wave and a central contact discontinuity. This structure is shown in figure 5-3 (right). To fill the states we proceed as follows: across the outgoing left-facing characteristic wave the right Riemann invariant is constant, and across the outgoing right-facing characteristic wave the left-going Riemann invariant is constant. This give two conditions for the "middle" invariants

$$r_{ML} = r_L\,, \qquad s_{MR} = s_R\,. \tag{5.10}$$

Across the contact discontinuity two equations hold

$$p(l_{ML}) = p(l_{MR})\,, \qquad u_{ML} = u_{MR}\,. \tag{5.11}$$

When written in terms of the invariants on either side of the contact, we obtain the following

$$p(s_{ML} + r_{ML}) = p(s_{MR} + r_{MR})\,, \tag{5.12}$$

and

$$r_{ML} - s_{ML} = r_{MR} - s_{MR}\,. \tag{5.13}$$

The second equation can be solved for an unknown, either s_{ML} or r_{MR}, here we solve for r_{MR} and substitute this relation into equation (5.12) obtaining

$$p(s_{ML} + r_{ML}) = p(2\,s_{MR} - s_{ML} + r_{ML})\,. \tag{5.14}$$

This is one equation with one unknown, s_{ML}. When this unknown is determined the states between all the waves are now specified. The contact discontinuity travels at the particle velocity which is known at this stage, while the velocities of each characteristic wave can be computed in the same way as they are in the head-on collision of two characteristics, see equations (5.6) and (5.7).

Other types of discontinuous waves besides shocks and contact discontinuities

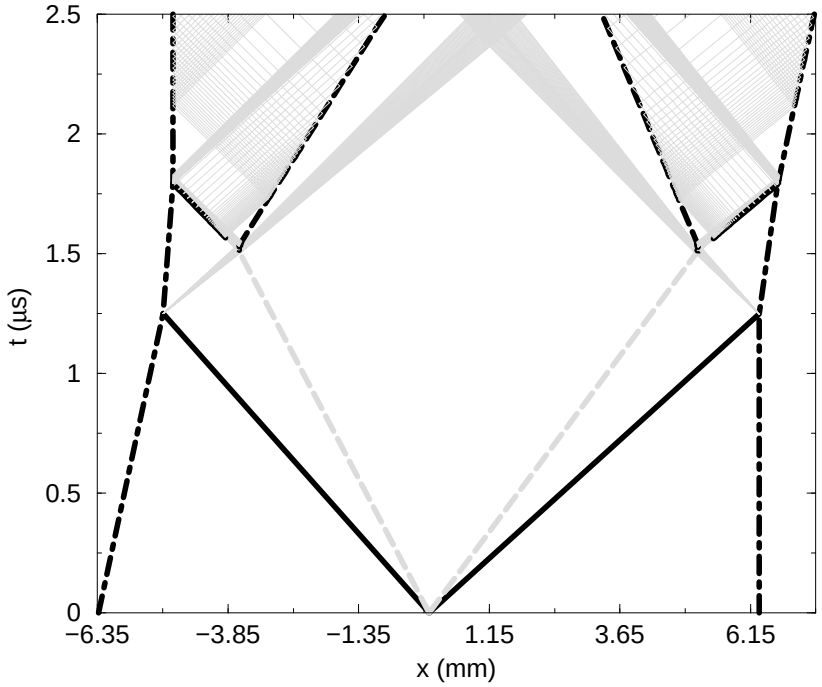

Figure 5-4: (x, t)-diagram for Barker-Hollenbach experiment number 1.

can be treated in a similar manner. For example, in chapter 1 the characteristic tracking method is used to solve the hyperbolic equations in an investigation of phase transitions in iron. There a type of "under-compressed" shock wave is found. The characteristic structure of these waves is such that the characteristics of the same family converge onto it from behind but not from ahead (see figure 2-4 (b)). As an example of the procedure used when the discontinuity wave is a phase transformation, consider the treatment of a head-on collisions. The result of this collision is three different waves: a characteristic wave of *each* family and a phase transformation wave. In this situation the character of the wave interactions looks exactly the same as that seen when a characteristic wave collides with a contact discontinuity, see 5-3 (right).

5.5 Numerical Results

As we said earlier, the characteristic tracking method was implemented for the hyperbolic system that arises in the study of martensitic phase transformations under shock loading. Here we present some of the numerical results obtainable. Since much

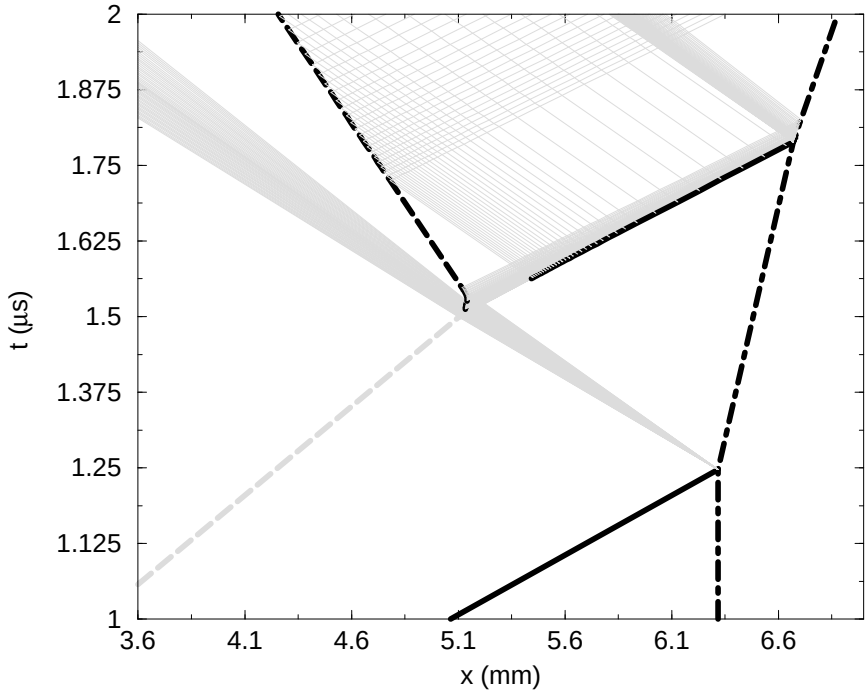

Figure 5-5: Magnified portion of (x, t)-diagram where the left-facing rarefaction fan and the forward transformation front interact.

of the background for this particular application has already been given in chapter 1, we will refer the reader to the exposition found there. Here we present results for the first experimental setup of Barker and Hollenbach. In this experiment all the various types of wave interactions the characteristic tracking method is designed to deal with can be seen. We first present an (x, t)-plot of all wave interactions, in figure 5-4. Here one can see both discontinuous waves and characteristic waves. Refer to the key presented on page 48 for an explanation of the line markings used in this plot. One can clearly see the locations and widths of the centered rarefaction fans and simple waves. Since the most interesting effects take place when the reflected fan interacts with the right-facing forward transformation wave, we show this region magnified in figures 5-5 and 5-6, and spend some time discussing it.

In figure 5-5 we see that the interaction of the rarefaction fan and the forward transformation front produces several waves. A left-facing and right-facing simple wave are present along with a backwards phase transformation. The simple waves are visualized as groups of left-facing or right-facing characteristic waves. Constant

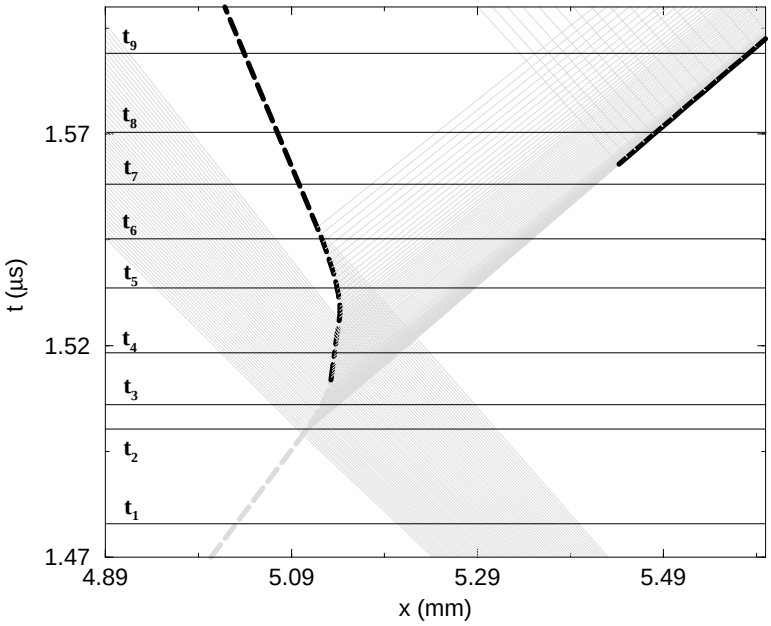

Figure 5-6: A further magnification of the interaction region. Horizontal lines represent the times pressure profiles were printed in figures 5-7 and 5-8

regions are see in pure white.

It is interesting to observe that the right-facing compressive wave breaks on its way to the free surface. The code produced the shock seen in figure 5-5 by detecting the crossing of two right-facing characteristics and inserted a shock. After the shock is born, later characteristic waves converge on it from behind and the numerical code produces left-facing characteristics waves as the result of the shock characteristic wave collisions (see subsection 5.4.3). In some regions the characteristic waves are spread far apart while in others they are much closer together. In the regions where they are much closer together the state variables change more rapidly.

To show the codes ability to capture the features around this interaction discussed above we have plotted the pressure as a function of x at ten different values of time. The values of time where pressure profiles are plotted are represented graphically on the (x, t)-plot in figure 5-6 as horizontal lines. The sequence of pressure plots is presented in figure 5-7 and 5-8. Please refer to the captions there for an explanation.

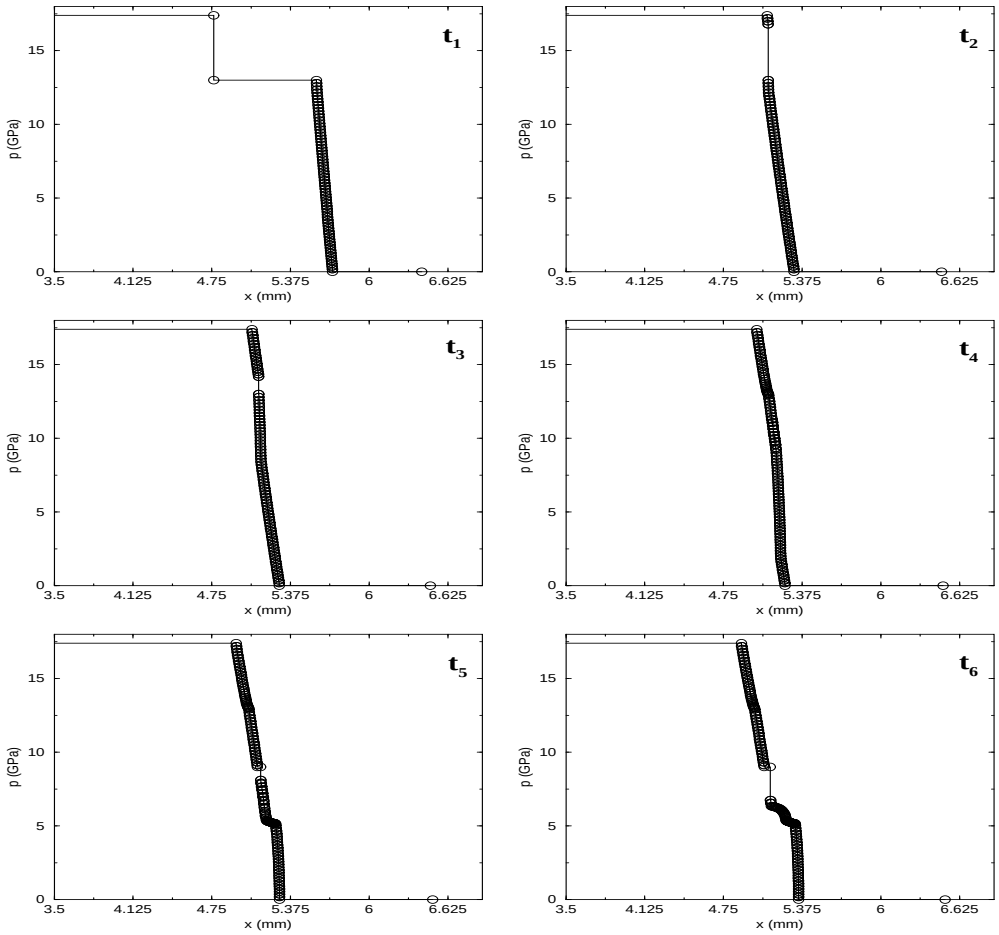

Figure 5-7: Sequence of timeslices of the pressure as a function of the spatial location x. The times at which these pictures were produced correspond to these represented graphically in figure 5-6 as horizontal lines. Plots are numbered from left to right, top to bottom. In plot t_1 the left-facing rarefaction fan is propagating towards the right-facing forward phase transformation front. In plot t_2 the two waves have just collided and some of the rarefaction fan has transmitted through the forward transformation front. In plot t_3 more of the rarefaction fan can be seen behind the forward phase transformation font, the forward phase transformation front itself has weakened in magnitude, and the compressive simple wave that is reflected from this transformation front can also be seen as a slight change in the slope of the $p(x)$ curve ahead of the transformation front. In plot t_4 the forward transformation front has weakened to the point that it must change types and is now a contact discontinuity. In plot t_5 the contact discontinuity has now become a weak left-facing backwards transformation front and the reflected simple wave from the interaction in beginning to steepen. In plot t_6 the full structure of the reflected composite simple wave is present.

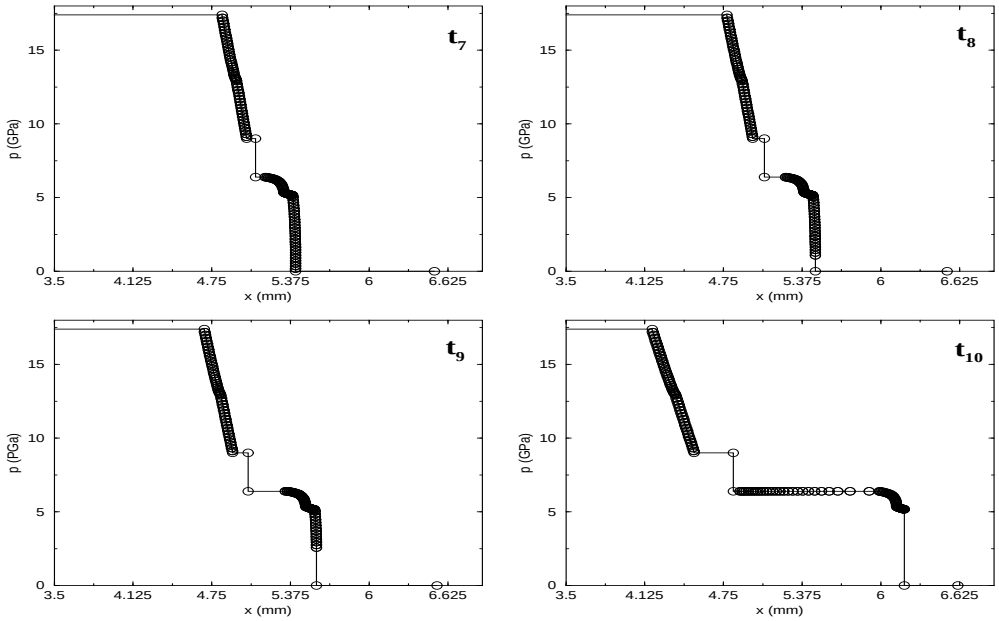

Figure 5-8: Sequence of timeslices of the pressure as a function of the spatial location x. The times that these pictures were produced correspond to these represented graphically in figure 5-6 as horizontal lines. Plots are numbered from left to right, top to bottom. In plot t_7 the right-facing compressive wave continues to steepen (from the profile shown in plot t_6). In plot t_8 this right-facing compressive wave *breaks* and the numerics inserts a shock. In plot t_9 the following pieces are clearly visible: the two components of the transmitted simple wave, the backwards phase transformation, the three components of the reflected simple wave. Plot t_{10} corresponds to a time slightly before the newly developed shock strikes the free surface.

Chapter 6

Conclusions

The problem of determining the details of what happens when iron is shock loaded is a difficult one. Direct controlled measurements are impossible to make under the huge pressures a phase transformation requires. The only measurements that can be made (at this time) are point measurements of the free surface velocity of an iron sample, where a shock wave causes the large pressures needed to trigger a phase transformation. Accurate modeling of the physics taking place in this situation is very difficult, since there is a multitude of effects that can be taking place inside the material — as the phase transformation occurs. These include the existence of regions in the sample with a mixture of phases, or where the transformation is only "partial".

The Bruno-Vaynblat model provides a simple approach to the problem, using only wave concepts in the modeling of martensitic phase transformations. Its formulation does not include complicated and hard to model effects — especially involving poorly understood physical processes, requiring the introduction of difficult to measure physical constants or functions. Even so, it is able to capture quite well the coarse fundamental effects observed in the experiments — as showed in chapter 3 of this thesis, where the model was implemented without the rarefaction discontinuity simplification that Bruno and Vaynblat used.

In order to increase the agreement between the Bruno-Vaynblat model and the experiments, some additional physics is needed. In this thesis we explored the effects

of adding to the model two new physical processes. These are: dissipation, and a modification of the equation of state near the critical transition pressure (for the austenite phase). The results of these modifications are as follows:

- *Addition of dissipation:* In this case we were able to obtain a very close match with the experimental observations. It is important to note that this match was obtained with *all the experiments*, using only two fitting parameters.
- *Modification of the austenite equation of state, near the critical pressure:* This also produces theoretical free surface velocity plots that agree quite well (for regime B impacts) with the observations, *using only one fitting parameter.* It will be left for future research to see if better predictions can be obtained by implementing more careful (local) modifications to the equation of state.

The results above indicate that both: a better understanding of how dissipation operates in the phase transition regime, and better measurements of the austenite equation of state (near the critical pressures) are needed to obtain better agreement between theory and experiments.

Finally, we point out that, in order to fully implement the Bruno-Vaynblat model (see chapter 3), a new numerical algorithm (capable of accurate and efficient calculation of the wave interactions that occur) was developed. This new scheme proved to be a very robust, stable and accurate method for the numerical solution of hyperbolic problems with standard and non-standard equations of state such as the ones used in this thesis to model phase transitions.

Appendix A

Lagrangian Formulation

Here we summarize some useful formulas, valid for the equations of motion in Lagrangian form (2.2). The quasi-linear matrix form of these equations is

$$\frac{\partial}{\partial t}\begin{pmatrix} p \\ u \end{pmatrix} + \begin{pmatrix} 0 & C^2 \\ 1 & 0 \end{pmatrix} \frac{\partial}{\partial \xi}\begin{pmatrix} p \\ u \end{pmatrix} = 0\,, \tag{A.1}$$

where $C \equiv \sqrt{-\frac{dp}{dv}} > 0$ is the acoustic impedance. The characteristic form for these equations is

$$\frac{\partial}{\partial t}p - C\frac{\partial}{\partial \xi}p - C\left(\frac{\partial}{\partial t}u - C\frac{\partial}{\partial \xi}u\right) = 0 \tag{A.2}$$

$$\frac{\partial}{\partial t}p + C\frac{\partial}{\partial \xi}p + C\left(\frac{\partial}{\partial t}u + C\frac{\partial}{\partial \xi}u\right) = 0\,. \tag{A.3}$$

Equivalently:

$$\frac{d}{dt}p - C\frac{d}{dt}u = 0 \qquad \text{along} \qquad \frac{d}{dt}x = -C\,, \tag{A.4}$$

$$\frac{d}{dt}p + C\frac{d}{dt}u = 0 \qquad \text{along} \qquad \frac{d}{dt}x = +C\,. \tag{A.5}$$

These can be written in *Riemann Invariant* form as

$$\frac{d}{dt}s = 0 \qquad \text{along} \qquad \frac{d}{dt}x = -C\,, \tag{A.6}$$

$$\frac{d}{dt}r = 0 \qquad \text{along} \qquad \frac{d}{dt}x = +C\,. \tag{A.7}$$

where

$$s \equiv u - l(p) \qquad \text{is constant along} \qquad \frac{d}{dt}x = -C\,, \tag{A.8}$$

$$r \equiv u + l(p) \qquad \text{is constant along} \qquad \frac{d}{dt}x = +C\,. \tag{A.9}$$

We have defined $l(p)$ as

$$l(p) = \int_{p'}^{p} \frac{\mathrm{d}p}{C}\,. \tag{A.10}$$

The two variables s and r are called the *Riemann invariants.*

The Rankine-Hugoniot jump conditions are

$$-S_L\,[\mathrm{v}] - [u] = 0\,, \qquad \text{and} \qquad -S_L\,[u] + [p] = 0\,, \tag{A.11}$$

where "[ ]" denotes the the jump in the enclosed quantity across the shock. That is $[Q] \equiv Q^b - Q^a$, where Q^b (Q^a) is the limiting value of Q behind (ahead) of the discontinuity and S_L is the speed of the discontinuity in the Lagrangian coordinate system. Physically $|S_L|$ is the mass flux through the discontinuity. Manipulations of the equations (A.11) give the 1-shock (resp. 2-shock) front equations

$$S_L = \mp\sqrt{-\frac{[p]}{[\mathrm{v}]}}\,, \qquad \text{and} \qquad [p] = S_L\,[u]\ . \tag{A.12}$$

Rarefaction fans are defined as flow in which one Riemann invariant is constant. From equations (A.8), (A.9), and (A.10) the velocity behind a rarefaction fan is given by

$$u^b = u^a \mp \int_{p^a}^{p^b} \frac{dp}{C}\,, \qquad \text{with} \qquad c = \sqrt{-\frac{dp}{d\mathrm{v}}}\,. \tag{A.13}$$

Appendix B

Mie-Grüneisen Equation of State

Quantitative predictions follow from the Bruno-Vaynblat model only after explicit constitutive relations (of the type required in equation (2.4)) are specified. We note that the conservation laws in (2.1) and (2.2), require an equation of state in the form of a relation $p = \hat{p}(\mathrm{v})$, for each phase. This type of equation of state is often called incomplete [54], because it does not involve any temperature dependence. Here we will use approximations for $p = \hat{p}(\mathrm{v})$ obtained directly from experimental results. In truth p is a function of other variables as well (for example temperature), but the dependence on these other variables is so weak that we may safely neglect them.

The function $\hat{p}(\mathrm{v})$ is determined experimentally as follows. Just as in the flyer-plate experiments described in chapter 1 a piece of the material under study is held stationary while an impactor is fired and undergoes a collision with the sample. This collision produces a shock wave that travels through the sample. The two measured quantities are the time at which the shock strikes the free surface, t_S, and the velocity u_p the shock imparts to the free surface after its collision. From the known thickness of the sample, h, one can determine the velocity of the shock from the equation

$$S = \frac{h}{t_S}\,. \tag{B.1}$$

Experimental measurements of this sort, done for a great number of materials (solids and liquids) show that, in a plot of S v.s. u_p, the data points lie along a straight

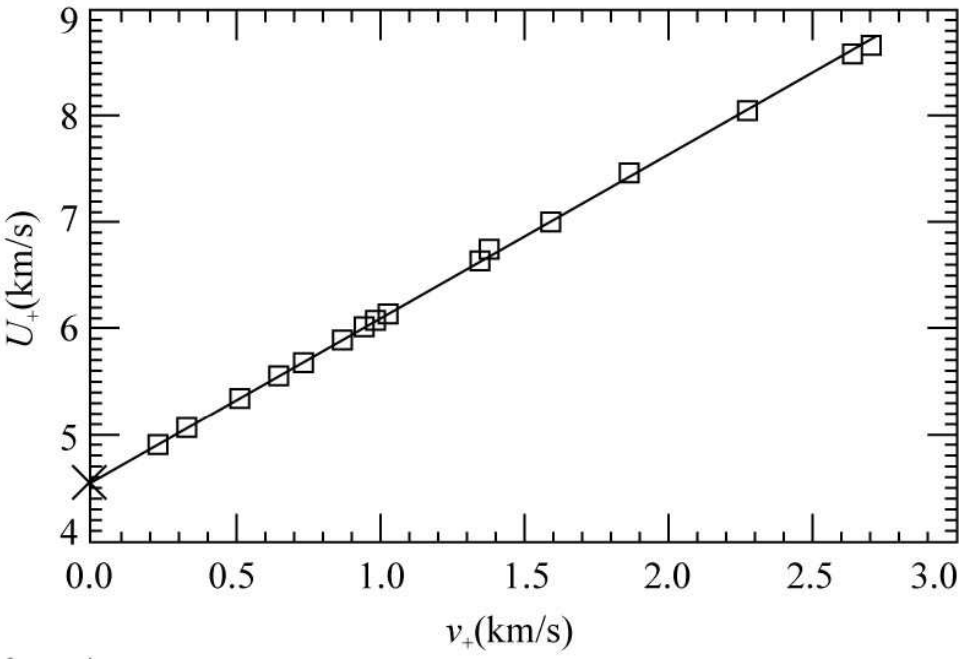

Figure B-1: The (U_S, u_p)-diagram for AISI-304 stainless steel. The squares denote individual experimental measurements.

line. Figure B-1 shows a representative example of a sequence of these measurements for AISI-304 stainless steel. The data can be approximated with great accuracy by a relationship of the form

$$S = c_0 + s\, u_p\,, \tag{B.2}$$

where c_0 and s are fitting parameters. The target block in these experiments has properties characterized by $p = 0$, $u = 0$, and $\rho = \rho_0$, all known quantities. From these expressions, and the mass and momentum Eulerian jump conditions in equation (2.9), one can derive the following expression for the pressure

$$p(\eta) = \frac{\rho_0\, c_0^2\, \eta}{(1 - s\,\eta)^2}\,, \tag{B.3}$$

where η is defined by

$$\eta = 1 - \frac{\rho_0}{\rho_1} = 1 - \frac{\mathrm{v}_1}{\mathrm{v}_0}\,. \tag{B.4}$$

Phase	ρ_0 (Mg/m^3)	c_0 (km/s)	s	p_{crit} (GPa)
α-iron	7.874	4.63	1.33	13.0
ϵ-iron	8.721	3.20	2.30	9.8

Table B.1: Material constants for α and ϵ iron.

This empirical fit is known as the Mie-Grüneisen equation of state. We note that this functional form of the equation of state can also be derived heuristically from a classical standpoint (see [39]).

The expression η is called the deformation and represents the amount of compression felt by the sample, it is 0 under no deformation, negative when the deformation is expansive, and positive when the deformation is compressive.

In most of this thesis, with an appropriate choice of coefficients (see table B.1), we used (B.3) as the equation of state. The material constants in the table follow from the available experimental data for α-iron and ϵ-iron (see [14]).

Remark 7 *We should state that for α–iron the fitting constants c_0 and s are well documented and the values shown above were taken from [4]. The data for ϵ–iron is more uncertain. Several different sets of parameters have been used in the literature [53, 12]. In addition to the ϵ–iron phase most data also represent the γ–iron phase. To avoid error in using data that might misrepresent the ϵ–iron equation of state, only data that corresponded to ϵ–iron was used. Specifically the (u_p, S) data was taken from [52], where a linear fit gave the numbers given in table B.1.*

Remark 8 *A great deal of uncertainty exists as to the values of p_{crit}, see [36, 51, 6]. The values for the forward transformation at room temperature range from $9 \ldots 15\, GPa$ while those of the backwards transformation range from $7 \ldots 10\, GPa$. The value of the forward transformation is most closely similar to the one reported on in [2]. The value of the backwards transformation corresponds to the same value used by Bruno and Vaynblat [14].*

Figure 3-7 on page 57 shows an example of a typical (v, p)-plot for a Mie-Grüneisen equation of state. There one sees the two branches, with the upper branch corresponding to martensite and the lower branch to austenite.

Appendix C

Conservation of Momentum Discretization

In this appendix we present the semi–discrete equations for the conservation of momentum, used in the numerical solution of the model for shock induced phase transitions, as modified by the addition of dissipation — see subsection 4.2.1. We use the following cell centered approximations for the first order space derivatives that appear in equation (4.5), which follow from using centered differences:

$$\frac{\partial}{\partial\xi}\bar{u}(\xi_{i+\frac{1}{2}}) \approx \frac{\bar{u}(\xi_{i+\frac{3}{2}},t) - \bar{u}(\xi_{i-\frac{1}{2}},t)}{2\,\Delta\xi} \qquad \text{and} \qquad \frac{\partial}{\partial\xi}p(\xi_{i+\frac{1}{2}},t) \approx \frac{p(\xi_{i+1},t) - p(\xi_i,t)}{\Delta\xi}\,. \tag{C.1}$$

Similarly, for the viscous term we use the spatial discretization:

$$\overline{\frac{\partial}{\partial\xi}\left(\frac{1}{\mathrm{v}}\frac{\partial u}{\partial\xi}\right)} \approx \frac{1}{\Delta\xi^2}\left[\frac{\bar{u}(\xi_{i+\frac{3}{2}},t) - \bar{u}(\xi_{i+\frac{1}{2}},t)}{\mathrm{v}(\xi_{\mathrm{i}+1},\mathrm{t})} - \frac{\bar{u}(\xi_{i+\frac{1}{2}},t) - \bar{u}(\xi_{i-\frac{1}{2}},t)}{\mathrm{v}(\xi_{\mathrm{i}},\mathrm{t})}\right]. \tag{C.2}$$

In all cases the terms on the right hand sides of the expressions are defined in their natural domains (node centered densities and cell centered velocities). With these approximations, the semi-discrete equation for the conservation of momentum (correct

up to second order in $\Delta\xi$) is then:

$$\begin{aligned}
\frac{\partial}{\partial t}\bar{u}(\xi_{i+\frac{1}{2}},t) &= \left(\frac{(1-\xi_i)\,\dot{s}_{m-1}+\xi_i\,\dot{s}_m}{s_m-s_{m-1}}\right)\frac{\bar{u}(\xi_{i+\frac{3}{2}},t)-\bar{u}(\xi_{i-\frac{1}{2}},t)}{2\Delta\xi} \\
&\quad -\left(\frac{1}{s_m-s_{m-1}}\right)\frac{p(\xi_{i+1},t)-p(\xi_i,t)}{\Delta\xi}+\frac{\mu}{(s_m-s_{m-1})^2}\frac{1}{\Delta\xi}\times \\
&\quad \left[\frac{1}{\mathrm{v}(\xi_{\mathrm{i}+\frac{1}{2}},\mathrm{t})}\left(\frac{\bar{u}(\xi_{i+\frac{3}{2}},t)-\bar{u}(\xi_{i+\frac{1}{2}},t)}{\Delta\xi}\right)\right. \\
&\quad \left.-\frac{1}{\mathrm{v}(\xi_{\mathrm{i}},\mathrm{t})}\left(\frac{\bar{u}(\xi_{i+\frac{1}{2}},t)-\bar{u}(\xi_{i-\frac{1}{2}},t)}{\Delta\xi}\right)\right]. \qquad \text{(C.3)}
\end{aligned}$$

Appendix D

Summary of the Interface Boundary Conditions used in the Viscous Code

In chapter 4 a numerical code is developed for the viscous Lagrangian conservation of mass and momentum equations (4.2), for a region containing several domains separated by moving discontinuities. In subsection 4.2.2, boundary conditions were derived for the nodes and cells around the interface between two domains. Here we summarize the semi-discrete and fully discrete equations used at each node and cell near the interface. See figure 4-3 (page 76) for the names of the cells and nodes used here. We note that in the problem the forward transformation front is right-facing while the backwards transformation front is left-facing. In this case we present a summary of the equations used for each variable around the interface.

1. If the interface is a *forward transformation front.*

   - Update $\mathrm{v_N}$ using the conservation of mass jump condition

$$\dot{s}\,(\mathrm{v_N} - \mathrm{v_1}) + \left(\frac{1}{2}(\bar{\mathrm{u}}_\mathrm{N} + \bar{\mathrm{u}}_{\mathrm{N}-1}) - \frac{1}{2}(\bar{\mathrm{u}}_0 + \bar{\mathrm{u}}_1)\right) = 0\,.$$

- Update $\bar{u}_N$ using first order extrapolation of velocity

$$\bar{u}_N - 2\bar{u}_{N-1} - \bar{u}_{N-2} = 0\,.$$

- Update s using the conservation of momentum jump condition

$$\dot{s}\left(\frac{1}{2}(\bar{u}_N + \bar{u}_{N-1}) - \frac{1}{2}(\bar{u}_0 + \bar{u}_1)\right) - (p(\mathrm{v_N}) - \mathrm{p(v_1)}) + \frac{\mu}{\Delta\xi}\left(\frac{\bar{u}_N - \bar{u}_{N-1}}{\mathrm{v_N}} - \frac{\bar{u}_1 - \bar{u}_0}{\mathrm{v_1}}\right) = 0\,.$$

- Update $\bar{u}_0$ using first order extrapolation of velocity

$$\bar{u}_0 - 2\bar{u}_1 - \bar{u}_2 = 0\,.$$

- Update $\mathrm{v_1}$ using the critical condition

$$p(\mathrm{v_1}) - \mathrm{p}^{\mathrm{A}}_{\mathrm{crit}} = 0\,.$$

2. If the interface is a *contact discontinuity*.

- Update $\mathrm{v_N}$ using the conservation of mass partial differential equation, in domain A evaluated at the local node $\xi = 1$.

$$\frac{D}{Dt}\mathrm{v_N} - \frac{1}{\mathrm{s} - \xi_{\mathrm{L}}}\frac{\bar{\mathrm{u}}_{\mathrm{N}} - \bar{\mathrm{u}}_{\mathrm{N}-1}}{\Delta\xi} = 0\,.$$

- Update $\bar{u}_N$ with the conservation of mass jump condition

$$\frac{1}{2}\left(\bar{u}_N + \bar{u}_{N-1}\right) - \frac{1}{2}\left(\bar{u}_0 + \bar{u}_1\right) = 0\,.$$

- Update s with

$$\frac{ds}{dt} = 0\,.$$

- Update $\bar{u}_0$ with the conservation of momentum jump condition

$$-\left(p(\mathrm{v_N}) - \mathrm{p}(\mathrm{v}_1)\right) + \frac{\mu}{\Delta\xi}\left(\frac{\bar{u}_N - \bar{u}_{N-1}}{\mathrm{v_N}} + \frac{\bar{u}_1 - \bar{u}_0}{\mathrm{v}_1}\right) = 0\,.$$

- Update v_1 using the conservation of mass partial differential equation in domain B, evaluated at the local node $\xi = 0$

$$\frac{D}{Dt}\mathrm{v}_1 - \frac{1}{\xi_\mathrm{R} - \mathrm{s}}\frac{\bar{\mathrm{u}}_1 - \bar{\mathrm{u}}_0}{\Delta\xi} = 0\,.$$

3. If the interface is a *backwards transformation front.*

- Update $\mathrm{v_N}$ with the critical pressure condition

$$p(\mathrm{v_N}) - \mathrm{p}^{\mathrm{M}}_{\mathrm{crit}} = 0\,.$$

- Update $\bar{u}_N$ with first order extrapolation of velocity

$$\bar{u}_N - 2\bar{u}_{N-1} - \bar{u}_{N-2} = 0\,.$$

- Update s using the conservation of momentum jump conditions

$$\begin{aligned}\dot{s}\left(\frac{1}{2}(\bar{u}_N + \bar{u}_{N-1}) - \frac{1}{2}(\bar{u}_0 + \bar{u}_1)\right) \quad &- \quad \left(p(\mathrm{v_N}) - \mathrm{p}(\mathrm{v}_1)\right) \\ &+ \quad \frac{\mu}{\Delta\xi}\left(\frac{\bar{u}_N - \bar{u}_{N-1}}{\mathrm{v_N}} - \frac{\bar{u}_1 - \bar{u}_0}{\mathrm{v}_1}\right) = 0\,.\end{aligned}$$

- Update $\bar{u}_0$ using first order extrapolation of the velocity

$$\bar{u}_0 - 2\bar{u}_1 - \bar{u}_2 = 0\,.$$

- Update v_1 using conservation of mass jump condition

$$\dot{s}\,(\mathrm{v_N} - \mathrm{v}_1) + \left(\frac{1}{2}(\bar{\mathrm{u}}_\mathrm{N} + \bar{\mathrm{u}}_{\mathrm{N}-1}) - \frac{1}{2}(\bar{\mathrm{u}}_0 + \bar{\mathrm{u}}_1)\right) = 0\,.$$

With this specification of the equation used at every node to update the local value, the numerical scheme is well defined and can be implemented. Care must be taken to insure that, when the interface changes type, these changes are detected and the correct equations are used.

Bibliography

[1] Don L. Anderson. Bulk attenuation in the earth and viscosity of the core. *Nature*, 285:204–207, 1980.

[2] D. Bancroft, E. L. Peterson, and S. Minshall. Polymorphism of iron at high pressure. *J. Appl. Phys.*, 27:291–298, 1956.

[3] William Band. Studies in the theory of shock propagation in solids. *J. Geophys. Res.*, 65:695–719, 1960.

[4] L. M. Barker. α-phase hugoniot of iron. *J. Appl. Phys.*, 46:2544–2547, 1975.

[5] L. M. Barker and R. E. Hollenbach. Shock wave study of the $\alpha \rightleftarrows \epsilon$ phase transition in iron. *J. Appl. Phys.*, 45:4872–4887, 1974.

[6] J. M. Besson and M. Nicol. An equation of state of γ–Fe and some insights about magnetoelastic effects on measurements of the α–γ–ϵ triple point and other transitions. *J. Geophys. Res.*, 95:21717–21720, 1990.

[7] R. Boehler, M. Nicol, and M. L. Johnson. Internally–heated diamond–anvil cell: phase diagram and P-V-T of iron. In M. H. Manghnani and Y. Syono, editors, *High–pressure research in mineral physics*, pages 173–176. Terra Scientific Publishing, Tokyo, 1987.

[8] J. C. Boettger and D. C. Wallace. Metastability and dynamics of the shock-induced phase transition in iron. *Phys. Rev. B*, 55:2840–2849, 1997.

[9] J. P. Boris and D. L. Book. Flux corrected transport I. SHASTA, a fluid transport algorithm that works. *J. Comp. Phys.*, 11:38–69, 1973.

[10] P. W. Bridgeman. The compression of 46 substances to $50,000\,kg/cm^2$. *Proc. Am. Acad. Arts Sci.*, 74:20–51, 1940.

[11] P. W. Bridgeman. The linear compression of iron to $30,000\,kg/cm^2$. *Proc. Am. Acad. Arts Sci.*, 74:11–20, 1940.

[12] J. M. Brown and R. G. McQueen. Phase transitions, Grüneisen parameter, and elasticity for shocked iron between 77 GPa and 400 GPa. *J. Geophys. Res.*, 91:7485–7494, 1986.

[13] Oscar Bruno and Dimitri Vaynblat. Shock–induced martensitic phase transitions I: critical stresses, two–wave structures, riemann problems. 2000.

[14] Oscar Bruno and Dimitri Vaynblat. Shock–induced martensitic phase transitions II: Graphite, diamond and iron. 2000.

[15] P. Colella. Glimm's method for gas dynamics. *SIAM J. Sci. Statist. Comput.*, 3:76–110, 1982.

[16] P. Colella. A direct Eulerian MUSCL scheme for gas dynamics. *SIAM J. Sci. Stat. Comput.*, 6:104–177, 1985.

[17] P. Colella and P. R. Woodward. The piecewise parabolic method (PPM) for gas-dynamical simulations. *J. Comput. Phys.*, 54:174–201, 1984.

[18] R. Courant and K. O. Friedrichs. *Supersonic Flow and Shock Waves*. Interscience Publishers, Inc., New York, 1948.

[19] R. Courant, E. Isaacson, and M. Reeves. On the solution of nonlinear hyperbolic differential equations by finite differences. *Comm. Pure Appl. Math.*, 5:243–255, 1952.

[20] L. Davison and R. A. Graham. Shock compression of solids. *Phys. Reports*, 55:255–379, 1979.

[21] P. S. DeCarli and J. C. Jamieson. Formation of diamond by explosive shock. *Science*, 133:1821–1822, 1961.

[22] D. S. Drumheller. *Introduction to Wave Propagation in Nonlinear Fluids and Solids*. Cambridge University Press, Cambridge, U.K., 1998.

[23] J. K. Dukowicz. A general, non-iterative Riemann solver for Godunov's method. *J. Comput. Phys.*, 61:119–137, 1985.

[24] G. E. Duvall and R. A. Graham. Phase transitions under shock-wave loading. *Rev. Mod. Phys.*, 49:523–579, 1977.

[25] B. Engquist and S. Osher. Stable and entropy satisfying approximations for transonic flow calculations. *Mathematics of Computation*, 34:45–75, 1980.

[26] D. J. Erskine and W. J. Nellis. Shock–induced martensitic transformation of highly oriented graphite to diamond. *J. Appl. Phys.*, 71:4882–4886, 1992.

[27] Wildon Fickett and William C. Davis. *Detonation*. University of California Press, Berkeley, 1979.

[28] S. K. Godunov. A difference scheme for the numerical computation of a discontinuous solution of the hydrodynamic equations. *Math. Sbornik*, 47:271–306, 1959.

[29] A. Harten. High resolution schemes for hyperbolic conservation laws. *J. Comp. Phys.*, 49:357–393, 1983.

[30] A. Harten. On a class of high resolution total-variation-stable finite-difference schemes. *SIAM J. Numer. Anal.*, 21:1–23, 1984.

[31] A. Harten, B. Engquist, S. Osher, and S. Chakravarthy. Uniformly high order accurate essentially non-oscillatory schemes,III. *J. Comput. Phys.*, 71:231–303, 1987.

[32] A. Harten and J. M. Hyman. Self-adjusting grid methods for one-dimensional hyperbolic conservation laws. *J. Comp.Phys.*, 50:235–269, 1983.

[33] A. Harten and S. Osher. Uniformly high-order accurate nonoscillatory schemes. I. *SIAM J. Numer. Anal.*, 24:279–309, 1987.

[34] A. Harten, S. Osher, B. Engquist, and S. Chakravarthy. Some results on uniformly high order accurate essentially non-oscillatory schemes. *Appl. Numer. Math.*, 2:347–377, 1986.

[35] James M. Hill. *One–dimensional Stefan Problems: an Introduction.* John Wiley & Sons, Inc., New York, 1987.

[36] E. Huang, W. A. Basset, and P. Tao. Study of bcc-hcp iron phase transition by synchrotron radiation. In M. H. Manghnani and Y. Syono, editors, *High-pressure research in mineral physics*, pages 165–172. Terra Scientific Publishing, Tokyo, 1987.

[37] R. Jeanloz. Properties of iron at high pressure and the state of the core. *J. Geophys. Res.*, 84:6059–6069, 1979.

[38] R. Jeanloz. The nature of the earths core. *Ann. Rev. Earth Planet. Sci.*, 18:357–386, 1990.

[39] J. N. Johnson. Single–particle model of a solid: The mie-grüneisen equation. *American Journal of Physics*, 36:917–919, 1968.

[40] J. N. Johnson and L. M. Barker. Dislocation dynamics and steady plastic wave profiles in 6061-T6 aluminum. *J. Appl. Phys.*, 40:4321–4334, 1969.

[41] W. Klement Jr. and A. Jayaraman. In H. Reiss, editor, *Progress in Solid State Chemistry*, volume 3, page 289. Pergamon, New York, 1967.

[42] J. Krumhansl and H. Brooks. The lattice vibration specific heat of graphite. *J. Chem. Phys.*, 21:1663, 1953.

[43] E. Kuramoto, Y. Aono, and K. Kitajima. Thermally activated slip deformation of high purity iron single crystals between 4.2 k and 300 k. *Scripta Metall.*, 13:1039–1042, 1979.

[44] P. D. Lax. Weak solutions of nonlinear hyperbolic equations and their numerical computation. *Comm. Pure Appl. Math.*, 7:159–193, 1954.

[45] P. D. Lax. Hyperbolic systems of conservation laws II. *Comm. Pure Appl. Math.*, 10:537–566, 1957.

[46] P. D. Lax and B. Wendroff. Systems of conservation laws. *Comm. Pure Appl. Math.*, 13:217–237, 1960.

[47] P. D. Lax and B. Wendroff. Difference schemes for hyperbolic equations with high order of accuracy. *Comm. Pure Appl. Math.*, 17:381–398, 1964.

[48] B. Van Leer. Flux vector splitting for the Euler equations. In *Proc. 8th International Conference on Numerical Methods in Fluid Dynamics*. SIAM–AMS, Springer Verlag, 1982.

[49] R. J. LeVeque. *Numerical Methods for Conservation Laws*. Birkhäuser Verlag, Basel, 1992.

[50] R. W. MacCormack. The effect of viscosity in hypervelocity impact cratering. *AIAA Journal*, 69:354–365, 1969.

[51] M. H. Manghnani, L. C. Ming, and N. Nakagiri. Investigation of the α-fe$rightleftarrows\epsilon$-fe phase transition by synchrotron radiation. In M. H. Manghnani and Y. Syono, editors, *High-pressure research in mineral physics*, pages 155–163. Terra Scientific Publishing, Tokyo, 1987.

[52] S. P. Marsh, editor. *LASL Shock Hugoniot Data*. University of California Press, Berkeley, 1980.

[53] R. G. McQueen, S. P. Marsh, J. W. Taylor, J. N. Fritz, and W. J. Carter. The equation of state of solids from shock wave studies. In R. Kinslow, editor, *High-Velocity Impact Phenomena*, pages 293–417. Academic Press, New York and London, 1970.

[54] R. Menikoff and B. J. Plohr. The riemann problem for fluid flow of real materials. *Rev. Mod. Phys.*, 61:75–130, 1988.

[55] J. Von Neumann and R. D. Richtmyer. A method for the numerical calculation of hydrodynamic shocks. *J. Appl. Phys.*, 21:232–237, 1950.

[56] S. Osher. Shock modeling in aeronautics. In K. W. Morton and M. J. Baines, editors, *Numerical Methods for Fluid Dynamics*, pages 179–218. Academic Press, London, 1982.

[57] S. Osher and F. Solomon. Upwind difference schemes for hyperbolic systems of conservation laws. *Math. Comput.*, 38:339–374, 1982.

[58] F. E. Prieto and C. Renero. Steady shock profiles in solids. *J. Appl. Phys.*, 44:4013–4016, 1973.

[59] R. D. Richtmyer. *Difference methods for initial–value problems.* Interscience, New York, 1967.

[60] P. L. Roe. Approximate riemann solvers, parameter vectors and difference schemes. *J. Comp. Phys.*, 43:357–372, 1981.

[61] P. L. Roe. The use of the riemann problem in finite difference schemes. In *Lecture Notes in Physics.* Springer Verlag, Berlin, 1981.

[62] C. J. M. Rooymans. In R. S. Bradley, editor, *Advances in High Pressure Research*, volume 2, page 1. Academic, New York, 1969.

[63] A. D. Sakharov, R. M. Zaidel, V. N. Mineev, and A. G. Oleinik. Experimental investigation of the stability of shock waves and the mechanical properties of substances at high pressures and temperatures. *Sov. Phys.-Dokl.*, 9:1091–1094, 1965.

[64] R. A. Secco. *Mineral physics and crystallography: a handbook of physical constants.* Wiley–interscience, New York, N.Y., 1995.

[65] J. Smoller. *Shock Waves and Reaction–Diffusion Equations.* Springer, New York, N.Y., 1983.

[66] J. L. Steger and R. F. Warming. Flux vector splitting of the inviscid gas–dynamic equations with application to finite difference methods. *J. Comp. Phys.*, 14:361–370, 1982.

[67] J. W. Swegle and D. E. Grady. Shock viscosity and the prediction of shock wave rise times. *J. Appl. Phys.*, 58:692–701, 1985.

[68] B. van Leer. Towards the ultimate conservative difference scheme II. Monotinicity and conservation combined in a second order scheme. *J. Comput. Phys.*, 14:361–370, 1974.

[69] B. van Leer. Towards the ultimate conservative difference scheme IV. A new approach to numerical convection. *J. Comput. Phys.*, 23:276–299, 1977.

[70] B. van Leer. Towards the ultimate conservative difference scheme V. A second order sequel to godunov's method. *J. Comput. Phys.*, 32:101–136, 1979.

[71] D. Vaynblat. *The Strongly Attracting Character of Large Amplitude Nonlinear Resonant Acoustic Waves Without Shocks. A Numerical Study.* PhD dissertation, MIT, Department of Mathematics, Aug 1996.

[72] E. Vlodarchik and R. Trebinski. Transformation of graphite and boron nitride in shock waves. *Shock Waves*, 7:231–248, 1997.

[73] J. M. Walsh. *Bull. Am. Phys. Soc.*, 29:28, 1954.

[74] J. P. Walsh and R. H. Christian. Equation of state of metals from shock wave measurements. *Phys. Rev.*, 97:1544–1556, 1955.

[75] G. B. Whitham. *Linear and Nonlinear Waves.* Wiley–interscience, New York, N.Y., 1973.

[76] Y. B. Zel'dovich and Y. P. Raizer. *Physics of Shock Waves and High-Temperature Hydrodynamic Phenomena*, volume 2. Academic Press, New York, 1967.